REPORT DOCUMENTATION PAGE

1. AGENCY USE ONLY *(Leave blank)*	2. REPORT DATE 30.Oct.00	3. REPORT TYPE AND DATES COVERED THESIS

4. TITLE AND SUBTITLE
MECHANICAL AND MICROSTRUCTURAL EFFECTS IN FRETTING FATIGUE OF TI-61-4V

5. FUNDING NUMBERS

6. AUTHOR(S)
2D LT CONNER BRETT P

7. PERFORMING ORGANIZATION NAME(S) AND ADDRESS(ES)
MASSACHUSETTS INSTITUTE OF TECHNOLOGY

8. PERFORMING ORGANIZATION REPORT NUMBER
CY00391

9. SPONSORING/MONITORING AGENCY NAME(S) AND ADDRESS(ES)
THE DEPARTMENT OF THE AIR FORCE
AFIT/CIA, BLDG 125
2950 P STREET
WPAFB OH 45433

10. SPONSORING/MONITORING AGENCY REPORT NUMBER

11. SUPPLEMENTARY NOTES

12a. DISTRIBUTION AVAILABILITY STATEMENT
Unlimited distribution
In Accordance With AFI 35-205/AFIT Sup 1

12b. DISTRIBUTION CODE

13. ABSTRACT *(Maximum 200 words)*

20001116 012

DTIC QUALITY INSPECTED 4

14. SUBJECT TERMS

15. NUMBER OF PAGES
111

16. PRICE CODE

17. SECURITY CLASSIFICATION OF REPORT	18. SECURITY CLASSIFICATION OF THIS PAGE	19. SECURITY CLASSIFICATION OF ABSTRACT	20. LIMITATION OF ABSTRACT

Mechanical and Microstructural Effects on Fretting Fatigue of Ti–6Al–4V

by

Brett P. Conner

B.S., Physics, University of Missouri-Columbia (1998)

Submitted to the Department of Materials Science and Engineering
in partial fulfillment of the requirements for the degree of

Master of Science

at the

MASSACHUSETTS INSTITUTE OF TECHNOLOGY

June 2000

Signature of Author . . . .
Department of Materials Science and Engineering
17 May 2000

Certified by . . . .
Subra Suresh
R. P. Simmons Professor of Materials Science and Engineering
Thesis Supervisor

Certified by . . . .
Antonios E. Giannakopoulos
Research Scientist
Thesis Supervisor

Accepted by . . . .
Carl V. Thompson
Stavros Salapatas Professor of Materials Science and Engineering
Chair, Departmental Committee on Graduate Students

Mechanical and Microstructural Effects on Fretting Fatigue of Ti–6Al–4V

by

Brett P. Conner

Submitted to the Department of Materials Science and Engineering
on 17 May 2000, in partial fulfillment of the
requirements for the degree of
Master of Science

Abstract

Fretting fatigue is the repetitive sliding of contacting surfaces at small displacements and can cause cracking that leads to failure in the presence of a bulk fatigue load. Dovetail joints in gas turbine engines are particularly susceptible to fretting fatigue and are the motivation for this study. Experiments are conducted in ambient air utilizing a sphere-on-flat contact geometry since its contact mechanics are well known. The effect of changing critical contact and bulk loading parameters are examined in depth for a mill annealed and solution treated overaged variants of Ti–6Al–4V. Parameters which are instrumented and controlled include the applied normal load, tangential load, and axial fatigue load. The fretting fatigue resistance of several other heat treated variants of Ti–6Al–4V are compared versus the two more common variants. Various stages of fretting fatigue crack growth are examined using a fracture mechanics approach. A multiaxial stress-based crack initiation criteria is developed and evaluated. The adhesion model of Giannakopoulos et al., is invoked to determine a contact fatigue threshold of 2 MPa$\sqrt{\text{m}}$ for Ti–6Al–4V and forms the basis of a life-prediction methodology. Finally, the usefulness of various surface treatments and dovetail designs as palliatives to counter fretting fatigue is discussed.

Thesis Supervisor: Subra Suresh
Title: R. P. Simmons Professor of Materials Science and Engineering

Thesis Supervisor: Antonios E. Giannakopoulos
Title: Research Scientist

Contents

List of Figures

6

7

List of Tables

Chapter 1

Introduction

Any engineering structure that requires contact and has repeated relative motion between the contacting surfaces is prone to a reduction in performance because of cracking. This is called contact fatigue and includes rolling, sliding, spin or torsion contact, and fretting. Small cracks initiate because of wear through mechanisms such as galling, spalling, surface distress and pitting. The geometry of contact can vary considerably, and the contact surfaces may or may not conform to each other. To understand the complex nature of contact fatigue, one must consider contact mechanics, tribology, fatigue, and fracture mechanics.

Fretting is a type of contact fatigue described as a repetitive sliding or slipping between two contacting surfaces such that the cyclic amplitude of the displacement is between 5-50 μm [1]. Fretting is a type of partial-slip because the slip is confined to regions near the edge of contact while the central portion of contact involves adherence between the two surfaces. This is in contrast to global sliding where the entire contact surface is subject to relative motion. Fretting has a deleterious effect on the fatigue life of contacting materials. Fretting fatigue occurs if cyclical bulk loads are superimposed on one or both of the contacting bodies. The contact mechanics of fretting fatigue consist of a very complex mixture of the effects of tangential load, normal load, bulk stresses, coefficient of kinetic friction and contact area. The combination of these factors affects the relative displacement and the contact stresses.

Fretting fatigue adversely affects a variety of engineering systems. These include riveted and bolted joints, metal ropes and cables, coil wedges in generator rotors, shrink-fitted couplings and the blade-dovetail regions of gas turbine engines [2]. Fretting fatigue is also one of the

primary sources of failure in biomechanical implants [3]. Nonmetals are also susceptible to the effects of fretting fatigue, and fretting experiments have been conducted on nonmetallic materials [4].

The effects of fretting fatigue was first noted in 1911 when Eden et al. [5] observed the formation of oxides in the grips of a tensile fatigue specimen. Then, Tomlinson [6] determined that the oxides must develop from tangential contact between contacting surfaces. In 1941, Warlow-Davies [7] determined that fretting fatigue reduced the fatigue strength. In 1960, the bridge-pad fretting fatigue apparatus was developed, and this became a very popular experimental method. The use of cylindrical pads for fretting experiments was brought forward by Milestone [8]. This geometry provided analytically determined stress fields beneath the contact.

From 1969-1972, Nishioka and Hirakawa addressed several critical fretting fatigue issues. First, it was demonstrated that slip amplitude affected the fretting damage such that below a specific slip amplitude (generally 5 μm), minimal damage occurred [9]. However, slip amplitudes above 50 μm resulted in significant wear which lead to the removal of cracks initiated by fretting fatigue. Second, cracks were observed to initiate at the edge of contact and propagated at an angle to the surface of the specimen [10]. Third, the coefficient of friction changed as a function of the number of cycles for a given frequency and load (this phenomenon will be described in Section 3.1) [10]. Fourth, Nishokia and Hirakawa suggested that contact stresses influence crack initiation while bulk stresses affect propagation [11]. Fifth, the slip amplitude was shown to be related to the tangential loading, and an increase the rate of crack initiation was more dependent on an increase of the tangential load than of the slip amplitude [12].

Other variables of concern were addressed including adhesion, temperature effects and pad radii. The issue of adhesion was first approached by Godfrey [13] and then experimentally addressed by Bethune and Waterhouse [14]. The possibility of fretting induced temperature changes was considered by Waterhouse [15] and then later by Attia [16, 17]. The effects of contact length/radius was first examined by Bramhall [18] and further work has been accomplished by Araújo and Nowell [19].

Endo [20] and Edwards [21] first applied fracture mechanics into the problem of fretting fatigue. Fracture mechanics is advantageous for life-prediction methodology, thresholds and

the issue of arrested cracks versus propagating cracks. Nowell also put forward a fracture mechanics approach in his doctoral thesis [22]. Fracture mechanics has been applied through the determination of an arbitary initial flaw size [23] or a distributed dislocation model [24]. Giannakopoulos et al. [25] developed a bridge between aspects of contact mechanics in fretting fatigue and fracture mechanics by the so-called crack analogue. This methodology connected the physical contact parameters for a sharp edged punch and with the stress fields for a cracked edge specimen. The resultant stress-intensity factors lead to fracture mechanics that could be invoked as a crack initiation criteria and a life prediction methodology. A notch analogue was recently developed for flat punches with rounded corners,and provided a connection between stress concentration and stress intensity factors in fretting [26]. Spherical and cylindrical contacts were connected to fracture mechanics through the stress field singularities produced by interfacial adhesion [27].

Several recent developments have occured. In 1998, Giannakopoulos and Suresh [28] developed a 3-D finite element model (FEM) of the stress fields produced by a sphere-on-flat contact geometry. The FEM utilized a ring-element method that substantially reduced the amount of computational cost required to conduct the modeling. Kirkpatrick [29] addressed the effect of peening on fretting fatigue in a simple model that considered the depth of peening necessary to have a compressive principal stress field without relief of residual stresses by the contact.

One of the most critical fretting fatigue issues currently is blade dovetail contact in gas turbine engines. Fretting fatigue is costly to the U. S. Air Force both in financial terms and in terms of readiness [30]. The following section describes this particular fretting fatigue issue.

1.1 Fretting fatigue in the blade dovetail region

Fretting fatigue in dovetail joints in gas turbine engines is the costliest and the insiduous problem related to high cycle fatigue of gas turbine engines in operational military use [31]. Since it is difficult to detect fretting cracks in a gas turbine engine, components must be replaced at regular intervals even if they are otherwise sound. It is very costly to replace blades and disks. In the case of a catastrophic failure due to fretting fatigue, cracking in the rotor joint or the blade itself will lead to blade separation and the resultant destruction of the engine. At

least two crashes of single-engine F-16 fighters in fiscal year 1999 were due to blade separation [32, 33]. The problem of fretting fatigue in gas turbine engines will dictate the material of focus in this study. Ti−6Al−4V is a common material for producing compressor blades in gas turbine engines and is the material examined in this investigation.
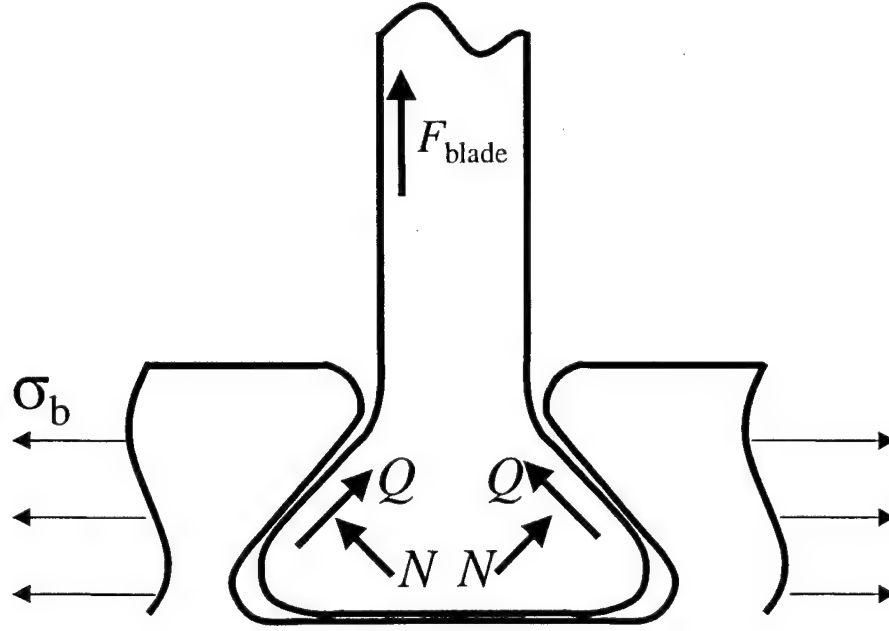
Figure 1-1: A schematic of fretting fatigue at a dovetail joint where F_{blade} is the centrifigual force on the blade, N is the resultant normal force of the blade on the disk, Q is the tangential force and σ_b is the bulk stress in the disk.

The contact geometry of the dovetail joint is shown in figure 1-1. Two loading conditions produce fretting fatigue damage at the blade/rotor interface. First, the severe changes in disk speed due to engine start up and shut down cause the opening and closing of the dovetail joints. The blades slip outward or inward due to the rotational acceleration. This contact fatigue can be considered low cycle fatigue (LCF). Second, the high frequency vibration of the blade due to blade flutter can cause fretting action at the dovetail contact [34]. Blade vibration is an HCF issue. The interaction between LCF loading and HCF loading on fretting fatigue of dovetail joints has been examined by Szolwinski et al [35]. Fretting fatigue cracks which form in the blade almost always propagate to failure because of the magnitude of the centrifugal force. Cracks that initiate in the disc often arrest as short cracks because of the lack of sufficient bulk

loading [19]. Fractography of a fractured disk lug from an aircraft turbine engine seems to indicate that the early stages of fretting fatigue cracking in the disk is due to the LCF portion of loading [36].

Fretting fatigue in a gas turbine engine takes place in a harsh environment. It is well known that air is an aggressive environment for HCF in Ti−6Al−4V [37]. Fretting fatigue that occurs in later fan stages (such as the third stage) will experience elevated temperatures (278 °C) due to the proximity to the hot portions of the engine [34].

The fretting fatigue geometry represented by the blade dovetail is a difficult geometry. The stresses beneath the contact have been determined analytically [38, 39] but are not as simple as those underneath a cylinder or flat geometry. It is advantageous to consider a simple experimental geometry that could provide fundamental insight into the fretting fatigue phenomena. A sphere-on-flat contact geometry was chosen for its well characterized contact geometry and analytically calculable stress fields.

1.2   Mechanics of Hertzian contact

The fretting fatigue contact in a dovetail joint is a complex geometry. To examine the fundamental effects of the various contact and bulk loading parameters of fretting fatigue, a sphere-on-flat geometry was chosen. This contact geometry is well understood and a schematic of the contact surface is shown in figure 1-2. The contact region is circular with a radius determined from the following relationship derived by Hertz [40]

$$a_{\text{contact}} = \sqrt[3]{K'N\rho} \qquad (1.1)$$

where N is the applied normal load and ρ is the pad radius. K' incorporates elastic material properties. If the pad and substrate are of the same material, K' is:

$$K' = \frac{3(1 - \nu^2)}{2E} \qquad (1.2)$$

where E is the elastic modulus and ν is the Poisson's ratio. From the knowledge of the radius of contact, a_{contact}, and the applied normal force, N, the maximum contact pressure, p_{max}, is

17

given by

$$p_{\max} = \frac{3N}{2\pi a_{\mathrm{contact}}^2}$$

(1.3)
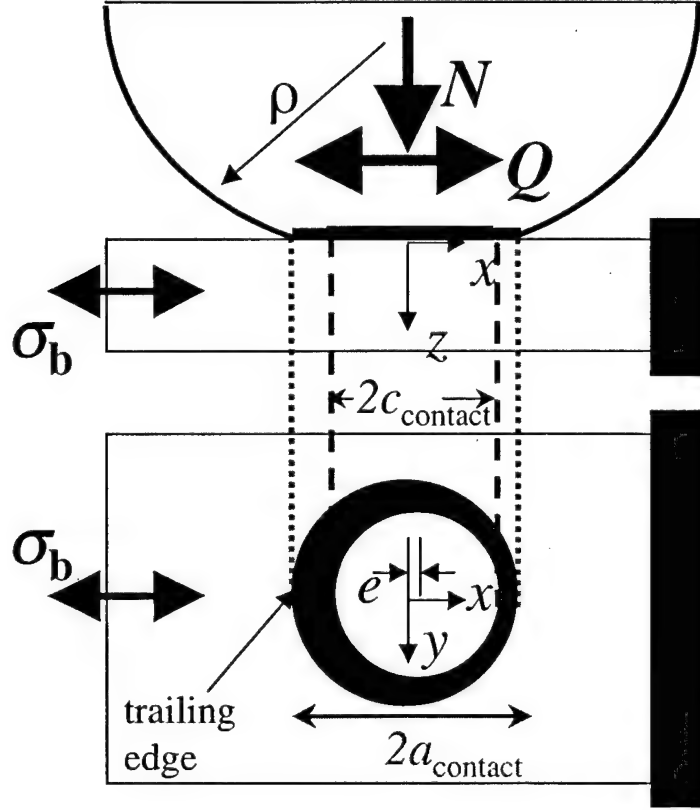
Figure 1-2: The contact geometry for sphere-on-flat fretting fatigue for a substrate fixed at one end and attached to an actuator at the opposite end.

Subsequently, to the normal load, one can apply a tangential load, Q, to the contact. This can be done either by applying a load on the sphere or on the substrate or both. In the experiments conducted in this study, the tangential load was produced by applying a load on the substrate. This is discussed in more detail in the next section. Partial slip occurs if the ratio of the maximum tangential load and the normal load ($Q_{\max}/N$) is less than the coefficient of friction, μ. Full slip occurs when $Q_{\max}/N$ exceeds the coefficient of friction. The resulting surface tractions induced by the tangential load results in an annulus of slip surrounding an adhered region [41]. The radius of the adhering region is given as [42]

$$c_{\text{contact}} = a_{\text{contact}} \left(1 - \frac{Q_{\max}}{\mu N}\right)^{\frac{1}{3}}. \tag{1.4}$$

The width of the slip annulus is determined by $(a_{\text{contact}} - c_{\text{contact}})$.

If one end of the contact substrate is fixed and the opposite has a uniaxial sinusoidal force applied to it in the x-direction causing the tangential load, the location of the stick region will shift toward the fixed end of the specimen by an amount e. This value is the eccentricity shown in figure 1-2. Hills and Nowell determined this value for a 2-D cylindrical contact [43]. The relationship for eccentricity, e, of a sphere-on-flat geometry was determined by Wittkowsky et al. [44]:

$$e = \frac{(1-\nu)}{(4-3\nu)} \frac{4\sigma_{\text{b}} a_{\text{contact}}}{\pi \mu p_{\max}} \tag{1.5}$$

where σ_{b} is the applied far-field uniaxial bulk stresses in the substrate. The fretting fatigue specimens utilized in the experimental portion of this investigation were fixed at one end and the opposite end was attached to an actuator. Thus, there was an eccentricity of the stick zone. The application of a sinuoidial uniaxial bulk stress also impacts the location of the highest maximum loading. If a tangential load is applied in the positive x-direction because of an applied tangential loading, the maximum contact stresses will be at $x = -a_{\text{contact}}$ (this will be discussed in section 4.2), which is the side closest to the actuator as shown in figure 1-2. If the direction of tangential loading is reversed because the applied bulk load has become compressive, the location of maximum contact stresses will be at $x = +a_{\text{contact}}$, but the bulk loading will be compressive. Therefore, fretting fatigue cracks will only propagate at the perimeter of contact closest to the actuator, which is $x = -a_{\text{contact}}$. For our purposes, the perimeter of contact closest to the actuator will be called the *trailing edge of contact* although strictly speaking both $x = -a_{\text{contact}}$ and $x = +a_{\text{contact}}$ can be trailing edges.

1.3 Regions of fretting fatigue crack growth

Fretting fatigue cracks can result from the Hertzian contact. Fretting fatigue crack growth can be divided into four stages (see figure 1-3), and this has been qualitatively shown in the

19
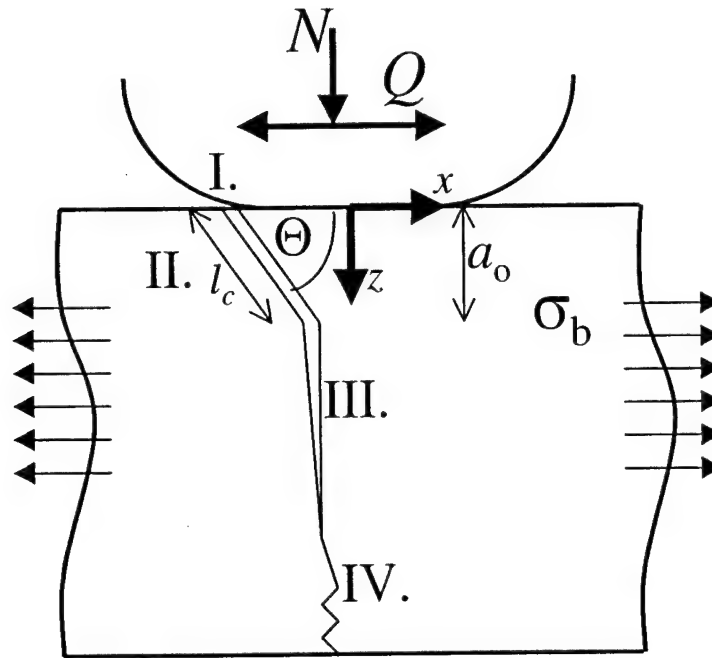
Figure 1-3: The stages of fretting fatigue crack growth. Region I is initiation. Region II is a slant crack propagating primarily due to contact loading. Region III is crack growth due to the bulk loading. Region IV is catatrophic failure.

literature as well as in this work for Ti−6Al−4V [45, 25]. Region I refers to crack initiation. The number of cycles utilized in this stage varies depending on microstructural effects, loading, and contact conditions. An examination of a fretted disk lug from a gas turbine engine revealed that cracks may have initiated and then were removed by surface wear during engine start-up and shut down [36]. After initiation, the crack will enter the material at a definitive angle and will progress into the material as long as the combination of contact stresses and bulk stresses are sufficient to propagate it. The stable crack propagation influenced primarily by contact loads can be called region II. It is important to note that during this stage the crack may be considered as a short-crack and could be treated as such in a life-prediction model. Stresses due to contact reduce as depth increases and eventually the crack turns to propagate in a direction normal to the bulk stress. Stable crack propagation due to bulk stress is region III. This region is described in more detail below. Upon turning perpendicular to the bulk stress, the crack assumes a thumbnail shape and propagates by mode I fracture until failure. Catastophic

failure is region IV. Failure will occur either when the critical stress intensity factor, ΔK_{IC}, is reached or the crack reaches the edge of the specimen and rupture occurs. Very few cycles are expended in region IV.

1.4   Overview

It was necessary to develop a body of fretting fatigue experimental results from the systematic changes of critical variables (such as the tangential load, normal load, bulk stress and pad radii) in fretting fatigue. Those experiments were to give insight into the mechanical and microstructural effects on fretting fatigue of Ti–6Al–4V. From these results, it is clear that fretting fatigue crack initiation is controlled by the contact conditions and the bulk stress has little effect. It is also made clear that stress-based modeling does not satisfactorily describe the fretting fatigue crack initiation process. On the other hand, a fracture based model, the adhesion model, agrees well with most experimental observations and leads us to crack initiation thresholds.

Chapter 2 will discuss the microstructures of Ti–6Al–4V that are examined in this study and will also give an overview of the fretting fatigue testing machine and methodology. Chapter 3 presents the experimental results of adjusting various parameters as well as frictional results and crack initiaton location. Chapter 4 covers the analysis of the experimental results. It includes a multiaxial stress-based fatigue crack initiation model as well as the adhesion model. A statement of the conclusions and future work is found in Chapter 5.

Chapter 2

Experimental materials and methods

This chapter is intended to provide background into the material examined and outline the experimental parameters of this investigation. The first section will review the metallurgy of Ti−6Al−4V and the implication of its structure on fracture and fatigue. Such a discussion is appropriate since the stages of fretting fatigue crack growth could be influenced by the microstructure. The second section will address the instrumentation and control of fretting fatigue apparatus, the contact pads and specimen geometry and the testing environment.

2.1   Materials

2.1.1   The microstructures of Ti−6Al−4V

This section is an overview of the effect of the microstructure Ti−6Al−4V and their effects on strength, fatigue and fracture properties [46]. Figure 2-1 is the phase diagram of Ti−6Al−nV [47]. The material has two phases: an hexagonal close packed alpha phase and a body-centered cubic beta phase. At four percent vanadium, the beta phase does not appear until the temperature exceeds nearly 1000°C. An alpha-beta field exists for temperatures below. As a result of heating and cooling into and out of the different phase fields, microstructures will develop that contain a range of combinations of these phases. Ti−6Al−4V has two basic microstructures: equiaxed and lamellar. A bimodal microstructure is a combination of the two.

An initial quench from the beta phase region results in a martensitic or fine lamellar struc-
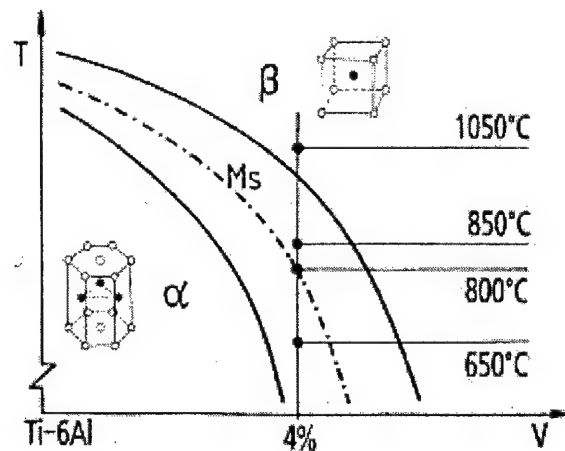
Figure 2-1: The phase diagram for the system consisting of 6% wt. Al and n% wt. V and the balance is Ti [47].

ture. Cold work rolling is often performed by a 60% reduction of the panel thickness that leads to the formation of a deformed lamellar microstructure. Various heat treatments can then be applied subsequently.

· Recrystallization at 800°C results in equiaxed primary alpha phase with 15% retained beta phase at the grain boundaries and triple points. If the recrystallization temperature is 965°C, the amount of equiaxed primary alpha is reduced to 40% with a beta matrix. The beta matrix transforms to martensite or a fine lamellar structure during rapid cooling. This is the bimodal structure. The lamellar matrix results from cooling rates of at least 37°C/min. The volume percentage of primary alpha increases to 60% with slower cooler rates. At very slow cooling rates such as 1°C/min , the amount of beta phase decreases to 15-20% and is retained.

A fine lamellar microstructure is obtained with a beta quench while a coarse lamellar microstructure can be developed by long annealing of a fine lamellar microstructure. This annealing must occur at temperatures high in the alpha+beta field. A more common approach to producing a coarse lamellar structure is to slowly cool (1°C/min) from the beta field. The coarse lamellar structure is unable to be refined by alpha-beta warm working or recrystallization.

2.1.2 Textures

Unidirectional rolling at temperatures less than or equal to 900°C results in a mixed basal/transverse texture (B/T). The basal (B) planes are parallel to the rolling plane but separated by an angle which decreases as the degree of deformation (or sharpness) of the texture increases. Transverse (T) planes are all aligned in the direction of rolling. B/T texture becomes sharper as the rolling temperature increases. Cross-rolling at 900°C or below produces the pure basal texture while deformation at high temperatures within the alpha+beta field (>900°C) will result in pure T.

Transverse poles have an important impact on the fatigue life characteristics in relationship to mean stress. Ti−6Al−4V blades produced by closed die forging have poles in the transverse direction.

2.1.3 Microstructure and the high cycle fatigue (HCF) strength

The HCF strength, σ_f, of Ti−6Al−4V varies from microstructure to microstructure. The bimodal microstructure has the highest fatigue strength followed by the equiaxed structure, and the lamellar structure has the lowest fatigue strength. Finer microstructures have higher fatigue strengths than coarser ones. The bimodal microstructure tends to have larger primary alpha grains than the fine equiaxed microstructure. However, the alpha grains in the bimodal microstructure are separated by the beta matrix. There is no separation between many of the equiaxed alpha grains and this reduces the fatigue strength. The HCF strength is summarized by the following relation where BM=bimodal, FE=fine equiaxed, CE=coarse equiaxed, FL=fine lamellar and CL=coarse lamellar:

$$\sigma_{f,BM} > \sigma_{f,FE} > \sigma_{f,CE} > \sigma_{f,FL} > \sigma_{f,CL}$$

This relationship is also true for the yield strength of the materal. Thus, uniaxial monotonic strength and HCF strength are related.

The amount of O_2 is believed to affect the fatigue properties, although there is some dispute on this issue. Jaffe and Lütjering [37] and Beevers and Robinson [48] present results that indicate that higher levels of O_2 lead to increased yield and HCF strengths. However, Yoder,

et. al. [49], dispute this claim as well as the relationship between yield strength and HCF strength.

Jaffe and Lütjering also demonstrated that texture has an effect on the fatigue strength of the material. Using fine equiaxed solution treated and aged Ti−6Al−4V, they determined that a B/T texture in the rolling direction (RD) has the highest fatigue strength while a pure basal (B) texture, which by definition has no directionality with respect to the rolling direction, has the lowest fatigue strength. The relationship between fatigue strength and texture is summarized by the following relationship where B/T-RD is the B/T texture in the rolling direction, B/T-TD is the B/T texture in the transverse direction, T-RD is the transverse texture in the rolling direction, T-TD is the transverse texture in the transverse direction and B is the pure basal texture.

$$\sigma_{f,B/T\text{-RD}} > \sigma_{f,B/T\text{-TD}} > \sigma_{f,T\text{-RD}} > \sigma_{f,T\text{-TD}} > \sigma_{f,B}$$

Texture has an effect on fatigue strength depending on the mean strength. If one plots fatigue strengths for various load ratios comparing maximum stress versus mean stress reveals a plateau from a mean stress of 0 to 200 MPa for the B/T-RD texture. This texture allows easy basal slip since the basal planes are at an angle to the RD direction. If the basal planes are parallel to the load direction, the HCF strength is normal because basal slip is not activated.

In plain fatigue, mean stress also affects the location of crack nucleation. At a load ratio of $R = \max \sigma_b / \min \sigma_b = 0.2$, the nucleation is subsurface, but nucleation is at the surface for a load ratio of $R = -1$.

2.1.4 Microstructure and fatigue crack propagation (FCP) resistance

HCF strength is governed by the material's ability to resist crack initiation. Once a crack is initiated, different microstructural characteristics effect the growth of a fatigue crack. The microstructures which best resist fatigue crack propagation (FCP) resistance are the ones with the lowest fatigue strength. Coarse lamellar microstructures offer the best FCP resistance (FCPR) while bimodal and fine equiaxed provide the least. This is summarized by the following relationship

$$\text{FCPR}_{\text{CL}} > \text{FCPR}_{\text{FL}} > \text{FCPR}_{\text{CE}} > \text{FCPR}_{\text{BM}} > \text{FCPR}_{\text{FE}}$$

As the microstructures become more coarse, crack closure effects increase and the crack front becomes more irregular.

The FCP resistance of a fully lamellar structure may decrease for semi-elliptical surface cracks at higher frequencies. Campbell and Ritchie [50] raised this issue after completing fatigue tests of solution treated overaged (bimodal) and fully lamellar Ti–6Al–4V at a frequency of 1.5 kHz. The frequencies and crack geometry involved in their experiments are very similar to those encountered in gas turbine engines. However, the lamellar colony size in their study may have been large enough to be a significant factor in crack propagation.

The effect of basal slip defines how texture affects FCP just as it did for HCF strength. For the B/T texture, stressing in the RD direction produces the best FCP resistance whereas in the TD direction it produces the lowest FCP resistance. Pure B and T have intermediate resistance.

2.1.5 Short crack FCP resistance and fracture toughness

If short surface cracks are examined, a surprising result occurs: short crack FCP resistance is dependent on the yield strength. Bimodal and equiaxed microstructures have better short crack resistance than lamellar ones. Crack closure effects are reduced because the crack faces are shorter.

Coarse lamellar microstructure yields the highest fracture toughnesses. In general, bimodal and fine equiaxed (of the same texture) have very similar fracture toughness. This is due to the high volume fraction of the fine lamellar structure in the bimodal microstructure. The lamellae in the matrix of the bimodal microstructure tend to be fine.

2.1.6 Microstructural summary

Bimodal microstructures (followed by the equiaxed microstructures) tend to have the highest yield/HCF strengths. Equiaxed microstructures (followed by the bimodal microstructures)

have the best short crack FCP resistance. However, lamellar microstructures have better long crack FCP resistance and better fracture toughness.

An important question arises when choosing a microstructure to combat fretting fatigue. Which is more critical: HCF/yield strength or FCP resistance? This becomes more complex when the issue of short cracks is raised. Another issue is the resistance of the material to contact fatigue. Can tradeoffs be made in regard to hardness and wear resistance versus HCF performance? In this work, fretting fatigue tests were conducted on various microstructures and provided some answers to the above questions.

In the long-term, fretting fatigue experiments involving several different microstructures should also be conducted at high temperatures. The elevated temperature such as those at the warm stages of a gas turbine engine could have an effect on fretting fatigue and microstructures that is different than what is found at room temperature.

2.1.7 Heat treatments examined in the present experiments

There were two major variants of Ti−6Al−4V utilized for the fretting fatigue tests: mill annealed (MA) and solution treated overaged (STOA). Fretting fatigue experiments were performed on several other heat treatments to examine the role of microstructure and fretting fatigue.

Mill annealed Ti−6Al−4V

The bar stock utilized for the tests had the following composition by weight percent: 6.08% Al, 4.01% V, 0.19% Fe, 0.18% O, 0.02% C, 0.01% N, 0.0004% H, <0.001% Y and the balance Ti. This composition met the specifications AMS 4928N and MIL-T-9047G.

Samples parallel and perpendicular to the length of the bar were removed from the bar to conduct metallography. The samples were ground with 500, 1200, 2400, 4000 grit silicon carbide paper and were mechanically polished using 3 μm diamond solution, 0.3 μm alumina solution, and 0.05 μm Mastermet$^{\circledR}$ solution. The samples were then etched with a reagent consisting of 5% HF, 10% HNO_2 and 85% distilled water. The material has an equiaxed microstructure consisting of 75% primary alpha and the remainder is beta phase. Along the length of the bar,
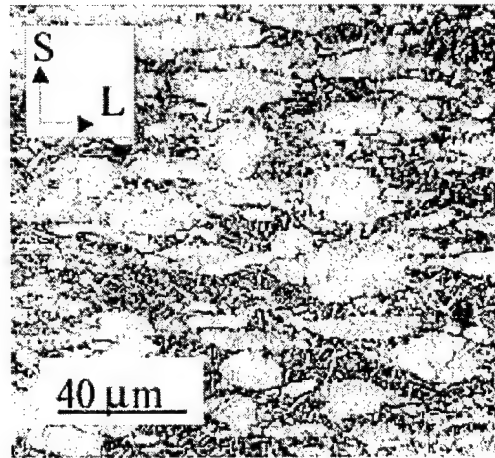
Figure 2-2: A micrograph of the mill annealed microstructure parallel to the length of the bar. This is the microstructure of the contact substrate.

Elastic modulus	116 GPa
Poisson's ratio	0.34
Tensile strength	1016 MPa
Yield strength	963 MPa

Table 2.1: Mechanical properties of the mill annealed Ti–6Al–4V.

the primary alpha grains are very elongated (50-80μm) due to cold working (in figure 2-2 this direction is denoted by L). All specimens were produced in the L-orientation. This means that the specimens were produced such that the short or transverse dimensions of the specimen were the same as those of the bar. Therefore, the contact surface of the specimen would consist of the elongated grains. The micrograph of the cross section of the bar (see figure 2-3) reveals the undisturbed equiaxed structure where the average grain size of the primary alpha grains are about 5-10 μm. This is also the grain geometry on the surface of the contacting pad. Table 2-1 lists some of the mechanical properties of mill annealed Ti−6Al−4V.

Solution treated and overaged (STOA) Ti-6Al-4V

The solution treated and overaged (STOA) Ti−6Al−4V material was developed as part of the Air Force HCF program initiative. The chemical composition of this material (in wt%) is 6.30% Al, 4.17% V, 0.19% Fe, 0.19%0, 0.13% N, and the balance Ti [51]. After forging, it was solution

28
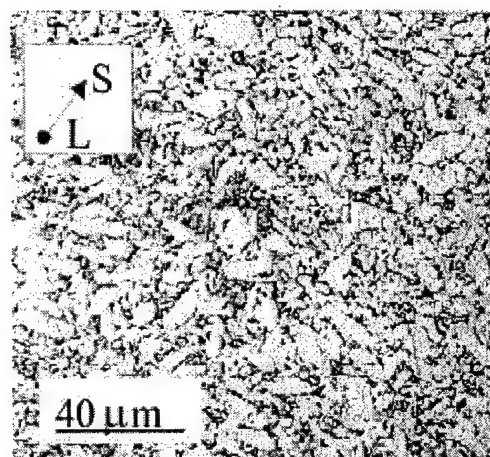
Figure 2-3: A micrograph of the mill annealed microstructure from the cross-section of the bar. This is the microstructure of the contact pad.

Elastic modulus	116 GPa
Poisson's ratio	0.34
Tensile strength	970 MPa
Yield strength	935 MPa

Table 2.2: Mechanical properties of the Air Force HCF program STOA material.

treated for 75 minutes at 932°C in an air atmosphere and air-cooled. Then, the material was vacuum annealed for 2 hours at 704°C and fan cooled in an argon atmosphere. Micrographs were produced in the same manner as the mill annealed material (see figure 2-4). The STOA microstructure is bimodal. The primary alpha grain size is 10-20 μm and is surrounded by a lamellar matrix. There is only a minor enlongation of the grains in the longitudinal direction. All specimens were produced in the L-orientation.

This material is well characterized. Table 2-2 lists the mechanical properties of the STOA material [51].

Other heat treatments

From the discussion above, it appears that the STOA material was an appropriate choice of microstructure for use in gas turbine engines in terms of *plain fatigue* performance. However, is that the best microstructure for *fretting fatigue*? To answer this question, several other
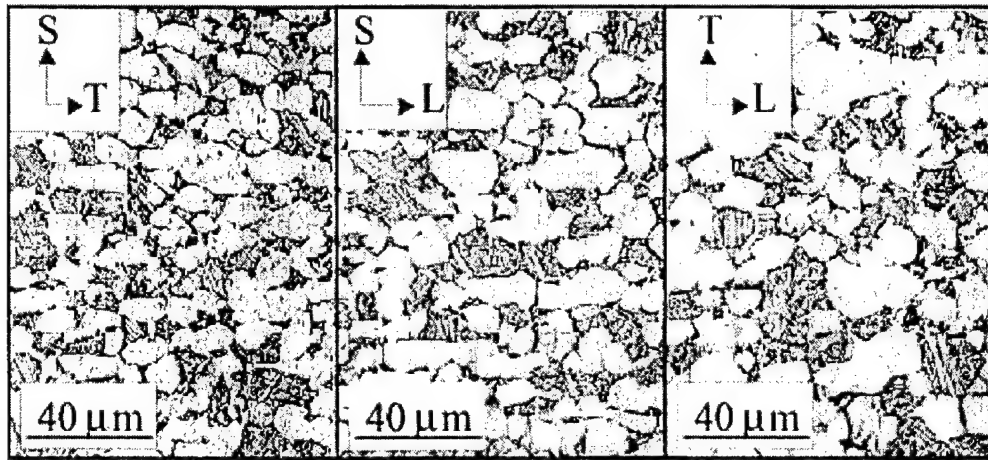
Figure 2-4: The STOA microstructure in three planes (S-T, L-S and T-L where S=short, T=transverse and L=long) is very isotropic with only a slight elongation of the grains in the L-direction.

Microstructure	Heat treatment
Martensitic	1050°C/0.5hr WQ
Coarse grained STOA	930°C/48hr AC, 700°C/12hr AC
Acicular	1050°C/0.5 AC
Beta annealed/Widmanstätten	1050°C/0.5hr FC to 700°C/1hr AC

Table 2.3: Various heat treatments used in fretting fatigue tests (WQ=water quenched, AC=air cooled and FC=furnace cooled).

microstructures were examined in this study. The specimens were vacuum encapsulated with a Ti getter and a backfill of argon gas. A list of the heat treatments is given in table 2-3. All heat treatments were produced from the Air Force HCF program STOA material. A description of their fretting fatigue performance will be given later.

The microstructures examined in this study are shown in figures 2-5, 2-6, 2-7, and 2-8. The micrographs were produced in the same manner as the mill annealed and STOA micrographs. The coarse STOA material has a grain size between 20 and 25 μm. The martensite microstructure consisted of a needle-like structure. The acicular microstructure consisted of colonies of coarse lamellar grains. The average colony diameter was approximately 300 μm. A coarse lamellar/Widmanstätten microstructure was also developed with lamellae of 15-20 μm width.
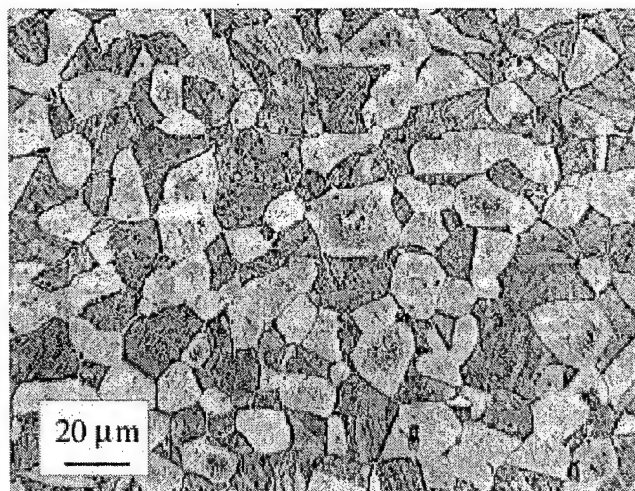
Figure 2-5: The bimodal microstructure of the coarse solution treated overaged material (Courtesy of C. S. Lee).

2.2   Experimental parameters

2.2.1   Control and instrumentation of major fretting fatigue variables

A fretting fatigue apparatus was created to achieve instrumentation and control over all critical fretting fatigue variables and is schematically shown in Figure 2-9. These variables include the normal load, the tangential load, the far-field applied bulk stresses, and the displacement. A detailed description of the fretting fatigue testing machine is given by Birch [30]. This machine departed from the bridge-pad geometry used in many previous studies. Rather a sphere-on-flat geometry was employed with the ability to remove a pad and replace it with a pad of a different radius. Initial validation of this machine was accomplished on Al 7075 T6 [44]. Upon validation, the next step was to proceed into the aggressive examination of fretting fatigue in Ti−6Al−4V. The fretting fatigue experimental machine was designed to instrument and control all of the major contact and bulk loading parameters in fretting fatigue.

The fretting pads are designed to be attached to the cylinder via a screw. This enables testing of pads of various radii. The normal load is applied using a spring attached to the load cell mounted on the end of the cylinder holding the pad. A butterfly screw is turned to increase or decrease the normal force.
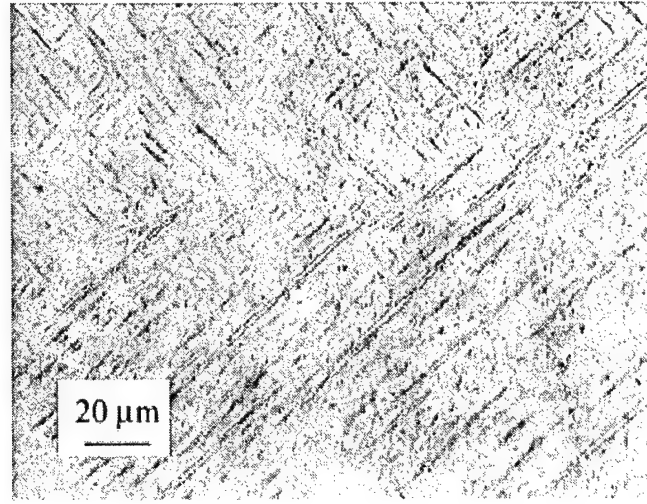
Figure 2-6: The martensitic material displayed a needle-like microstructure (Courtesy of C. S. Lee).

The uniaxial sinusoidal bulk load P is applied using an Instron® 8501 uniaxial tension/compression machine. The specimen is fixed at one end to a dye attached to a load cell. The other end of the specimen is fixed to the testing machine's actuator. Adjustment of the bulk load is very simple through the use of the Instron 8500 Plus control board.

The tangential load is developed by the application of a bulk load, P, causing a strain in the specimen. The frictional response to the strain is the tangential load. The compliance of the machine also affects the tangential load and this relationship is described by the following [20, 43, 30]:

$$Q = -\frac{C_{\mathrm{p}}}{C_{\mathrm{q}}}P \qquad (2.1)$$

where C_{p} is the compliance of the load train and C_{q} is the compliance of the tangential load. Replacing a stiff dye with a more compliant dye will increase the tangential load for a given bulk load, P, and a constant C_{q}. If the contacts are placed closer to the actuator, C_{p} will increase because the gauge length above the contact acts as a compliant spring. C_{q} can be varied by moving the supports that hold the flexible plates (and therefore the mountings, linear bearings, and pads) to the rigid base. By reducing the length of flexible plate between the support and the stiff base, C_{q} is decreased and Q will increase for a given P and C_{p}. C_{q} is
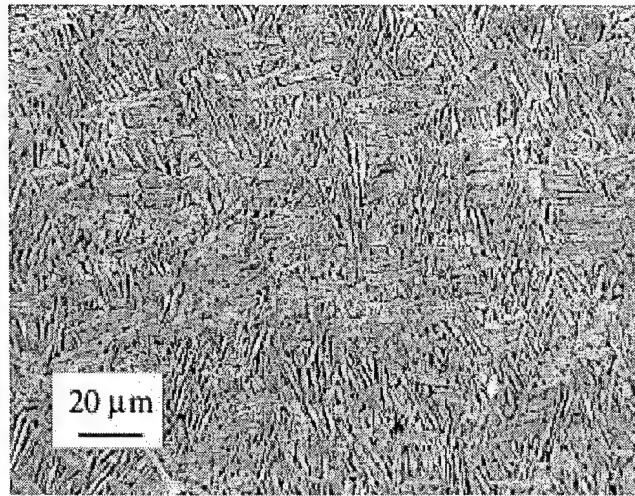
Figure 2-7: The colonies of lamellar structures are visible in this micrograph of the acicular material (Courtesy of C. S. Lee).

significantly influenced by the fit between the cylinder and the bearing and the quality of the bearing. A loose fit between the bearing and the cylinder will result in a reduced tangential load and an abnormal hysteresis loop (Q vs. P). C_q and C_p were never varied during the course of a fretting fatigue test. They would only be adjusted before a test. The tangential load is measured by two load cells separated equidistantly underneath the mount that contains the linear bearings. The sum of the loads upon the load cells equals the tangential load applied to the specimen.

The load cells were calibrated by the manufacturer and that calibration was verified using weights. The normal load and the tangential load could be measured to an accuracy of ±0.1 N. More realistically, the accuracy during actual testing operations was ±0.5 N.

The displacement is measured using an extensometer. The extensometer has two legs connected by a strain gauge. One leg is attached behind the pad and the other leg is attached to the specimen at a distance away from the region of contact. Utilizing information on the material's elastic modulus (assuming linear elasticity), the displacement can be obtained from the output of the strain gauge. The extensometer was used in the validation of the capabilities of this fretting machine [30], but was not used in this study of Ti−6Al−4V. The displacement is varied by adjusting the Q_{max}/N ratio. As Q_{max}/N is increased, the displacement increases
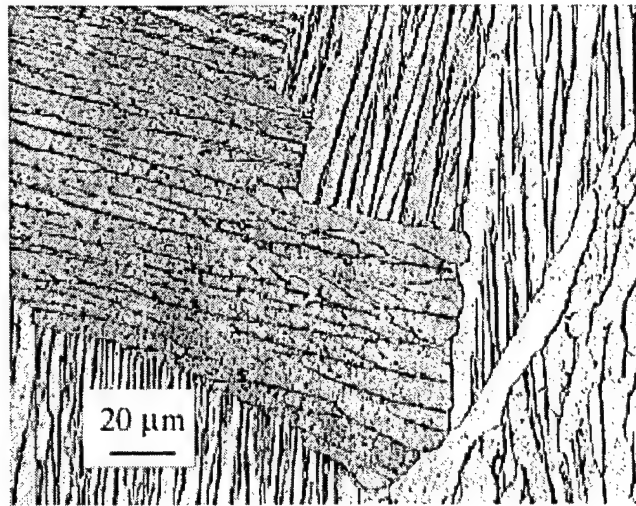
Figure 2-8: Coarse lamallae are very evident in this micrograph of the Widmanstätten microstructure (Courtesy of C. S. Lee).

until sliding occurs. Sliding will occur when Q_{max}/N exceeds the coefficient of breakaway friction.

The information from the load cells is sent to a nearby computer. A LABVIEW® program is used to process and display all of the data. All tests were conducted with a frequency of 10 Hz. Data is recorded at preset time intervals. Generally, the interval is every 100 minutes, but it depends on the anticipated length of the test. For example, friction tests are much shorter in duration, so 5 minute intervals or less are appropriate. The program will display several plots including the tangential load versus the axial load. During conditions of partial slip, the Q-P plot displays as thin closed hystersis loop. Once global sliding occurs, the Q-P hysteresis loop becomes a parallelogram.

The purpose of this study was to systematically vary these parameters and show their effect on fretting fatigue. Also, two pad radii were used. Although the effect of pad radius was not examined exhaustively, it was useful to investigate what occurs when certain contact loads are applied to different radii.
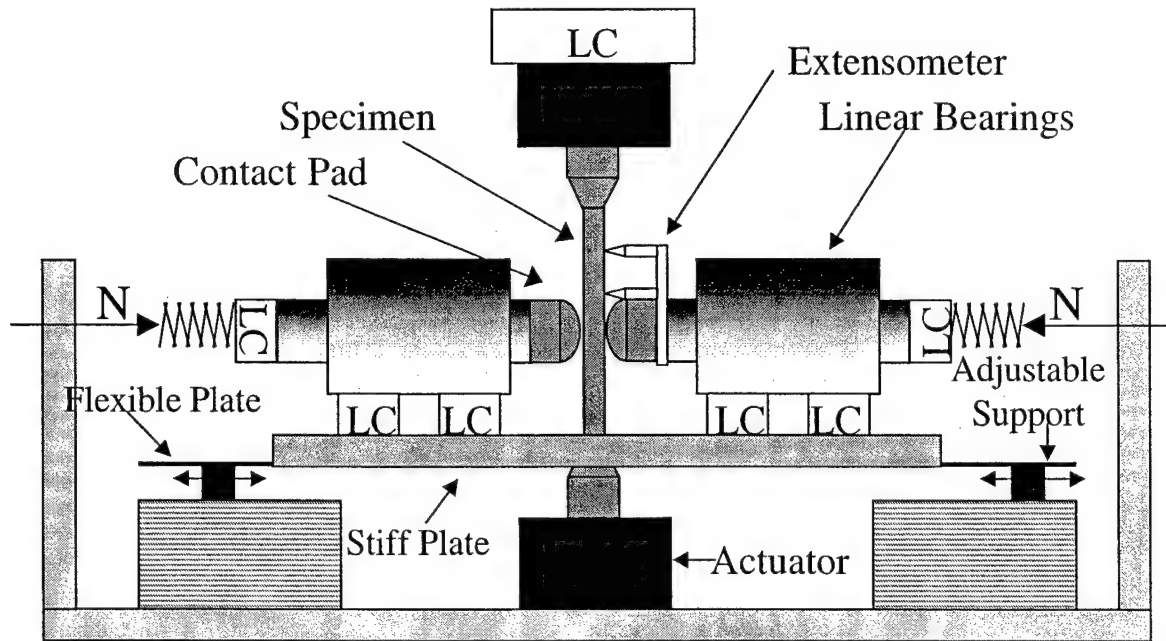
Figure 2-9: A schematic of the fretting fatigue testing machine (LC: load cell).

2.2.2 Specimen and pad dimensions

The contact pads were hemispheres made of Ti–6Al–4V with a radius, ρ, of 1.27 cm or 2.54 cm. The specimens had a gauge length of 5.2 cm and a square cross sectional area of approximately 22.7 mm^2 (3/16 inch by 3/16 inch). Care was taken to ensure that the width of each face of the specimen was longer than $6a_{contact}$ where $a_{contact}$ is the contact radius. Such a constraint on dimensions was necessary to prevent edge effects from interfering with the contact conditions [52]. Both the contacting pads and the specimens were of the same heat treatment. Photographs of the pads and specimens are shown in figures 2-10 & 2-11.

2.2.3 Testing conditions

All tests were conducted in air with 60-70% relative humidity at 25°C. The uniaxial bulk load was fully tensile to fully compressive (load ratio, $R = \min \sigma_b / \max \sigma_b$, of -1), and the maximum bulk stress never exceeded the endurance limit for this material. The test frequency was 10 Hz. Prior to every test, specimens were mechanically polished using 1200, 2400 and 4000 silicon carbide grit paper and 0.3 μm and 0.05 μm alumina. A surface roughness test was
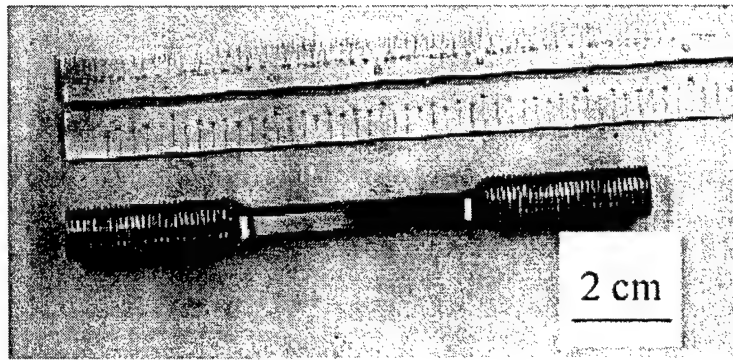
Figure 2-10: A photograph of a fretting fatigue specimen.

performed as part of a program with Los Alamos National Laboratory. The results showed an average surface roughness of 0.1 μm with a standard deviation of 0.02 μm. The root mean squared (rms) wavelength of roughness was anisotropic because the small thickness of the specimen hindered polishing across the specimen. The rms wavelength along the machining lines was 6.35 to 8.89 μm and across the machining lines was 1.91 to 3.18 μm. The direction of fretting was along the machining lines. The effect of the machining lines on the fretting is thus minimized [53].

For the mill annealed and STOA series, pads and specimens were of the same microstructure. In the tests involving other microstructures, the pads were STOA. In these series of tests, the elastic modulus of the pads and specimens were the same, but the hardness could be different.

At the beginning of each fretting fatigue test, the frequency was set to 1.0 Hz and the maximum load was 1.0 kN. After starting the test, the frequency was slowly ramped up to 10 Hz. Then the load was be slowly ramped up to the desired load necessary to produce the required bulk stresses. The ramping of the frequency and bulk load was conducted slow enough to maintain partial slip but quickly enough to avoid taking up too many cycles. This process would often take approximately 1,000 cycles.

The present approach is different from others where fretting tests are conducted so that testing begins at the desired frequency and load. For these approaches, the coefficient of friction within the stick-slip zone varies from the first cycle, until after many cycles a steady-state coefficient of friction is reached. Under such testing conditions, sliding will occur from

36
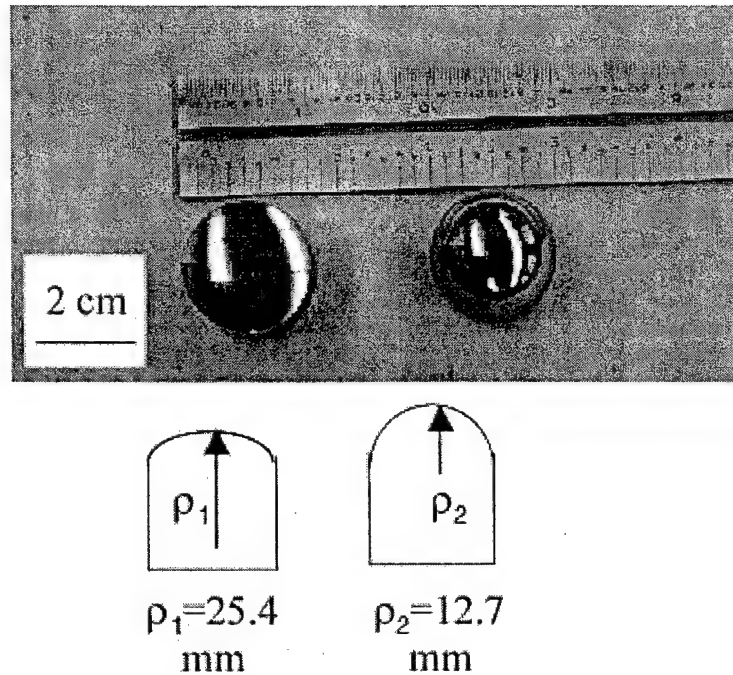
Figure 2-11: At the top is a photograph looking down on the 25.4 mm radius pad (left) and the 12.7 mm radius pad (right). The bottom of the figure is a schematic showing the radii of curvature from the side.

the onset of the test and then conditions of partial-slip will slowly develop together with light wearing [24]. This tribological effect was not noticed in the ramping sequence outlined above. Such differences in the loading history could have an effect on the reported coefficient of friction.

Chapter 3

Experimental results

The first section will be a description of the determination of the relevant coefficient of friction. Then, the results will be presented from the systematic variation of a particular load (either the applied bulk stress, the tangential load, and the normal load) while the other loads were held constant. Finally, fretting damage (scars and cracking) will be assessed.

3.1   Measuring friction

Under stick-slip contact conditions, a plot of the tangential load, Q, versus the bulk load, P, will form a closed hystersis loop. Once sliding occurs, the hystersis loop will open and will continue to open until it is shaped like a parallelogram. This condition is called global sliding and $Q_{\max}/N$ equals the coefficient of dynamic friction, μ_d.

To measure friction, fretting fatigue tests were conducted under conditions of stick-slip at a frequency of 1.0 Hz and a tangential load of 1.0 N. The applied normal load was chosen to be 10, 14, or 15 N. The frequency was ramped to 10 Hz, then the bulk load was slowly increased and as a result the tangential load increased until sliding occurred. The maximum tangential load, $Q_{\max}$, at the point just prior to sliding was recorded. This value of $Q_{\max}$ divided by the corresponding normal load is the breakaway coefficient of friction, μ_b. This value was measured to be 0.95 ± 0.1. As the tangential load was ramped, the size of the stick region decreased and surface modification occurred. The ratio $Q_{\max}/N$ at the point of breakaway is greater than that ratio once sliding is commenced. The coefficient of dynamic friction was

measured to be 0.7 ± 0.1. The measured values of the dynamic and breakaway coefficients of friction were unaffected by the magnitude of the normal load. The values of the coefficient of friction seem to be reasonable. Literature values for the coefficient of friction for Ti sliding against itself in air are near 0.6 [47]. Antoniou and Ratke [45] measured both the breakaway and the dynamic coefficients of friction for Ti–6Al–4V against Ti–17 and found them to be 0.85 and 0.7 respectively. However, these results do differ from those of Farris et al. [54] who determined a steady-state coefficient of friction of 0.5. This difference is probably due to the different initial loading history.
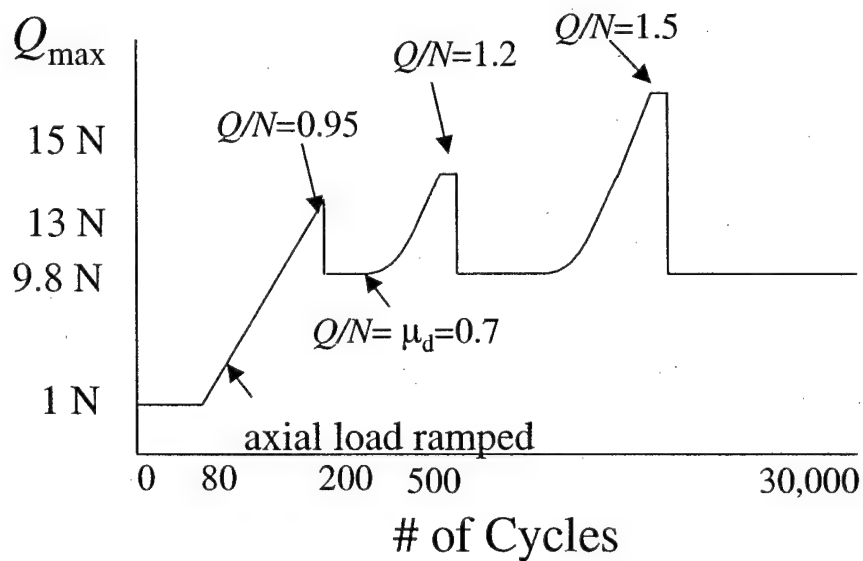
Figure 3-1: A schematic of the evolution of the tangential load as the bulk load is repetitively increased until sliding over several thousand cycles.

The evolution of the tangential load during one of the friction tests is shown schematically in figure 3-1. After one or two thousand cycles of sliding, stick-slip could return. This is the result of wear and debris on the surface. Increasing the bulk load would cause the tangential load to increase above $Q_{max}/N = 0.95$ until another breakaway would occur. After breakaway, global sliding would resume with tangential load reducing back to $Q_{max} = \mu_d N$. The process of stick-slip to sliding to stick-slip can occur several times. Each time the stick-slip Q_{max}/N becomes greater yet reducing to $Q_{max} = \mu_d N$ upon the resumption of sliding. The maximum

value of Q_{max}/N observed in stick-slip was 1.5. This process continues until the condition of global sliding becomes stable.

Another method of calculating the coefficient of friction comes from the measurement of fretting scars. The dimensions of the contact radius and the stick zone radius were taken from specimens and pads from interrupted tests, tests that did not fail and tests which led to failure but the scar was relatively undamaged. Figure 3-2 shows the scar measurements and the Mindlin function plotted as $c_{contact}/a_{contact}$ versus $Q_{max}/\mu N$. $c_{contact}$ and $a_{contact}$ were measured while Q_{max} and N were measured during the fretting fatigue test. The results are plotted for both the dynamic and breakaway coefficients of friction and fit the Mindlin curve very well for $\mu = \mu_b = 0.95$. This value is most representative of the steady-state coefficient of friction in the slip-zone. From this point in this paper, the value of the coefficient of kinetic friction (μ_b=0.95) will be used in the presentation of experimental results as μ.
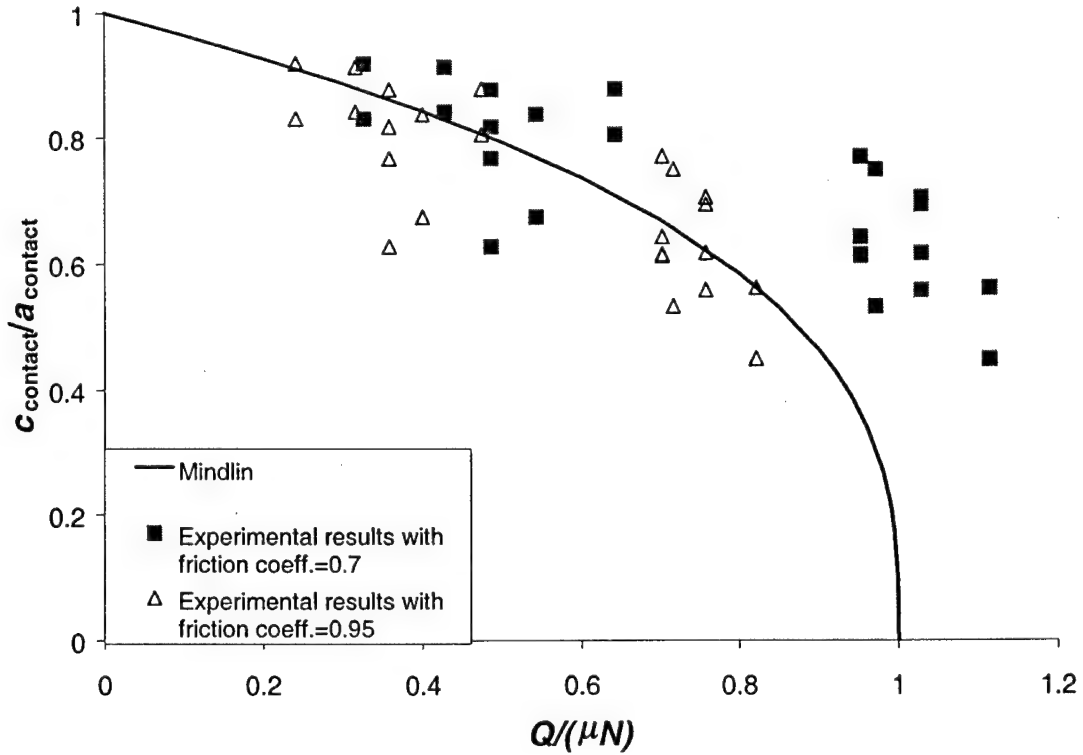
Figure 3-2: Scar measurements plotted as $c_{contact}/a_{contact}$ versus $Q/(\mu N)$ for $\mu = 0.7$ and $\mu = 0.95$ shows that the relevant coefficient of friction is the breakaway coefficient of friction.

If a fretting experiment starts without ramping (i.e. at high frequency and tangential load) such as the experiments conducted by Farris et al., there will be an initial coefficient of friction that is uniform over the entire contact area. However, surface modification in the slip zone will lead to an increase in the coefficient of friction in the slip zone while the friction in the stick zone will remain at the initial value. The size of the slip zone will decrease from the initial size and the value of the coefficient of friction between the new and the old stick-slip boundaries will remain indeterminate. The friction in the slip zone varies with the number of cycles until a steady-state coefficient of friction is reached after several hundred cycles. To determine the friction in the slip zone, one must fretting for n cycles and stop. The tangential load should then be increased until sliding to determine the mean value of friction. From the measured value of friction, the value of friction in the slip zone for n cycles can be determined. The coefficient of friction in the slip zone will vary as a function of the number of cycles until a steady state is reached [24]. This loading sequence as well as the resulting surface tribology differs from the method used in the current program. Ramping the loads and frequency modifies the surface throughout the loading sequence until the desired value of loading is reached. Thus, steady-state is reached almost immediately upon achieving the desired tangential load.

3.2 Effect of the bulk stress for various constant contact conditions

Bulk stress versus number of cycles to failure curves were produced by varying the maximum bulk stress while maintaining constant contact conditions. Four different parameters of constant contact conditions were applied. The first constant contact condition was $Q_{max} = 15$ N, $N = 50$ N and $\rho = 25.4$ mm. The results are recorded in table 3-1 and are shown in figure 3-3 where the fretting results are compared to plain fatigue data [47]. There is a significant decrease in the fatigue strength (called the "knockdown" effect) of the material as compared with plain fatigue. The contact conditions clearly initiate cracking at much lower bulk loading than plain fatigue. This is similar to the fatigue effect of notches. Notice that the maximum bulk stress for every fretting experiment is well below the endurance limit for this material. Also plotted is the curve for $Q_{max} = 30$ N showing that the fatigue life is further reduced if

Q_{max} is increased. The effect of the tangential load will be discussed in detail below.
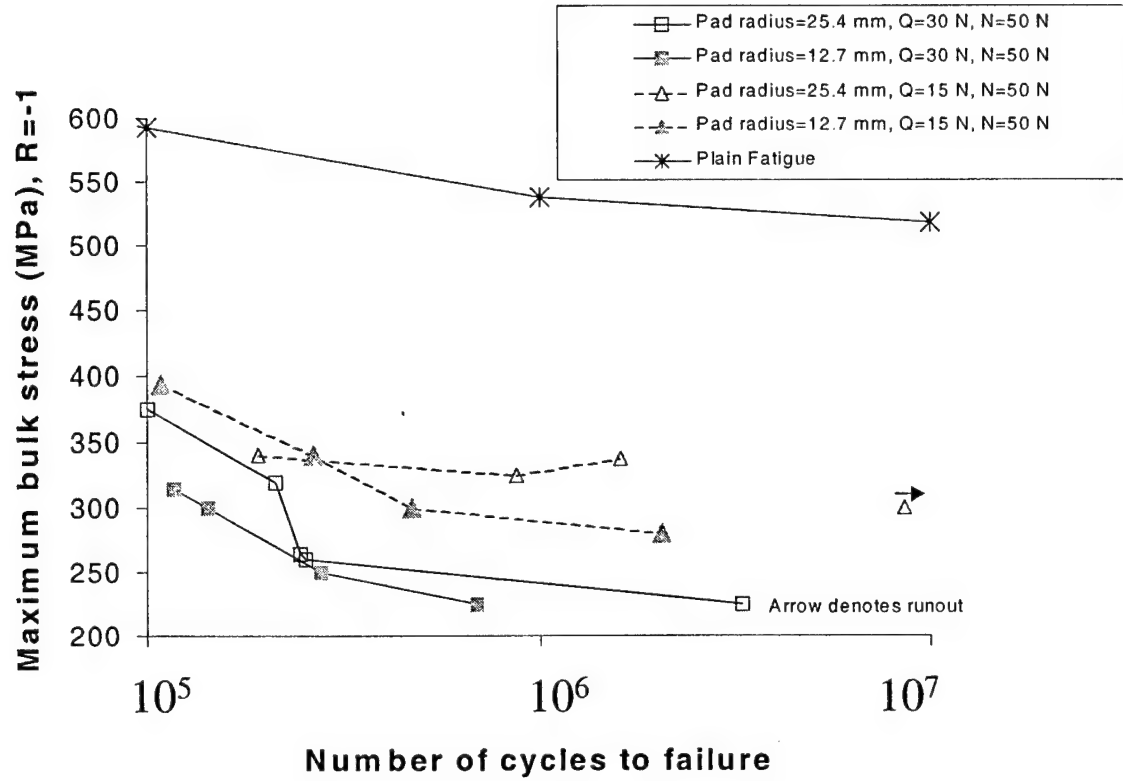
Figure 3-3: A plot of the fretting fatigue results showing the maximum bulk stress versus the number of cycles to failure. Pads and specimens were both mill annealed.

A continuation of the series above was performed for pad radius of $\rho = 12.7$ mm. It was apparent that a decrease in the pad radius increases the knockdown factor. This also holds true for $\rho = 12.7$ mm and $Q_{\mathrm{max}} = 30$ N. This is explained in more detail when contact stresses are addressed.

3.3   Effect of the tangential load

A series of tests was performed with a maximum applied bulk stress of 300 MPa, normal force of 50 N, and contact pad radius of $\rho = 12.7$ mm. The results are recorded in tables 3-2, 3-3, 3-4 and 3-5 plotted in figure 3-4 showing the maximum tangential load normalized by the normal

	σ_{b} (MPa)	Q (N)	N (N)	ρ (mm)	N_{f}	Result
B1	394	14.5	50	12.7	107899	failed
B2	357	13	50	12.7	31540	interrupted
B3	341	15	50	12.7	266176	failed
B4	300	14.5	50	12.7	474656	failed
B5	280	15	50	12.7	2055856	failed
B6	341	15	50	25.4	192000	failed
B7	325	15	50	25.4	872,863	failed
B8	338	15	50	25.4	1,609,238	failed
B9	300	17	50	25.4	8,596,572	no failure
B10	292	15	50	25.4	3,962,688	failed
B11	276	15	50	25.4	4,273,718	no failure
B12	254	16	50	25.4	2,288,839	no failure
B13	315	30	50	12.7	117,183	failed
B14	300	30	50	12.7	142,746	failed
B15	250	30	50	12.7	278,238	failed
B16	225	33	50	12.7	691,612	failed
B17	375	30	50	25.4	85,957	failed
B18	320	30	50	25.4	212,491	failed
B19	265	30	50	25.4	245,637	failed
B20	260	30	50	25.4	253,700	failed
B21	225	30	50	25.4	3,295,860	failed

Table 3.1: Fretting fatigue results from varying bulk stresses for constant contact conditions.

load on the y-axis and the number of cycles to failure on the x-axis. The maximum tangential load was varied for each test by changing either the compliance of the bulk load train C_{p} or the compliance of the tangential load train, C_{q}.
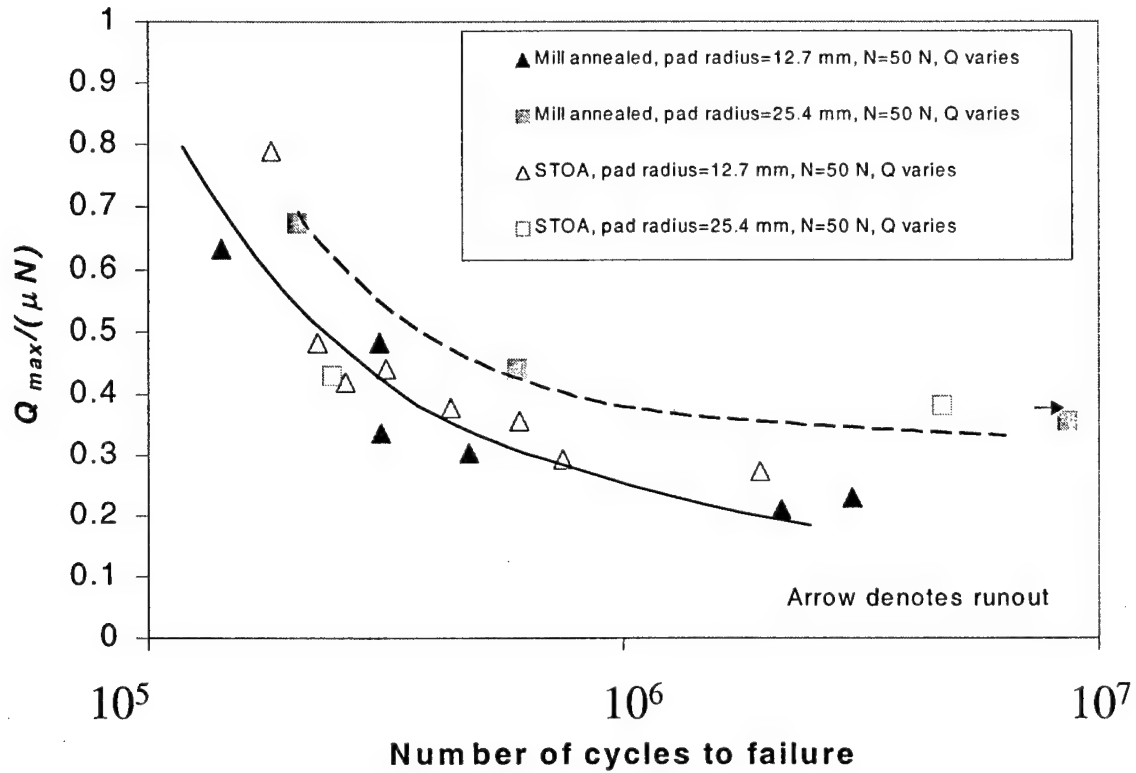
Figure 3-4: A plot of the fretting fatigue results for varying the tangential loading ($N = 50$ N and $\sigma_{\mathrm{b}} = 300$ MPa) showing $Q_{\mathrm{max}}/(\mu N)$ ($\mu = 0.95$) versus number of cycles to failure. Results are shown for both the mill annealed and solution treated overaged material. A trendline is shown for the results for $\rho = 12.7$ mm (solid line) and for $\rho = 25.4$ mm (dotted line).

A clear relationship is established between Q_{max}/N and the number of cycles to failure. As the tangential load is increased, life is reduced significantly as Q_{max}/N approaches μ_{b} (incipient sliding). This series of tests was repeated for a pad radius of 25.4 mm. The fatigue strength of the material increased due to the increase of the pad radius.

Tests were performed for both the mill annealed and STOA materials. The trends involving Q_{max}/N and the pad radii are evident in both microstructures. It appears that the STOA

44

	σ_b (MPa)	Q (N)	N (N)	ρ (mm)	N_f	Result
T1	300	30	50	12.7	142,746	failed
T2	300	23	50	12.7	307,653	failed
T3	300	14.5	50	12.7	474,656	failed
T4	300	11	50	12.7	3,057,892	failed
T5	300	10	50	12.7	2,163,277	failed

Table 3.2: Fretting fatigue conditions and results for the effect of tangential loading with 12.7 mm radius pads and mill annealed material.

	σ_b (MPa)	Q (N)	N (N)	ρ (mm)	N_f	Result
T6	300	13	50	12.7	1,955,612	failed
T7	300	14	50	12.7	745,000	failed
T8	300	18	50	12.7	433,195	failed
T9	300	23	50	12.7	227,972	failed
T10	300	21	50	12.7	317,073	failed
T11	300	17	50	12.7	605,023	failed
T12	300	37.5	50	12.7	182,617	failed
T13	300	20	50	12.7	260,894	failed

Table 3.3: Fretting fatigue conditions and results for the effect of tangential loading with 12.7 mm radius pads and STOA material.

material has a slight improvement in fretting resistance.

3.4   Effect of the normal load

The effect of the normal load was demonstrated by varying the normal load while applying a maximum bulk stress of 300 MPa, a tangential load of 16 N, and a contact pad radius of $\rho = 12.7$ mm. Varying the normal load produces the dual effect of changing the contact pressure and the contact length scale. The results of this series of tests are recorded in tables 3–6 & 3-8 and

	σ_b (MPa)	Q (N)	N (N)	ρ (mm)	N_f	Result
T14	300	21	50	25.4	598,191	failed
T15	300	17	50	25.4	8,596,572	no failure
T16	300	32	50	25.4	207,258	failed

Table 3.4: Fretting fatigue conditions and results for the effect of tangential loading with 25.4 mm radius pads and mill annealed material.

	σ_b (MPa)	Q (N)	N (N)	ρ (mm)	N_f	Result
T17	300	20.5	50	25.4	244,054	failed
T18	300	18.25	50	25.4	4,708,273	failed

Table 3.5: Fretting fatigue conditions and results for the effect of tangential loading with 25,4 mm radius pads and STOA material.

	σ_b (MPa)	Q (N)	N (N)	ρ (mm)	N_f	Result
N1	300	14.5	50	12.7	474,656	failed
N2	300	16	40	12.7	401,153	failed
N3	300	16	30	12.7	499,291	failed
N4	300	15	22	12.7	284,670	failed
N5	300	16.25	60	12.7	1,235,575	failed
N6	300	16.5	70	12.7	2,969,846	failed

Table 3.6: Fretting fatigue results for varying the normal load with a 12.7 pad radius and mill annealed material.

are plotted (see figure 3-5) in the same manner as the tests above.

Increasing the normal load causes a minor increase in total life for $Q_{max}/(\mu N)$ above 0.4. This trend is due to the increase in contact radius as the normal load increases and will be explained in more detail when the contact stresses are discussed below. However, the radius of the stick zone also increases and approaches the contact radius as long as the tangential load is roughly held constant for all tests. As will be discussed soon, using the equations of Chivers and Gordelier [39], the stress at the trailing edge decreases as N is increased and Q_{max} remains constant. However, the trend for $Q_{max}/(\mu N) < 0.3$ is not explained well by the stress relations. It appears that an endurance limit is being approached.

The same series of tests were performed for a pad radius of $\rho = 25.4$ mm. For this tangential loading, increasing the pad radius significantly increased the fatigue strength of the material.

	σ_b (MPa)	Q (N)	N (N)	ρ (mm)	N_f	Result
N7	300	17	30	25.4	5,342,499	failed
N8	300	17	25	25.4	12,000,000	no failure
N9	300	17	50	25.4	8,596,572	no failure

Table 3.7: Fretting fatigue results for varying the normal load with a 25.4 pad radius and mill annealed material.
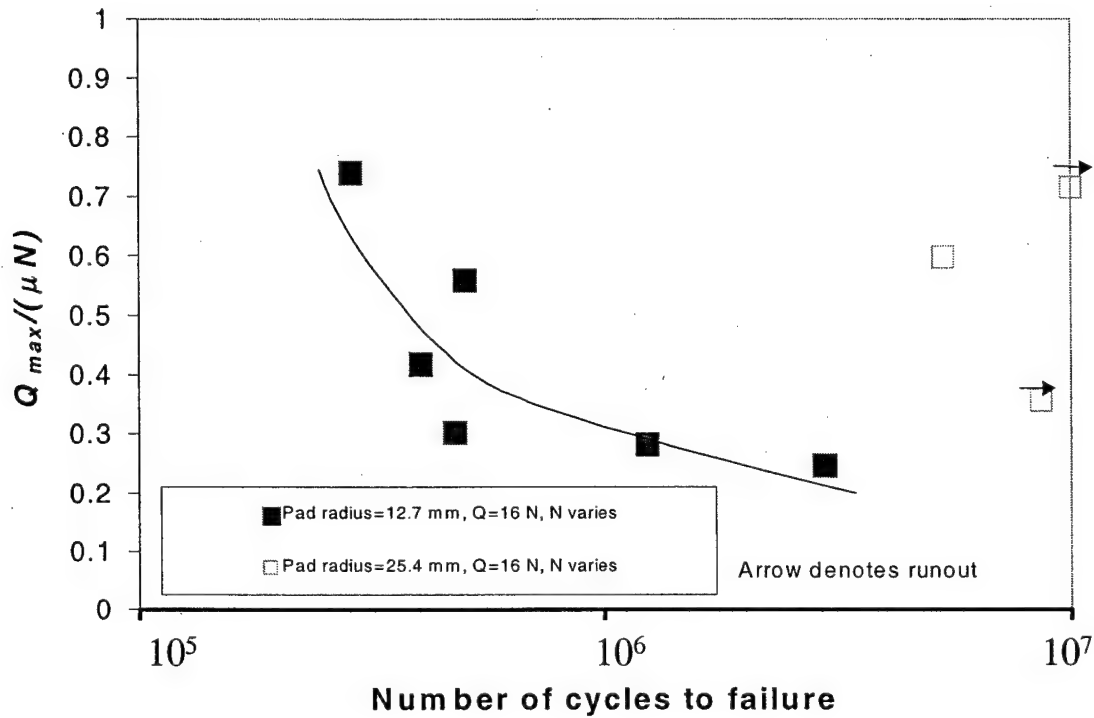
Figure 3-5: A plot of the fretting fatigue results for varying the normal loading ($Q_{\text{max}} = 50$ N and $\sigma_{\text{b}} = 300$ MPa) showing $Q_{\text{max}}/(\mu N)$ ($\mu = 0.95$) versus number of cycles to failure. A trendline is shown for the results for $\rho = 12.7$ mm. Pads and specimens were mill annealed.

3.5 Effect of the microstructure

Several microstructures were examined under constant contact conditions and a maximum bulk stress of 300 MPa. The applied normal load was 50 N, the fretting pad was a STOA pad with $\rho = 12.7$ mm and the tangential load was varied. Therefore, the results are shown with the full range of Q_{max}/N fretting fatigue tests for the STOA and mill annealed microstructures. The results presented in table 3-8 and are plotted in figure 3-6 with respect to Q_{max}/N because the coefficient of friction was not determined for each microstructure.

The performance of most microstructures was within the scatter of the STOA and mill annealed microstructures. The martensitic microstructure had a marked improvement in fretting
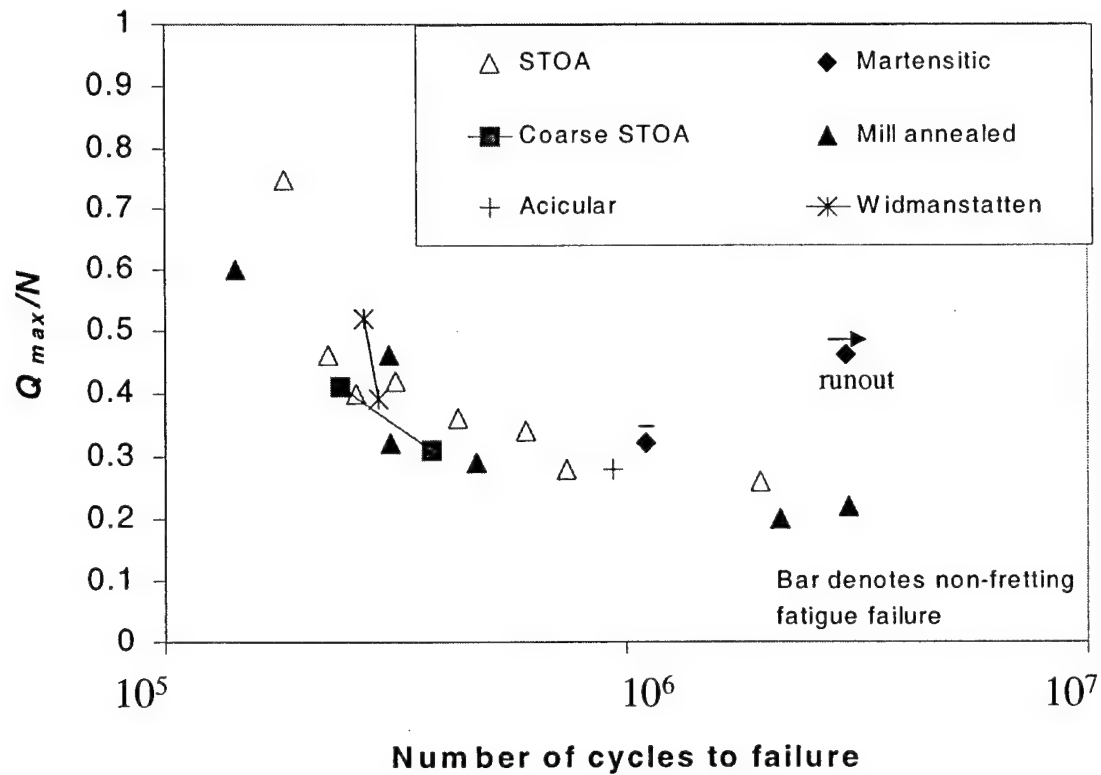
Figure 3-6: A plot of the fretting fatigue results for the microstructural variation for varying the tangential load $N = 50$ N, $\rho = 12.7$ mm and $\sigma_b = 300$ MPa and showing Q_{max}/N versus number of cycles to failure.

fatigue performance. One of the martensitic structures failed due to plain fatigue away from the contact region. The cause of that failure was undetermined. The martensitic microstructure appeared to have improved resistance to contact fatigue, yet the microstructure is brittle material.

The fracture surfaces were examined optically. The mill annealed and STOA specimens had relatively smooth fracture surfaces. The Widmanstätten and lamellar specimens had rough fracture surfaces. The roughness on the fracture surface of the Widmanstätten specimens made it impossible to determine the initial region III crack size. In the case of the lamellar microstructures, the colony size and the grain size may have influenced fatigue crack growth properties. The fact that most microstructures had fatigue performances close to that of

48

	σ_b (MPa)	Q (N)	N (N)	ρ (mm)	N_f	Result
Martensitic 1	300	16	50	12.7	1,100,649	failed
Martensitic 2	300	24	50	12.7	4,720,061	no failure
Coarse STOA 1	300	15.5	50	12.7	378,782	failed
Coarse STOA 2	300	20.5	50	12.7	240,501	failed
Widmanstätten 1	300	19.5	50	12.7	290,286	failed
Widmanstätten 2	300	26	50	12.7	271,576	failed
Acicular	300	14	50	12.7	936,000	failed

Table 3.8: Fretting fatigue results for various microstructure and a pad radius of 12.7 mm.

the mill annealed and STOA variants may indicate that the influences of respective fatigue crack growth, contact resistance, and crack initiation resistance may have canceled out. The exception, of course, is the martensitic material.

The Vickers hardness (HV) was determined for each microstructure and the results plotted in a bar graph in figure 3-7. A force of 0.1 kg was applied to the pyramid hardness indenter. Ignoring the sink-in or pile-up at the contact perimenter, the Vickers hardness is determined by the following relation [55]

$$HV = \frac{1.854N}{L^2}$$

where N is the applied normal load on the indenter in kg (equal to 0.1 kg in this case) and L is the average length of the diagonals in mm. The mill annealed microstructure was tested in both the cross-sectional and longitudinal directions and it was found that the texture did not affect the hardness; the microstructure with the highest hardness had the highest fretting resistance. The martensite had the largest HV value at 401 kg/mm^2 while the coarse STOA had the smallest value with 331 kg/mm^2. For HV=340 kg/mm^2, the area of the indentation would be 2.72×10^{-10} m^2 and the side of the indentation would be 16.5 μm. Thus, the indentation would only cover a few grains, therefore these hardness results must be approached carefully. It appears that the hardness may have an effect on the fretting resistance. However, a martensitic microstructure tends to be brittle. If close control of the microstructural properties can be achieved, an optimal fretting fatigue resistant Ti−6Al−4V component would have a martensitic surface around a core of a different microstructure.
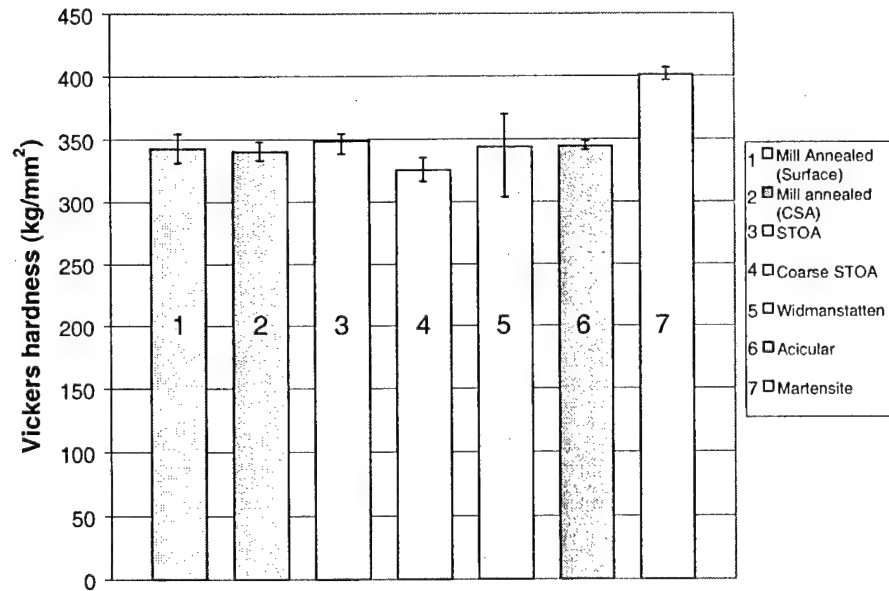
Figure 3-7: The average Vickers hardness for each microstructure (Courtesy of C. S. Lee).

3.6 Fretting scars

Slip produces oxides as fresh layers of the surface are exposed. If the fretting is stopped and the pads are removed, a characteristic scar will remain with the slip annulus covered by oxides. If a test leads to failure, severe damage can occur to the scar when the specimen slides immediately following fracture. However, interrupting the test allows examination of an undamaged scar. Figure 3-8 shows the fretting scar on the pad together with the theoretical region of slip and theoretical contact region. Theory predicts $a_{contact} = 244$ μm, $c_{contact} = 152$ μm and $e = 54$ μm. The measured values are $a_{contact} = 238$ μm, $c_{contact} = 179$ μm and $e = 31$ μm. Eccentricity is noticed since the slip annulus at the trailing edge of contact is wider. Distortion at the periphery of the contact is due to surface roughness and oxides being kicked out behind the contact. The scar on the pad is the mirror image of the scar on the specimen. The scar on the specimen is shown in figure 3-9.

A typical scar was examined using backscatter scattering electron microscopy (SEM) to qualitatively determine some of the oxide charactersitics. The slip zone contained a region that is rich in oxygen and maintains concentrations of Ti, Al, and V at ratios comparable to

50
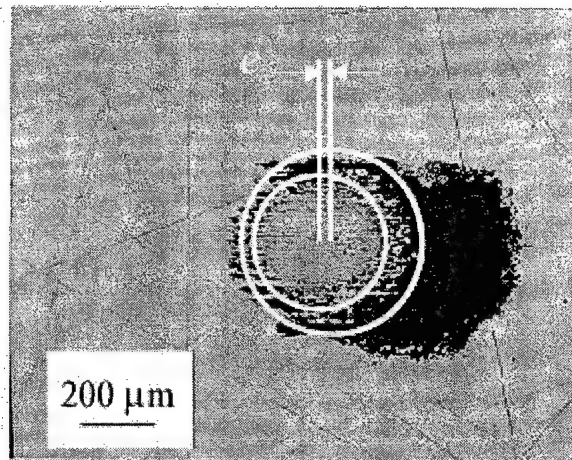
Figure 3-8: Fretting fatigue scar on a contact pad from a test that was interrupted at 36,000 cycles with a pad radius of 12.7 mm and a load of $N = 50$ N, $Q = 36$ N and $\sigma_b = 300$ MPa. Oxides cover the slip zone and have flowed to the right of the scar because of gravity. The actuator would be to the right, so the trailing edge is on the right side. The measured contact radius was 238 μm, stick zone was 179 μm and the eccentricity was $e = 31$ μm.

that in the bulk material. For more quantitative analysis of the oxide composition, other microprobe methods must be used since oxygen is a difficult element for backscatter SEM to interpret. These microprobe methods were not used in this work.

The oxides found in the slip zone had very strong adherence to the specimen. Three methods were used for removing oxides: wiping the surface with acetone, ultrasonic cleaning in acetone bath for 1.5 hours, and polishing with 0.05μm and 0.3 μm alumina. None of the methods effectively removed the oxides. This adhesion affects the contact characteristics of the fretting.

The eccentricity was measured for several interrupted tests and in the few cases where the scar was relatively undamaged after failure. These values are shown in Table 3-9 and compared to the predicted values for the coefficient of friction $\mu = 0.95$, using eq. (1.5). The predicted values of eccentricity agree well with the experimental values for a pad radius of 12.7 mm. For the pad radius of 25.4 mm, the values appear to be a factor of 2 less than the predicted value. Thus, there appears to be a size effect. All other factors in eq. (1.5) contribute a maximum 20% error, assuming the coefficient of friction does not change. Therefore, the value of μ
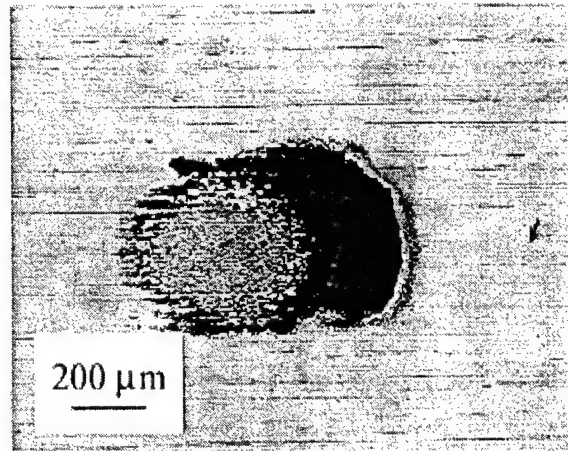
Figure 3-9: The fretting fatigue scar on the specimen for the same experiment is a mirror image of the one on the pad (corresponding to Fig. 3-8).

utilized for eq. (1.5) depends on the pad radii. If the eccentricity develops during the first cycle, the relevant coefficient of friction may be a strong function of the adhesion between the two contacting Ti-6Al-4V surfaces prior to the development of oxides *and* prior to slip. The total energy of debonding would have a greater magnitude as the pad radius increases since the total contact length also increases, therefore explaining why μ in eq. (1.5) would be larger for the 25.4 mm pad radius than the 12.7 mm pad radius. Further discussion on adhesion and the debonding energy will be given in Section 4.4.

3.7 Location and shape of cracks

Experimental observation of many specimens from tests that either failed or were interrupted determined the location of cracking to be near the trailing edge or in the slip zone near the trailing edge. Post-mortem analysis using an optical microscope revealed three clear instances of crack linkage from two initiation sites. Figures 3-10 & 3-11 show the contact regions on a mill annealed specimen and an STOA specimen, respectively. These tests were interrupted at 90% of the expected number of cycles to failure. Both images show cracks located at the edge of contact. The STOA specimen was sectioned along the x-axis after a test was interrupted at 360,000 cycles. Polishing and etching was performed in the same manner as the micrographs

52

Test	Material	σ_b (MPa)	Q (N)	N (N)	ρ (mm)	$a_{c,p}$	$a_{c,m}$	$c_{c,p}$	$c_{c,m}$	e_p	e_m
I1 (right)	MA	300	36	50	25.4	244	238	152	179	54.2	31
I1 (left)	MA	300	36	50	25.4	244	253	152	167	54.2	13.3
I2 (right)	MA	300	22.5	50	25.4	244	253	197	206	54.2	26.7
I2 (left)	MA	300	22.5	50	25.4	244	273	197	193	54.2	26.7
I3	STOA	300	17	50	12.7	194	200	167	143	27.1	20
I4	MA	300	17	50	12.7	194	220	167	200	27.1	23.3
T7	STOA	300	19.5	50	12.7	194	185	172	125	27.1	23.8
T11	STOA	300	17	50	12.7	194	200	167	133	27.1	66.7
N8	MA	300	17	25	25.4	194	200	127	173	54.2	26.7

Table 3.9: Predicted versus measured values of the contact radius, stick zone radius (values given in microns) and eccentricity for several interrupted tests and tests where the scar remained intact after failure (coefficient of friction is 0.95 and Poisson's ratio is 0.34). In some cases, both sides of the specimen were measured. MA=mill annealed, c=contact, p=predicted and m=measured

in section 2.1.7. Figure 3-12 shows the region near the trailing edge of the contact where two cracks can be seen. One crack is at the edge of contact, and the other is just behind the edge of contact. The crack just beyond the edge of the contact branched and subsequently arrested at a depth of 50 μm. Both cracks entered into the material at a steep angle.
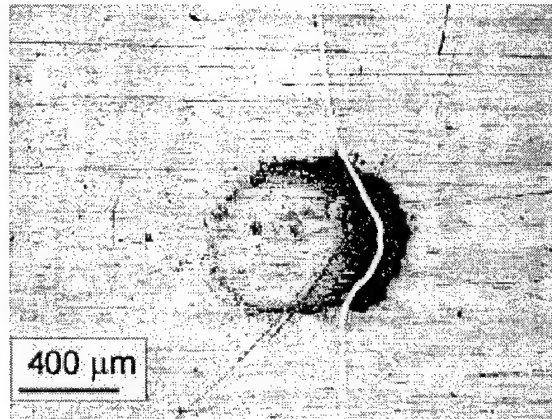
Figure 3-10: A crack is highlighted by a white line on a mill annealed specimen from an experiment which was interrupted at 290,000 cycles with a pad radius of 12.7 mm and a load of $N = 50$ N, $Q_{max} = 21$ N and $\sigma_b = 300$ MPa.

From the many observations of fretting initiated cracking, the following statements can be
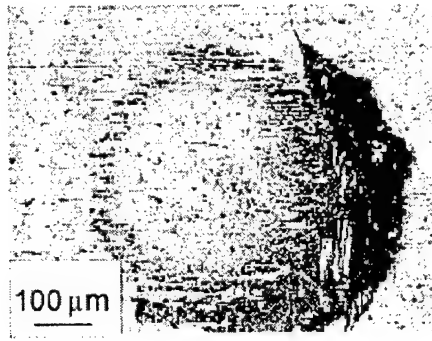
Figure 3-11: An interrupted experiment on STOA material reveals a crack at the edge of contact for a test interrupted at 360,000 cycles with a pad radius of 12.7 mm and a load of $N = 50$ N, $Q_{max} = 10$ N, and $\sigma_b = 300$ MPa.

made about the various stages of fretting fatigue crack growth.

The various regions of fretting fatigue crack growth can be recognized in the fractography. For region I, the location of initiation is at or near the edge of contact with multiple crack initiations along the x-axis. One specimen did indicate that cracks did not just initiate at the intersection of the trailing edge and the x-axis but also at many sites along the radius of the edge of contact near the trailing edge. Viewing the contact surface from above (see figure 3-13) shows that region II crack growth consists of the crack traveling around the contact region. In a three dimensional sense, the crack is growing in the shape of a half-funnel. Away from the contact surface, the contact stresses drop sufficiently compared to the bulk stresses and the crack will propagate solely in the y-z plane. It is interesting to note that in the absence of a fatigue bulk stress, cracks would initiate and grow from opposite sides of the contact and form an eyelid shape around the contact [56]. The presence of a fatigue bulk stress in-phase with the contact loading will inhibit the formation of a crack on the side furthest from the actuator. That location is the trailing edge of contact when the actuator is applying a compressive load.

Post-failure optical examination of each specimen was conducted utilizing a microscope to determine the dimensions of the crack. The ratio of the length of the semielliptical crack (a) versus the half-width (c) could be found by viewing the fracture surface near the point of contact. At that location it is quite simple to measure the initial crack length, a_o, and initial crack width, c_o, for region III. The region II portion of the crack would be outside of the focal
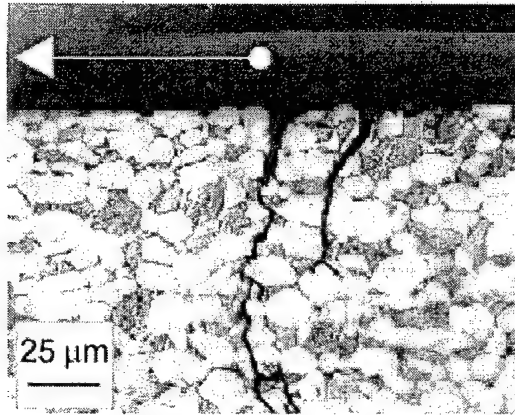
Figure 3-12: Fretting fatigue cracks from the experiment shown in figure 3-11 initiated near the edge of the contact zone (marked with an arrow). One crack is arrested at a depth of 50 microns. The other would have propagated to failure.

view of the microscope and will appear as a thumbnail shape. The thumbnail shape is clearly shown in figure 3-14. The crack will maintain its shape as it propagates, $a/c = a_o/c_o$. The ratio of a/c was typically near 0.7.

Conducting fractographic observations via sectioning was difficult. The section must be made perfectly along the x-axis of the contact surface. Since the contact region is very small, making such a cut was difficult. The only time such a cut was made in this study is shown in the micrograph in figure 3-12. To further determine crack entrance angles from failed specimens, the following method was employed using an optical microscope. First, wherever possible, the point of initiation was determined. Then, the distance of that point to the location at which the crack turned normal to the bulk stresses, l_x, was measured (see figure 3-15). Finally, this length and the initial region III crack length are utilized to determine the crack entrance angle.

$$\Theta = \arctan\left(\frac{a_o}{l_x}\right)$$

The typical crack entrance angle was 70°. This value agrees well with the steep angles shown in figure 3-12. This method of measuring the crack entrance angle assumes that the crack is traveling in a straight line through region II. In reality, the crack is turning as it enters into the bulk [45]. The measurements of the initial region III crack size and the angle of crack entrance

55
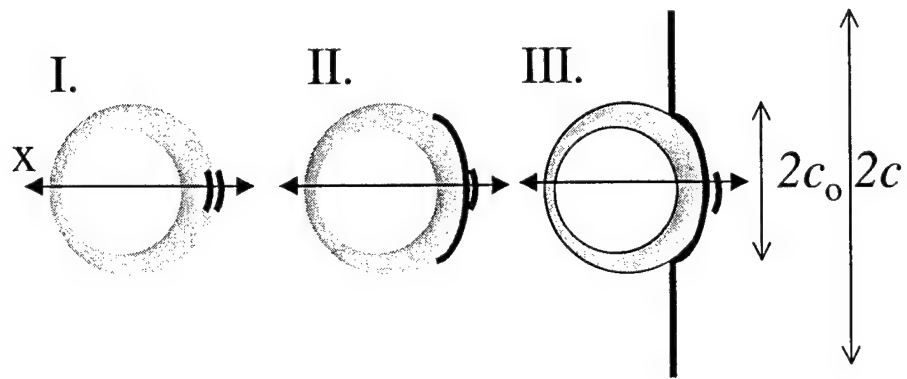
Figure 3-13: A view looking down at the fretting scar showing regions I, II and III of fretting fatigue crack growth.

are given in a Appendix A.
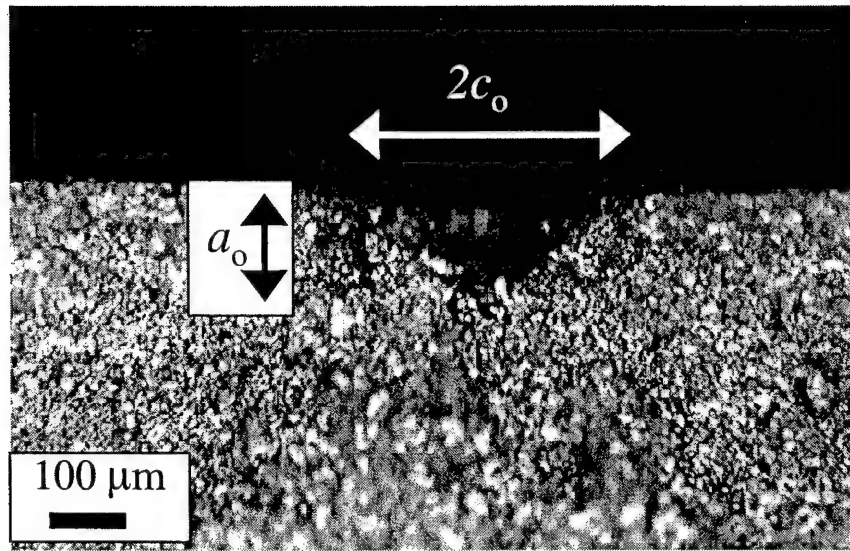
Figure 3-14: The initial region III crack dimensions ($a_o = 160$ μm and $c_o = 228$ μm) are clearly seen in this photograph of the fracture surface of a fretting fatigue test on an STOA specimen with $\rho = 12.7$ mm, $N = 50$ N, $Q = 20$ N, $\sigma_b = 300$ MPa, and $N_f = 260,874$ cycles.
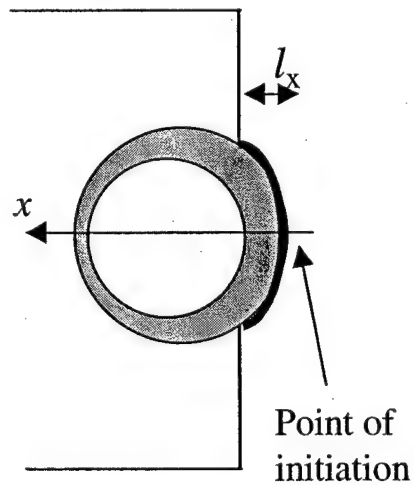
Figure 3-15: A schematic showing how to measure l_x from the post-failure surface of a specimen.

Chapter 4

Analysis

A variety of approaches can be taken toward analyzing crack initiation and propagation because of fretting fatigue. One straightforward way would be to examine the contact stresses. The Hertzian contact produces stress concentrations similar to a notch. It is advantageous to this study that the stresses beneath a Hertzian contact are well known analytically. The stresses beneath more complex geometries can be determined using FEM. Thus, a stress-based approach to fretting fatigue crack initiation hold some promise. One can expect that locating the maximum stresses can lead to finding the location of crack initiation. Yet, that connection between initiation location and stress concentration may be not as straightforward as it sounds. Ultimately, contact fatigue is more complex than ordinary fatigue. Nonetheless, it is important to consider a stress-based approach to fretting fatigue crack initiation, and a multiaxial stress-based criterion is developed and employed in this chapter.

A second approach to fretting fatigue is through fracture mechanics. Fatigue crack propagation as well as life-prediction are easily characterized by fracture mechanics. Indeed, a section of this chapter is devoted to calculating region III propagation life, subtracting that life from total life and making statements about crack initiation. There is little question that a fracture mechanics methodology to contact fatigue is advantageous. However, a connection must be made between aspects of contact mechanics and fracture mechanics. In the case of the sphere-on-flat geometry, this connection is made through interfacial adhesion. The adhesion model is employed in this chapter to determine a contact fatigue threshold and to establish a life prediction methodology.

4.1 Determining number of cycles spent in regions I and II of fretting fatigue crack propagation

The number of cycles due to crack propagation can be determined from knowing the relevant stress intensity factors, crack lengths and crack growth rates in Ti–6Al–4V. This approach will use the following steps:

1) Upon turning normal to the bulk stresses, the crack has a semi-elliptical shape. The stress-intensity factor for such a surface crack has been determined by Newman and Raju [57]. From that stress-intensity factor, it can be determined if the crack is greater than the long crack fatigue threshold for the material. If so, we can proceed to the next step. If not, we can determine if the crack size exceeds the short crack growth threshold for this material.

2) Integrate Paris law crack growth relationship to determine the number of cycles the crack spends propagating under the bulk load, σ_b. The constants in the Paris law, if not known, must be experimentally determined.

3) Once the propagation life is determined, one can subtract it from the total life of a specimen to determine the number of cycles the crack spends in region I and II (see figure 1-3 for the regions of fretting fatigue crack growth). It is assumed here that the number of cycles spent in fast fracture (region IV) is negligible compared to the number of cycles spent in all other regions. This can be summarized in the relationship:

$$N_{\text{I\&II}} = N_{\text{f}} - N_{\text{III}}, \ N_{\text{IV}} \approx 0 \tag{4.1}$$

where $N_{\text{I\&II}}$ is the number of cycles spent in regions I and II, N_{f} is the total number of cycles to failure, N_{III} is the number of cycles spent in region III and N_{IV} is the number of cycles spent in region IV.

As stated above, the crack produced by fretting fatigue is a surface elliptical crack shown schematically in figure 4-1. The stress intensity factor for such a crack was derived by Newman and Raju [57]. For a finite plate the stress intensity factor is given by

$$K_{\text{I}} \quad = \quad \sigma_b \sqrt{\frac{\pi a}{Q'}} F(\frac{a}{t}, \frac{a}{c}, \frac{c}{w}, \phi) \tag{4.2}$$

59
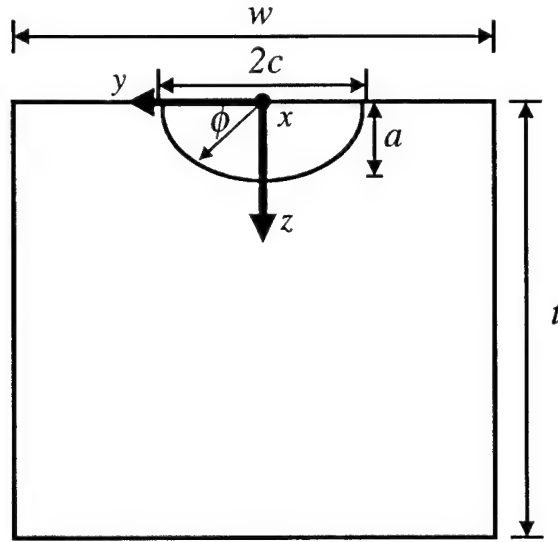
Figure 4-1: A schematic of a cross section of the specimen showing the thumbnail crack, coordinates x, y, and z, and the various parameters required to determine the stress-intensity factor: w=width, t=thickness, $2c$=crack width, a=crack length, and ϕ=radial angle from the center of the crack width.

$$Q' = 1 + 1.464(\frac{a}{c})^{1.65} \tag{4.3}$$

where ϕ is an angle measured from midpoint of the crack at the surface and F is given by

$$F = \left[M_1 + M_2(\frac{a}{t})^2 + M_3(\frac{a}{t})^4\right] f_\phi g f_w \tag{4.4}$$

The various terms in F are defined as follows.

$$M_1 = 1.13 - 0.09(\frac{a}{c}) \tag{4.5}$$

$$M_2 = -0.54 + \frac{0.89}{0.2 + \frac{a}{c}} \tag{4.6}$$

$$M_3 = 0.5 - \frac{1.0}{0.65 + \frac{a}{c}} + 14(1.0 - \frac{a}{c})^{24} \tag{4.7}$$

$$g = 1 + [0.1 + 0.35(\frac{a}{t})^2](1 - \sin\phi)^2 \tag{4.8}$$

$$f_\phi = [(\frac{a}{c})^2 \cos^2\phi + \sin^2\phi]^{1/4} \tag{4.9}$$

$$f_w = \left[\sec \left(\frac{\pi c}{2w} \sqrt{\frac{a}{t}} \right) \right]^{1/2} \tag{4.10}$$

Note that a corresponds to the length of the crack, not the contact radius ($a_{contact}$) from above (see figure 4-1). The thickness, t, and width, w, of the specimen are both 4.762 mm.

Upon measurement of the initial region III a_o and c_o for each specimen, the stress intensity factor should be greater than the fatigue threshold. Although a long-crack threshold stress-intensity factor for $R = -1$ could not be found in the literature search, approximations can be made from the threshold data available. Lütjering and Gysler [46] found the threshold stress intensity factor for Ti−6Al−4V to be between 3 and 7 MPa$\sqrt{m}$ for a load ratio of 0.1. Liaw et al. [58] determined that the threshold for titanium alloys lies between 1 and 2.5 MPa$\sqrt{m}$. Boyce et al. [51] found the fatigue threshold to be 2.2 MPa$\sqrt{m}$ for $R = 0.9$ in solution treated overaged Ti−6Al−4V with comparable strengths to the presently examined mill annealed batch. Using the measured a_o and c_o of the present investigation, the smallest stress intensity factor for the tests conducted was found to be 8.3 MPa$\sqrt{m}$ which is sufficiently larger than the reported fatigue crack growth thresholds. Therefore, one can be confident that for $a \geq a_o$ the crack will follow a Paris-type fatigue law where the crack growth per cycle is determined by [59]:

$$\frac{da}{dN_{III}} = C(\Delta K_I)^m \tag{4.11}$$

where C and m are material constants and ΔK_I is the range of the mode I stress intensity factor, $\Delta K_I = (1 - R)K_I$. One should note that the above stress intensity factor is for monotonic loading. For a fatigue loading of $R = -1$, $\Delta K_I = 2K_I$ where K_I is the stress intensity factor for monotonic loading.

The relationship between fatigue crack growth rate in air and ΔK_I has been determined experimentally by several sources. C and m for mill annealed Ti−6Al−4V are determined from a low load ratio (to account for crack closure) are reported to be $C = 7.5 \times 10^{-13}$ and $m = 4.1$ for da/dN_{III} in m/cycle and ΔK_I in MPa$\sqrt{m}$ [49]. A SEM was utilized to examine the fracture surface of a specimen with bulk stress of 280 MPa and contact conditions of $Q_{max} = 15$ N and $N = 50$ N. Confirming optical examination, the SEM could not locate fatigue striations in the initiation/nucleation region nor in the fast fracture region but only in the Paris region.

a (mm)	ϕ (rad)	da/dN_{III} striations (m/cycle)	da/dN_{III} calculated (m/cycle)	ΔK_I (MPa$\sqrt{m}$)
0.44	1.11	2.1×10^{-7}	0.88×10^{-7}	17.3
1.09	1.39	3.86×10^{-7}	7.6×10^{-7}	29.2
1.43	1.57	11×10^{-7}	17.0×10^{-7}	35.5

Table 4.1: Crack growth rate as determined by striation spacing and calculation for several locations on a fracture surface of a mill annealed specimen from a test with a tangential load of 15 N, normal load of 50 N, bulk stress of 300 MPa and pad radius of 12.7 mm.

Table 4-1 shows that the crack growth rate as determined by the above relation agrees well with striation spacing on the fracture surface.

Boyce et al. [51] empirically determined a relationship for fatigue crack growth in the Air Force HCF program STOA material but found that the relationship did not describe crack growth at low loading ratios. The number of cycles spent in region III as determined by the relationship from Boyce et al. overestimated our experimental propagation life. Jaffee et al. [37] showed that although the fatigue crack growth resistance of a bimodal material is greater than that of a mill annealed material, the difference is very small. Thus, the same Paris law constants were used for both the bimodal and mill annealed material.

The number of cycles spent in crack propagation can be determined by integration of the Paris equation where the limits of integration range from a_o to $(a_o/c_o)t/2$ (when the crack reaches the side of the specimen) or a_c (when K_{IC} is reached). The fracture toughness for Ti$-$6Al$-$4V ranges from 33-110 MPa$\sqrt{m}$ depending on oxygen content and heat treatment. For the mill annealed and STOA microstructures, this value should be 65 MPa$\sqrt{m}$ [47]. In this analysis, a Mathematica® program was made to numerically perform the integration of equation (4.11) and calculate the propagation life. Subtracting the propagation life from the total life N_f yields the number of cycles spent initiating and nucleating a crack.

Figure 4-2 is a plot comparing varying tangential loads at a maximum bulk stress of 300 MPa to percentage of life spent in regions I & II. Since the bulk stresses are the same in each experiment, it can be expected that the amount of life in stage three to be roughly the same. Thus, the focus of the variation $N_{I\&II}$ in can be placed squarely on the contact conditions. As $Q_{max}/(\mu N)$ approaches 1 the number of cycles spent in regions I & II decreases significantly. As $Q_{max}/(\mu N)$ is decreases, the amount of fatigue life spent in initiating and nucleating the fretting fatigue crack increases up to 90-95% of the total life. This indicates that a contact

fatigue threshold is being reached. For the mill annealed tests with 12.7 mm pads, this indicates a threshold near $Q_{\max}/(\mu N) = 0.2$.
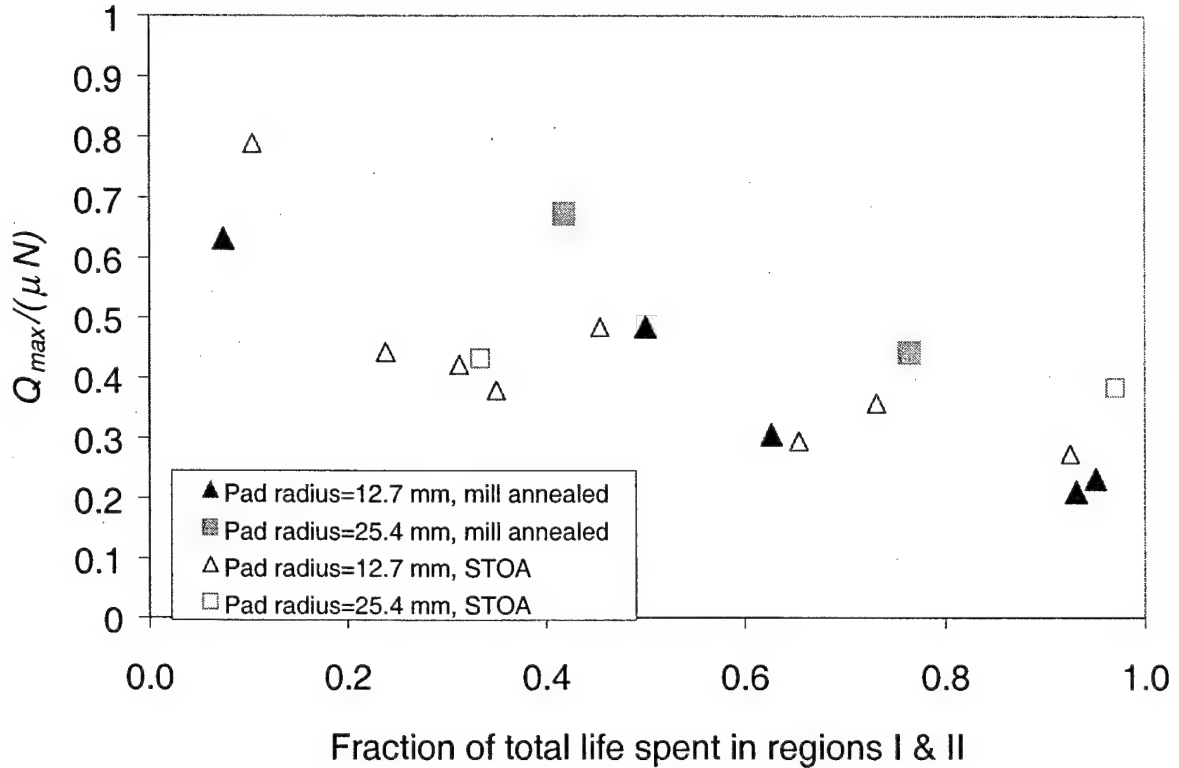
Figure 4-2: A plot of contact stresses versus fraction of life spent in regions I & II for a maximum bulk stress of 300 MPa.

Figure 4-3 is a plot comparing the maximum bulk stress for four contact conditions ($Q_{\max}/(\mu N) = 0.43$ for $\rho = 12.7$ mm and 25.4 mm pads and $Q_{\max}/(\mu N) = 0.86$ for the same pad radii). Data scatter at $Q_{\max}/(\mu N) = 0.43$ makes determination of the effect of pad radius difficult. The bulk stresses provide local mode I and II stress intensity factors during region II. It may also play a role in the initiation process, which will be discussed in further detail below. It is also clear that the increase in tangential load from $Q = 15$ N to $Q = 30$ N produces a dramatic decrease in the life spent initiating and nucleating a crack provided that the bulk stress is sufficient to propagate the crack. The effect of the contact conditions on regions I & II is far more dramatic than that of the bulk stress. In fact, if the effect of bulk stresses on region II

63

is removed from this figure, there would be little or no effect on crack initiation by the bulk stress. This indicates that a more detailed picture of crack initiation than just the stresses is required. That will be the role of the adhesion model to be discussed later.
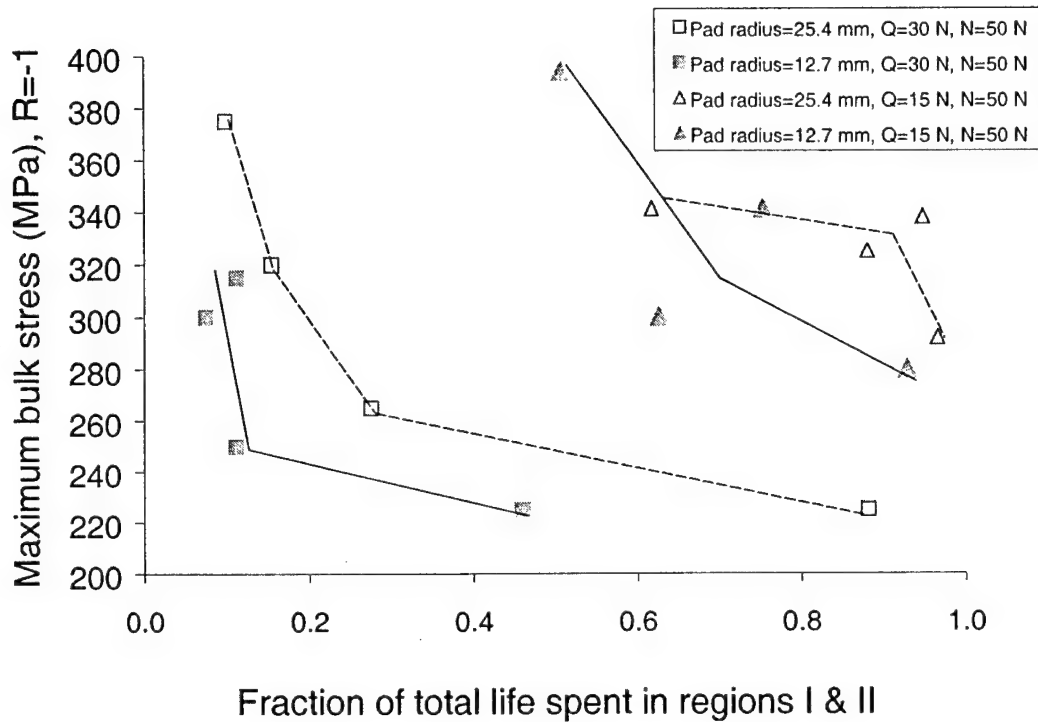
Figure 4-3: A plot showing the effect of the maximum bulk stress on the fraction of life spent in regions I & II for various constant contact conditions.

Interestingly, the data indicated that the contact conditions played no (or very little) role on the life spent in region III. The most likely effect that contact conditions could have on region III would be to change the shape of the crack thus changing the stress intensity factor. However, measurements of the crack shape showed that neither a/c nor a_o/c_o varied systematically with changes in the contact loading.

4.2 Contact stresses

The stresses beneath a sliding sphere were explicitly found by Hamilton [38] The most critical region is the surface along the x-axis ($y = 0$, $z = 0$). The corresponding stress relations were determined by Hamilton for inside the contact radius and along the x-axis ($x^2 + y^2 \leq a^2_{\text{contact}}$, $y = 0, z = 0$):

$$\sigma_x = p_{\text{max}}[-\frac{1 - 2\nu}{3}\chi^{-2}\{(1 - \chi^2)^{3/2} - 1\} - (1 - \chi^2)^{1/2}]$$
$$-\mu p_{\text{max}}\chi[\frac{\pi}{2}(\frac{\nu}{4} + 1)] \tag{4.12}$$

$$\sigma_y = p_{\text{max}}[\frac{1 - 2\nu}{3}\chi^{-2}\{(1 - \chi^2)^{3/2} - 1\} - 2\nu(1 - \chi^2)^{1/2}] - \mu p_{\text{max}}\chi\frac{3\pi\nu}{8} \tag{4.13}$$

Where $\chi = x/a_{\text{contact}}$, p_{max} is given by equation (1.3) and ν is the Poisson's ratio. Outside the contact radius($x^2 + y^2 \geq a^2$, $y = 0, z = 0$):

$$\sigma_x = p_{\text{max}}(\frac{1 - 2\nu}{3})\chi^{-2} - \frac{\mu p_{\text{max}}}{4}[\chi(\nu + 4)\arctan(\chi^2 - 1)^{-1/2}$$
$$-2\nu\chi^{-3}(\chi^2 - 1)^{3/2} + \chi^{-1}(\chi^2 - 1)^{1/2}(\nu - 4)] \tag{4.14}$$

$$\sigma_y = -p_{\text{max}}(\frac{1 - 2\nu}{3})\chi^{-2} - \frac{\mu p_{\text{max}}}{4}[3\nu\chi\arctan(\chi^2 - 1)^{-1/2}$$
$$-2\nu\chi^{-1}(\chi^2 - 1)^{1/2}(\chi^{-2} + 3/2)] \tag{4.15}$$

Figure 4-4 a) shows the surface stresses in the x-direction for sliding spheres made of Ti−6Al−4V with $\mu = \mu_d = 0.7$, $N = 50$ N and radii of 12.7 mm and 25.4 mm. The stresses are maximum at the trailing edge. Notice that the 12.7 mm pad generates stresses of a greater magnitude than those from the 25.4 mm pad. The same effect of the pad radius occurs also for partial slip. This is due to the relationship between the contact stresses and the maximum contact pressure. The contact stresses are proportional to the maximum contact presssue, which in turn is proportional to $\rho^{-2/3}$. For an applied normal load of 50 N and $\rho = 25.4$ mm,

the maximum contact pressure is 292 MPa, yet it is 463 MPa for $\rho = 12.7$ mm. In each series of experiments conducted in this work, decreasing the pad radius does indeed reduce the fatigue strength of the material. It is also of interest to note that Hamilton's relationships are also relevant for fretting fatigue on the verge of sliding ($\mu = \mu_b = 0.95$) as shown in Figure 4-4 b).
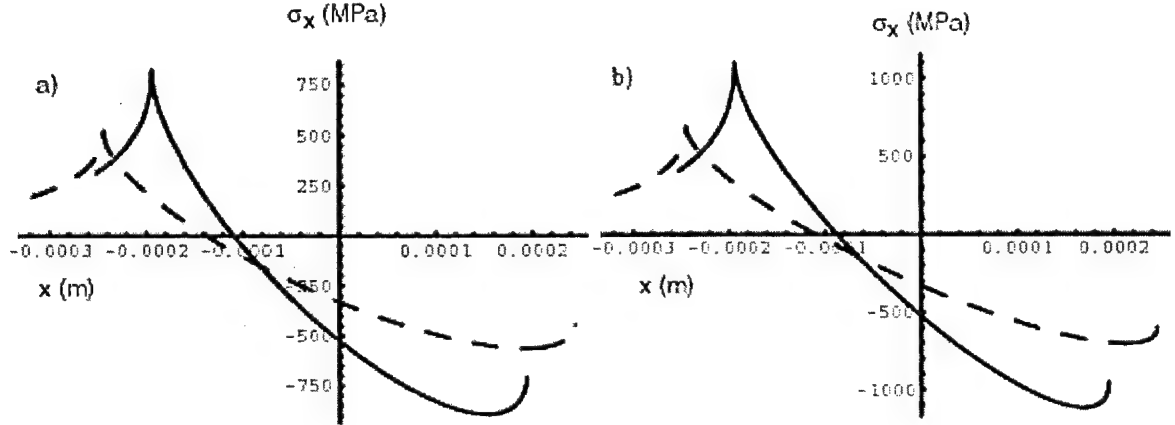
Figure 4-4: a) The contact stresses in the x-direction of two sliding Ti−6Al−4V spheres with radii of 12.7 mm (black) and 25.4 mm (gray) and $N = 50$ N and $Q = \mu = 0.95$. b) The same contact conditions as a) except $Q = \mu = 0.7$.

The stresses beneath a sphere experiencing partial slip were determined by Chivers and Gordelier [39]. As $c_{contact}/a_{contact}$ approaches zero the equations of Chivers and Gordelier reduce to those of Hamilton. Next, Chivers and Gordelier invoke Mindlin's analysis to determine the stress distribution within the slip zone:

$$\sigma_i = \sigma_{i,in} - \frac{c_{contact}}{a_{contact}}\sigma_{i,mod} \tag{4.16}$$

Where $i=x,y$; $\sigma_{i,in}$ is the stress in the ith direction and inside the contact radius, and $\sigma_{i,mod}$ is a modification of the stress field outside of the contact radius where the radius of contact, $a_{contact}$, is replaced by the radius of the stick zone, $c_{contact}$. The maximum stresses occur always at the trailing edge of contact. At the trailing edge of contact ($x = -a_{contact}$), the mean contact stresses for the conditions of partial slip are as follows:

$$\sigma_{x,\mathrm{m}}^{\mathrm{c}} = p_{\max}[(\frac{1 - 2\nu}{3})(1 - \varepsilon^3)] \tag{4.17}$$

$$\sigma_{y,\mathrm{m}}^{\mathrm{c}} = -p_{\max}[(\frac{1 - 2\nu}{3})(1 - \varepsilon^3)] \tag{4.18}$$

where ε is $c_{\mathrm{contact}}/a_{\mathrm{contact}}$. The stress amplitudes are also straightforward:

$$\begin{aligned}
\sigma_{x,\mathrm{a}}^{\mathrm{c}} &= \frac{\mu p_{\max}}{4}(\nu + 4)[\frac{\pi}{2} - \arctan\{\varepsilon(1 - \varepsilon^2)^{1/2}\}] \\
&\quad - \frac{\mu p_{\max}}{4}\varepsilon(1 - \varepsilon^2)^{1/2}[\nu(2\varepsilon^2 - 1) - 4]
\end{aligned} \tag{4.19}$$

$$\begin{aligned}
\sigma_{y,\mathrm{a}}^{\mathrm{c}} &= -p_{\max}[(\frac{1 - 2\nu}{3})(1 - \varepsilon^3)] + \frac{3\mu p_{\max}\nu}{4}[\frac{\pi}{2} - \arctan\{\varepsilon(1 - \varepsilon^2)^{1/2}\}] \\
&\quad + \frac{\mu p_{\max}}{4}[2\varepsilon(1 - \varepsilon^2)^{1/2}\nu(\varepsilon^2 + 3/2)]
\end{aligned} \tag{4.20}$$

It must be noted here that the stresses in the z-direction are zero at the perimeter of contact.

Figure 4-5 shows the contact stresses in the x-direction and along the x-axis ($y = 0$, $z = 0$) near the trailing edge for the sliding conditon shown above ($\rho = 12.7$ mm) and for two conditions of partial slip where $N = 50$ N, $Q_{\max} = 15$ N and 30 N, and $\rho = 12.7$ mm. The stresses in the x-direction will be the focus of our analysis since they tend to be an order of magnitude greater than the stresses in the y-direction. If the tangential load is increased while maintaining a specific normal load and specific pad radius, increasing $Q_{\max}$ results in an increase of the tensile stresses near the trailing edge. The maximum value of the tensile stresses occur at incipient sliding ($Q_{\max} = \mu N$). This agrees well with the experiments conducted: as $Q_{\max}/N$ approaches μ, there is a significant decrease in total fatigue life.

The surface contact stress relationships also reflect that reducing the normal load for a given tangential load (shown for $Q = 15$ N) results in an increase in the stresses despite the fact that the maximum contact pressure is decreasing. In the series of experiments where the normal load was reduced for a tangential load of 16 N, the total fatigue life was significantly reduced. Regardless of how the loading is adjusted, both the experiments and the surface contact stress
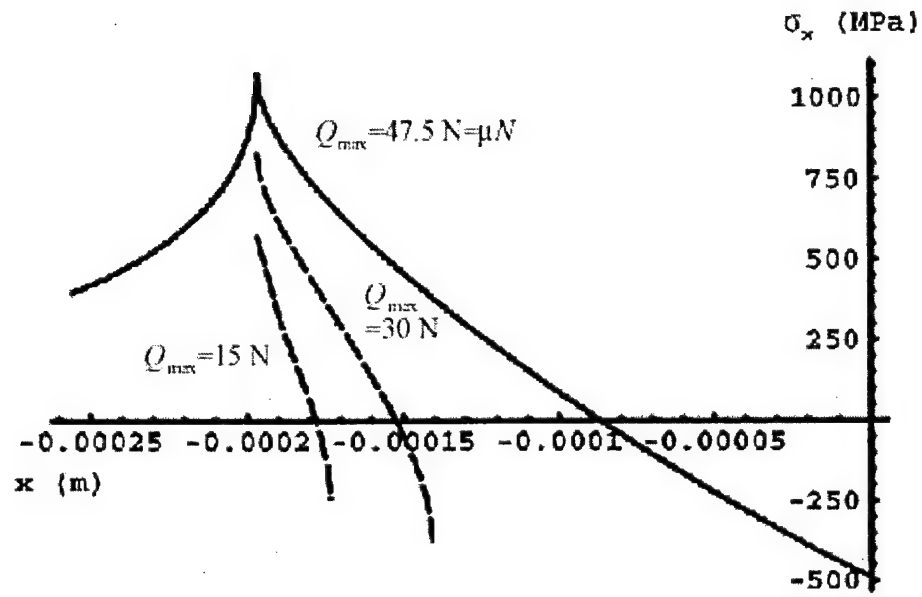
Figure 4-5: The solid curve is the surface stresses along the x-direction of a sliding sphere (ρ=12.7 mm, $N = 50$ N and $Q = \mu N = 35$ N) toward the trailing edge of contact. The dotted line is the surface stresses along the x-direction in the slip zone for a sphere of the same radius in partial-slip ($N = 50$ N and $Q = 20$ N).

analysis reveal that the most damaging contact condition occurs when $Q_{\max}/N$ approaches μ.

Note that neither Hamilton nor Chivers and Gordelier considered the effect of eccentricity on their contact stress relations. Moreover, the specimen thickness was not considered. The thickness may distort the normal stress fields if fretting occurs on both sides of a fretting specimen. See Araújo and Nowell [19] for a more rigorous approach.

4.3 Multiaxial stress fatigue crack initiation criterion

A multiaxial stress relationship was established by Crossland [60] as a criterion for significant fatigue cracking. In a simple fatigue (non-contact) geometry, this criterion will be a failure criterion. However, fretting fatigue is far more complex because the stresses are inhomogeneous. Thus, the Crossland criterion will be applied here as a crack initiation criterion. The maximum tensile stresses due to fretting are found at the trailing edge, as was discussed in the previous section. The initiation of cracks at the trailing edge will not guarantee failure unless bulk stresses are sufficient to propagate the cracks. In other words, a small region of very high stresses will be examined and if this region fails, crack initiation will occur, although crack propagation may not. The Crossland relationship has the form:

$$\sqrt{J_{2,a}} + \overline{\alpha}\sigma_{\mathrm{H,\,max}} \leq \overline{\beta} \tag{4.21}$$

where $\overline{\alpha}$ and $\overline{\beta}$ are material properties based on the limits of fully reversed torsional (t_{-1}) and bending (f_{-1}) loading determined by fatigue experiments.

$$\overline{a} = \frac{3t_{-1}}{f_{-1}} - \sqrt{3} \tag{4.22}$$

$$\overline{\beta} = t_{-1} \tag{4.23}$$

$$\sqrt{J_{2,a}} = \frac{\sigma_{\mathrm{e,a}}}{\sqrt{3}}$$

where $\sigma_{\mathrm{e,a}}$ is the Mises effective stress amplitude. Figure 4-6 is a plot showing the Mises effective

stress amplitudes at the trailing edge of contact versus the number of cycles to failure for tests varying contact conditions and a maximum bulk stress of 300 MPa (the contact conditions are given in Tables 3-2 to 3-7 . In general, an increase in the Q_{max}/N ratio leads to an increase in the Mises stress amplitude at the edge of contact.
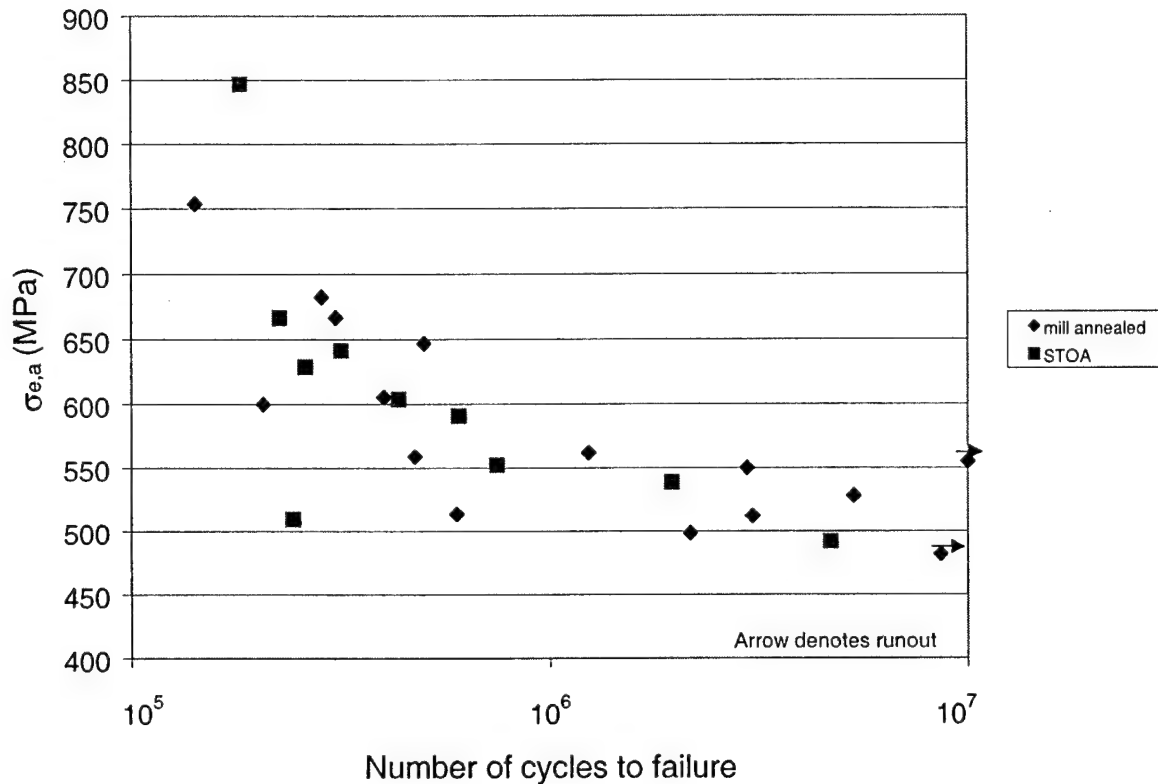
Figure 4-6: A plot of the Mises stress amplitudes at the trailing edge versus the number of cycles to failure for experimental series where the contact conditions are varied but the maximum bulk stress is constant for the series.

In out-of-phase multiaxial fatigue, the Crossland relationship is amended by replacing $\sqrt{J_{2,a}}$ with $\max \sqrt{J_{2,a}}$, which is $\sqrt{J_{2,a}}$ at the point in the loading cycle where the effective stress amplitude is a maximum. The modified criterion provides very similar estimates with the criterion proposed by Papadopoulos et al. [61] and is much simpler. Appendix C compares the results of the Papadopoulos, the modified and the original Crossland criteria for several cases of multiaxial fatigue. All three criteria yield the same results when the multiaxial stresses are

70
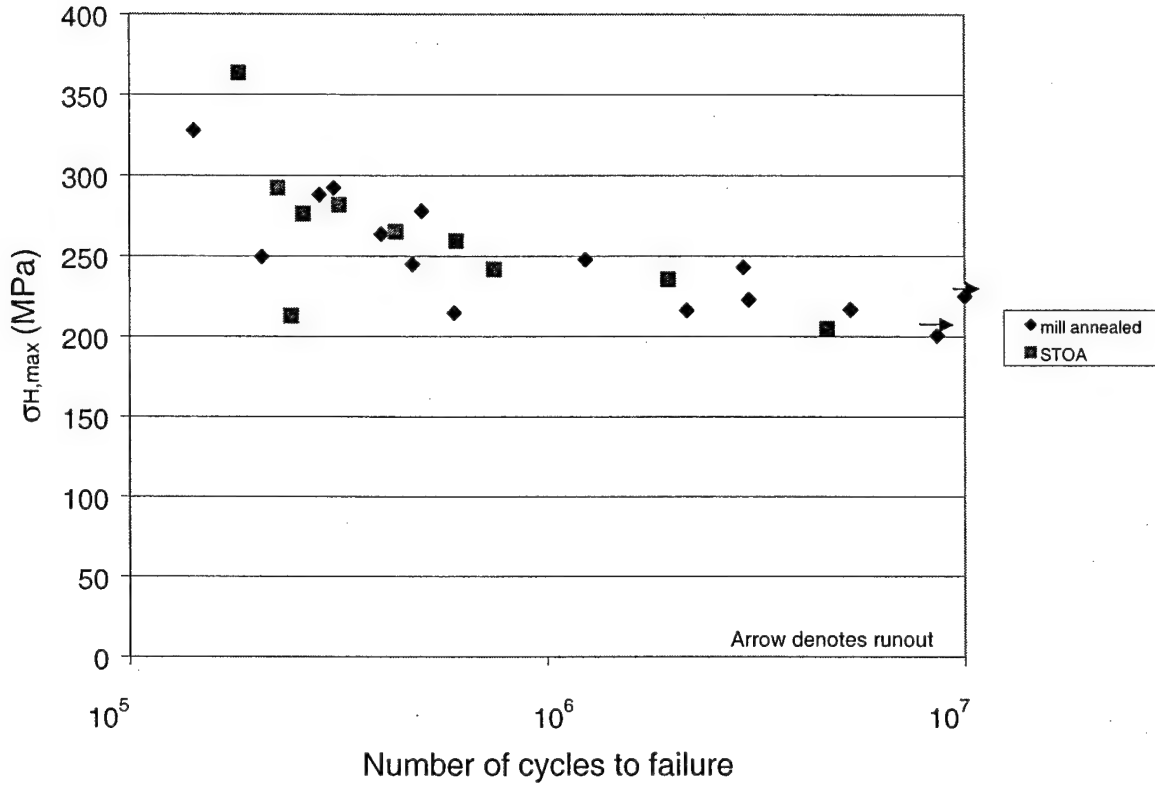
Figure 4-7: A plot of the maximum hydrostatic stresses at the trailing edge versus the number of cycles to failure for experimental series where the contact conditions are varied but the maximum bulk stress is constant for the series.

in-phase, and Papadopoulos' criterion and the Modified Crossland yield the same results also for out-of-phase conditions.

Since the contact stresses in the z-direction are zero at the contact perimeter, the $\max \sqrt{J_{2,\mathrm{a}}}$ can be written as:

$$\max \sqrt{J_{2,\mathrm{a}}} = \frac{\sigma_{\mathrm{e,a}}}{\sqrt{3}} = \sqrt{\frac{(\sigma_{x,\mathrm{a}} - \sigma_{y,\mathrm{a}})^2 + (\sigma_{x,\mathrm{a}})^2 + (\sigma_{y,\mathrm{a}})^2}{6}} \qquad (4.24)$$

where the subscript "a" denotes that these are stress amplitudes.

The maximum stresses are located at the edge of contact. This region will be the focus of the Crossland criterion. It will be assumed that given enough stress a small volume of material at the edge of contact will fail initiating the fretting crack. From Hamilton's results, it can

71

be shown that the stress state at the edge of contact is biaxial. In with the experimental conditions, the stresses will vary sinusoidally and are *in-phase*. The mean hydrostatic stress, $\sigma_{\mathrm{H,mean}}^{\mathrm{c}}$, due to normal contact is zero. However, the maximum hydrostatic stress, $\sigma_{\mathrm{H,max}}^{\mathrm{c}}$, is non-zero.

$$\sigma_{\mathrm{H,\,max}}^{\mathrm{c}} = \frac{\sigma_{x,\mathrm{max}}^{\mathrm{c}} + \sigma_{y,\mathrm{max}}^{\mathrm{c}}}{3} = \frac{(\sigma_{x,\mathrm{m}}^{\mathrm{c}} + \sigma_{x,\mathrm{a}}^{\mathrm{c}}) + (\sigma_{y,\mathrm{m}}^{\mathrm{c}} + \sigma_{y,\mathrm{a}}^{\mathrm{c}})}{3}$$

where the subscript "m" denotes terms that these are mean stresses.

We will now add a bulk stress, σ_{b}, in the x-direction. The bulk stress will sinusoidually vary in phase with the contact loading with zero mean value. This addition will affect both the amplitude of the stresses in the x-direction and the maximum hydrostatic stress. Since the bulk stress is in phase with the contact loading, it can be superposed as follows

$$\sigma_{x,\mathrm{a}} = \sigma_{x,\mathrm{a}}^{\mathrm{c}} + \sigma_{\mathrm{b}}. \tag{4.25}$$

The maximum hydrostatic stress can be found simply by superposition of the bulk and the contact maximum hydrostatic terms

$$
\begin{aligned}
\sigma_{\mathrm{H,max}} &= \frac{\sigma_{x,\mathrm{max}} + \sigma_{y,\mathrm{max}} + \sigma_{z,\mathrm{max}}}{3} = \frac{(\sigma_{x,\mathrm{max}}^{\mathrm{c}} + \sigma_{\mathrm{b}}) + \sigma_{y,\mathrm{max}}^{\mathrm{c}}}{3} \\
&= \frac{(\sigma_{x,\mathrm{max}}^{\mathrm{c}} + \sigma_{y,\mathrm{max}}^{\mathrm{c}}) + \sigma_{\mathrm{b}}}{3} = \sigma_{\mathrm{H,max}}^{\mathrm{c}} + \frac{\sigma_{\mathrm{b}}}{3}
\end{aligned} \tag{4.26}
$$

Figure 4-7 is a plot showing the maximum hydrostatic stresses at the trailing edge of contact versus the number of cycles to failure for tests varying contact conditions and a maximum bulk stress of 300 MPa (the contact conditions are given in Tables 3-2 to 3-7). The von Mises effective stress is more complicated than the maximum hydrostatic stress

$$\sigma_{\mathrm{e,a}} = \sqrt{\frac{(\sigma_{x,\mathrm{a}}^{\mathrm{c}} + \sigma_{\mathrm{b}} - \sigma_{y,\mathrm{a}})^2 + (\sigma_{y,\mathrm{a}}^{\mathrm{c}})^2 + \left(\sigma_{x,\mathrm{a}}^{\mathrm{c}} + \sigma_{\mathrm{b}}\right)^2}{2}} \tag{4.27}$$

After some algebraic manipulation this becomes

$$\sigma_{e,a} = \sqrt{\frac{(\sigma_{x,a}^c - \sigma_{y,a}^c)^2 + (\sigma_{x,a}^c)^2 + (\sigma_{y,a}^c)^2 + 2\sigma_b(2\sigma_{x,a}^c - \sigma_{y,a}^c) + 2\sigma_b^2}{2}} \qquad (4.28)$$

Residual stresses can now be considered. Such stresses would include residual stresses from peening, bending, or thermal effects. The residual stresses will not affect the stress amplitudes. However, it will impact the maximum hydrostatic stress. It must be noted that introducing a residual stress may change the material properties $\overline{\alpha}$ and $\overline{\beta}$. However, it will be assumed here that $\overline{\alpha}$ and $\overline{\beta}$ remain unchanged.

The residual stresses will be assumed to be biaxial, yet they do not have to be equal. They can be compressive (-) or tensile (+). σ_x^R is the residual stress in the x-direction while σ_y^R is the residual stress in the y-direction. First, the maximum hydrostatic stress will be examined.

$$\sigma_{H,max} = \frac{\sigma_{x,max} + \sigma_{y,max} + \sigma_{z,max}}{3} = \frac{(\sigma_{x,max}^c + \sigma_b + \sigma_x^R) + (\sigma_{y,max}^c + \sigma_y^R)}{3} \qquad (4.29)$$

Using (4.25), we obtain

$$\begin{aligned}
\sigma_{H,max} &= \frac{(\sigma_{x,max}^c + \sigma_{y,max}^c) + \sigma_b + (\sigma_x^R + \sigma_y^R)}{3} \\
&= \sigma_{H,max}^c + \frac{\sigma_b}{3} + \frac{(\sigma_x^R + \sigma_y^R)}{3}
\end{aligned} \qquad (4.30)$$

At this point, all of the major stress related variables of the problem are considered including residual stress. It is interesting to note that the residual stresses are contained only in the hydrostatic stress term. From the perspective of the Modified Crossland Criterion, the effect of the residual stresses on crack initiation is limited since the hydrostatic term is multiplied by $\overline{\alpha}$ which is typically less than one. Thus, it seems that introducing a compressive residual stress as a fretting pallative would have little effect on crack initiation.

Utilizing the stress relations from Chivers and Gordelier, one can determine the maximum contact stresses and the contact stress amplitudes. Figure 4-8 shows the experimental data

from Figure 4-6 as evaluated by the Crossland criterion. The constants $\overline{\alpha}$ and $\overline{\beta}$ for Ti−6Al−4V were determined from the uniaxial fatigue tests at multiple load ratios conducted by Bellows et al. [62]. The material constants are as follows: $\overline{\alpha} = 0.22$, $\overline{\beta} = t_{-1} = 325$ MPa and $f_{-1} = 540$ MPa. Figure 4-8 indicates that the Crossland is far too conservative, by showing that fretting almost always leads to crack initation. It is possible that cracks could initiate but the bulk stresses may not be sufficiently high enough to propagate a crack. However, fractography performed on an specimen that did not fail, seemed to indicate that no cracks had yet formed.
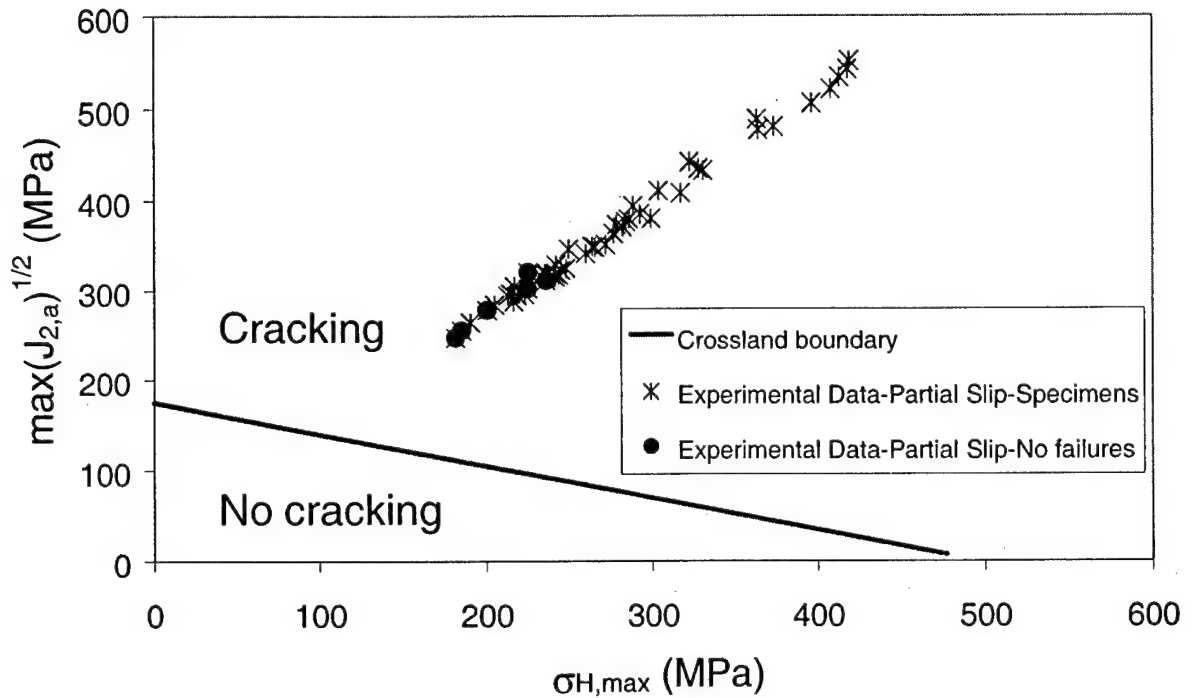
Figure 4-8: Experimental results are plotted in stress space. The line indicates boundary of the region where no cracks will initiate. The experimental points are from Figures 4-7 and 4-8.

The Modified Crossland Criterion has been extended to cylindrical geometries (both plane stress and plane strain) and was simplified for the condition of a sliding sphere; the results are included in Appendix D.

The stress-based models have several shortcomings. First, only one location of the contact

region is considered. Experimental observations of cracking in this material indicate that cracks occurs *near* the edge of contact, but not always *at* the edge of contact. Other studies have shown cracks initiating at the edge of the stick-slip zone [27]. Second, this model does not consider the full volume of the material. Cracks can initiate and subsequently arrest. A Weibull-type statistical model could be utilized to expand the Crossland stress criterion into a fretting fatigue failure model. Finally, when compared with experimental results, this model tends to be too conservative. This is because the stress model overestimates the effect of the bulk stresses on crack initiation. The previous section on the experimental results indicated that the bulk stresses play a only a minor role in crack initiation.

4.4   Adhesion model

The Modified Crossland Criterion demonstrated some of the weaknesses of examing fretting fatigue exclusively through stress fields. If one can view fretting fatigue as a fracture mechanics problem, then the question of crack initation and growth become much simplier. Often this approach to fretting fatigue is relies on accepting an arbitrary initial flaw size [23]. However, it is more advantageous to consider aspects of the contact problem and directly (or through analogy) make it equivalent to a fracture mechanics problem. This was first accomplished through a crack-analogue by Giannakopoulos et al. [25] for sharp contacts. The square root singular stresses close to the edge of a sharp contact are the same as those for various cracked edge geometries. The corresponding stress-intensity factors are then well known. It has been demonstrated with independent experimental observations that the crack analogue can accurately predict crack initiation and failure, crack entrance angles, and critical crack lengths (l_c). Similar work has been accomplished for flat contacts with rounded corners [26], a particular geometry which closely approximates the blade dovetail joint. The approach for rounded corners through a notch-type analogy has good agreement with independent experimental observations.

Giannakopoulos et al. [27], determined a fracture mechanics approach to sphere-on-flat fretting by considering the effects of surface adhesion. The short range forces of adhesion cause an increase in the contact radius. The resulting radius is

$$a_{\max} = \frac{3\rho(1-\nu^2)}{2E}\left(N + 3\pi\rho\omega + \sqrt{6\pi\rho\omega N + (3\pi\rho\omega)^2}\right) \tag{4.31}$$

where ω is the work of adhesion and for most metals, $\omega \approx 1$ N/m. The stick zone radius is determined by the following relationship.

$$c_{\max} = a_{\max}\left(1 - \frac{Q_{\max}}{\mu N}\right)^{\frac{1}{3}} \tag{4.32}$$

The tangential load that is balanced in the stick zone of radius, $c_{\max}$, is

$$Q_{\max}^{\text{in}} = Q_{\max} - \mu N \left[1 - \left(\frac{c_{\max}}{a_{\max}}\right)^2\right]^{3/2}. \tag{4.33}$$

This leads to stress-intensity factors similar to a physical crack. For conditions of partial-slip, the adhesion is considered weak adhesion, and the stress-intensity factor is

$$\Delta K_{\text{II}} = \min\left[\frac{Q_{\max}^{\text{in}}}{c_{\max}\sqrt{\pi c_{\max}}}, 2\sqrt{\frac{G_{\text{d}}E}{1-v^2}}\right] \tag{4.34}$$

where G_{d} is the debonding energy. The debonding energy can be determined experimentally or empirically. An empirical determination has been made by Giannakopoulos et al. [27] using the experimental research of McFarlane and Tabor [63] resulting in the following form (G_{d} in N/m):

$$G_{\text{d}} = 14.4(0.3 + \mu^2)^{1/2} \tag{4.35}$$

From the adhesion model, one would anticipate cracking at the stick-slip boundary for the case of "weak" adhesion and at the edge of contact for "strong" adhesion. This is a distinct advantage compared to stress-based analytical models which can predict cracking only at the edge of contact. As shown earlier, sphere-on-flat fretting fatigue cracks are initiated at or very near the edge of contact. Thus, one can analyze the experimental results using strong adhesion. The stress-intensity factor for strong adhesion differs from that of weak adhesion in that the stress singularities are moved to the edge of contact. This stress-intensity factor is

$$\Delta K_{\mathrm{II}} = \frac{Q_{\mathrm{max}}^{\mathrm{in}}}{a_{\mathrm{max}}\sqrt{\pi a_{\mathrm{max}}}}. \tag{4.36}$$

A quick evaluation of the relationships above show that as the ratio of Q_{max}/N approaches μ the stress-intensity factors for both strong and weak adhesion increase. This agrees well with the experimental results. Figure 4-9 shows ΔK_{II} for both strong and weak adhesion plotted against $Q_{\mathrm{max}}/Q_{\mathrm{bar,max}}$ for the conditions of the experimental tests conducted above where the maximum tangential load that can sustain adhesion at the maximum contact radius, $Q_{\mathrm{bar,max}}$, is

$$Q_{\mathrm{bar,max}} = 2\sqrt{\frac{(2-2\nu)}{(2-\nu)}\pi a_{\mathrm{max}}^3 \left[G_{\mathrm{d}}^{\mathrm{II}} \frac{E}{(1-\nu)} - \left(\frac{3G_{\mathrm{d}}^{\mathrm{I}}\pi\rho}{2a_{\mathrm{max}}^{3/2}} \right)^2 \right]}. \tag{4.37}$$

Also shown are the tests which did not fail and the tests with lives that equaled or exceeded 2,000,000 cycles. As Q_{max} becomes smaller, the number of no failures and tests with long lives increase. It appears that 2 MPa$\sqrt{\mathrm{m}}$ is a contact fatigue threshold for Ti$-$6Al$-$4V. Although the pure mode II fatigue thresholds have never been measured for Ti$-$6Al$-$4V, the threshold above seems to agree well with the mixed-mode thresholds determined by Campbell and Ritchie [64] as the mixity approaches the pure mode II case.

Following the model of Cottrell and Rice[65], the crack is expected to continue to advance in a direction where the local stress intensity factor, k_2, vanishes.

$$k_2 = \frac{1}{4}\left(\sin\frac{\Theta}{2} + \sin\frac{3\Theta}{2} \right) K_{\mathrm{I}} + \frac{1}{4}\left(\cos\frac{\Theta}{2} + 3\cos\frac{3\Theta}{2} \right) K_{\mathrm{II}} = 0 \tag{4.38}$$

For sphere-on-flat fretting fatigue with a constant normal force and an oscillating tangential load, K_{I} would be zero. Therefore, the expected angle, Θ, of the crack as it enters into the flat surface would be 70.5° (as shown in Figure 4-10). As shown in Appendix A, the surface measurements have found this angle to be approximately 70°. The mechanics of this model seem to follow the experimental results.

The bulk stress state (e.g. applied far-field bulk loading or residual stresses) of the specimen does not factor into the initiation ΔK_{II}. This agrees very well with the small effect of bulk stresses on crack initiation as discussed in section 4.1. From the fracture mechanics perspective,
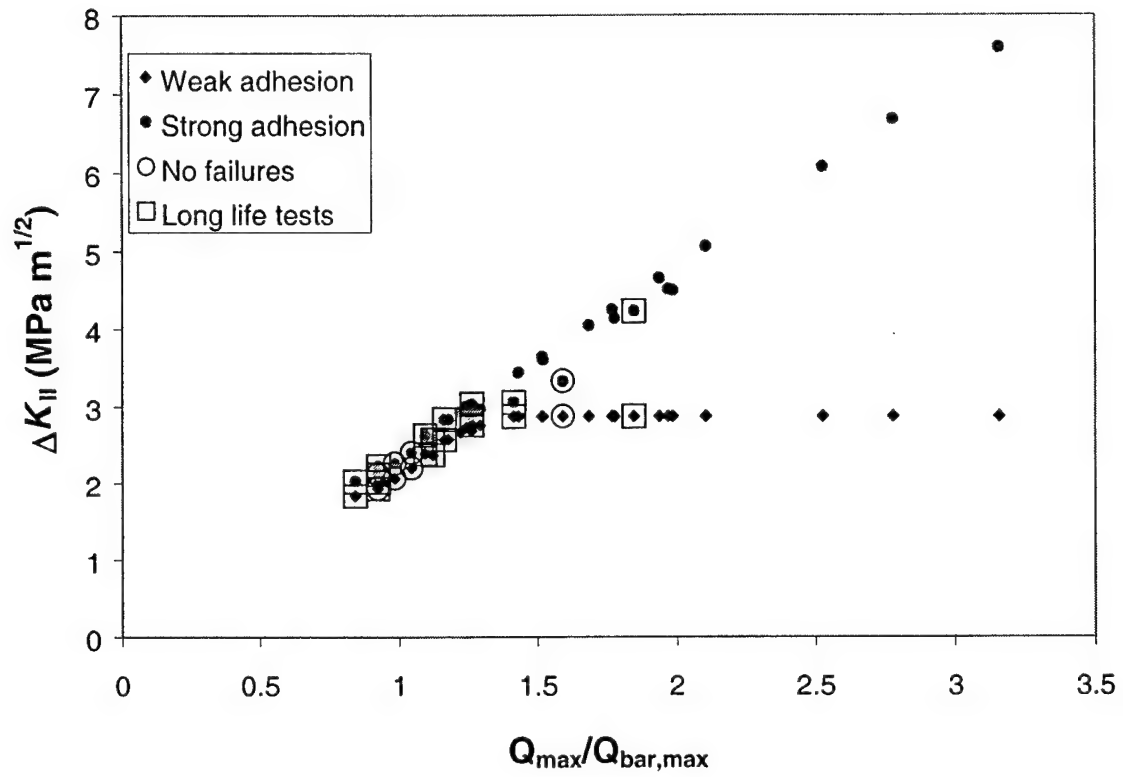
Figure 4-9: Results from the fretting fatigue tests plotted as ΔK_{II} versus $Q_{max}/Q_{bar,max}$. Of interest are the tests where failure did not occur or the test had long life. A threshold is approached at 2 MPa m$^{1/2}$

the applied bulk stresses or residual stresses would be considered as T-stresses at the initiation point. T-stresses are of only secondary importance to the square-root singular stress fields generated by adhesion (in the case of sphere/cylinder-on-flat contacts), sharp corners or stress concentrations from round corners.

The adhesion model offers several advantages. The model accurately determines the crack entrance angle for fretting fatigue in Ti−6Al−4V and as a fracture mechanics model it can easily be extended into a life-prediction methodology, as will be discussed in the following subsection. The adhesion model also yields contact fatigue thresholds. In the case of Ti−6Al−4V, this appears to be 2 MPa$\sqrt{\text{m}}$. However, the strictest interpretation of the adhesion model would connect partial-slip results with cracking at the edge of the stick-slip zone. This is clearly not the case experimentally for cracking occurs at the edge of contact for sphere-on-flat fretting of Ti−6Al−4V. On the other hand, this could be explained by the effect of adhesion due to surface modification (recall that the oxides were very adhesive), or that the debonding energy is stronger than expected. Another drawback of the adhesion model would be the difficulty in experimentally determining the debonding energy for some materials (in particular, non-metals). Knowledge of the debonding energy is required to examine fretting effects in cases of small loading conditions in materials with large debonding energies such as polymers or metals at high temperatures.

4.4.1 Life-prediction methodology based on the adhesion model

An outline for a life-prediction methodology based on the crack analogue is provided in [25] and will be adapted for the adhesion model. The groundwork for computing the number of cycles spent in region III has been outlined in Section 4.1. Again, the number of cycles in region IV will be assumed to be negligible. Figure 4-10 is a schematic of the regions of crack growth. Each of these stages will be addressed in this method.

First, one must determine if the contact loading is sufficient to cause crack initiation. If the ΔK_{II} is above the fretting fatigue threshold, then one can proceed with the life-prediction methodology.

Let the crack growth rate in region II be approximated using the Paris law in the following relation:

Figure 4-10: A schematic of the stages of fretting fatigue crack growth, the crack entrance angle, Θ, the critical crack length, l_c and the initial region III crack length, a_o.

$$\frac{da}{dN_{\text{II}}} = C_{\text{II}}(\Delta k_{\text{I}})^{m_{\text{II}}}$$

where Δk_{I} is the mode I local crack tip stress-intensity factor for a mixed-mode opening condition. C_{II} and m_{II} are experimentally determined material parameters. C_{II} and m_{II} may be short-crack parameters. For bimodal Ti−6Al−4V, a load ratio of $R=-1$ and da/dN_{II} in m/cycles and Δk_{I} in MPa$\sqrt{\text{m}}$ the short crack parameters are $C_{\text{II}} = 1.63\text{x}10^{-10}$ and $m_{\text{II}} = 2.07$ [37]. Also, if short crack growth does not follow the above relationship (even considering appropriate C_{II} and m_{II}), a more relevant relationship can be applied. If contact stresses dictate that Δk_{I} is compressive, the local shear intensity factor Δk_{II} should be examined.

N_{II} can be determined by integrating the above crack growth rate for crack lengths between zero and the critical crack length, l_{c}.

$$N_{\mathrm{II}} = \int\limits_0^{l_{\mathrm{c}}} \frac{da}{C_{\mathrm{II}}(\Delta k_{\mathrm{I}})^{m_{\mathrm{II}}}} \approx \frac{l_{\mathrm{c}}}{C_{\mathrm{II}}(\Delta k_{\mathrm{I}})^{m_{\mathrm{II}}}}$$

The above approximation can be made assuming that Δk_{I} does not change much at this stage. Strictly speaking, N_{II} the number of oscillations of the contacting pad not that of the applied bulk stresses, unless the oscillations in σ_{b} and Q are in-phase, as in the case of the experiments conducted in this study.

In terms of a crack-analogue or an adhesion model, the fracture mechanics assumes that a large crack is pre-existent. In reality, such crack does not exist, only crack-like stress conditions in the form of a square root singular stress field. Calculations of the life-prediction methodology were not completed in this thesis. Nonetheless, it is important to outline the steps for conducting such calculations.

If it is necessary to include the number of cycles required for the incubation of a physical crack, then that number must be determined experimentially. The number of cycles to incubation will be N_{I}. The number of cycles to failure can be determined by the following relationship

$$N_{\mathrm{I}} + N_{\mathrm{II}} + N_{\mathrm{III}} = N_{\mathrm{f}}, \ N_{\mathrm{IV}} \approx 0.$$

4.4.2 Thermal effects

With the presence of interfacial friction, it is expected that fretting fatigue can induce an increase in the temperature at the surface of the material. If the material or the pad (or both) are thermally conductive, the heat will be transferred away from the contact. The temperature was not measured in the series of fretting fatigue experiments conducted for this study. One would expect that at a contact frequency of 10 Hz, there would be little increase in the temperature at the contact. However, higher frequencies could increase the temperature. Giannakopoulos et al. [27] determined the following relationship for the change in surface temperature due to the friction effects of Hertzian contact fatigue:

$$\Delta T = \frac{9(3\pi - 4)(2 - \nu)(1 + \nu)}{64\pi^2 EK} \Omega \left[\frac{\mu N}{a_{\text{contact}}} \right]^2$$

where K is the thermal conductivity and Ω is the fretting frequency. The thermal conductivity for Ti−6Al−4V is reported to be between 6.6 and 6.8 W/(m K) [47]. Based on this relationship, a test performed on a Ti−6Al−4V specimen at a frequency of 10 Hz with N=50 N and $\rho =$ 12.7 mm and taking K to be 6.8 W/(m K) will experience a temperature increase slightly less than 0.1 K. Assuming no change in the coefficient of friction, the same test performed at 1 kHz will have a temperature increase at the surface of 7 K. For the series of experiments in this series, it seems justifiable that the temperature change due to fretting will be negligible. However, higher frequencies combined with high normal load or low contact radii will have some temperature effects. Fretting fatigue tests conducted at high frequencies will have to contend with strain rate sensitivity and any changes in the elastic modulus and coefficient of friction due to temperature changes. Figure 4-11 is a chart showing the fretting induced temperature change for a range of loading conditions for test frequencies of 10 Hz and 1 kHz.

4.5 A discussion on fretting palliatives

Fretting palliatives are techniques used to counter the detrimental effects of fretting fatigue. Most palliatives are surface treatments. While there are several commonly applied palliatives for plain fatigue, their applicability for fretting fatigue must be examined closely. The very characteristics that make a particular palliative undesirable to counter plain fatigue may be highly desirable to counter fretting fatigue. The complex conditions of contact mechanics make the decision of the proper palliative more vital yet more difficult.

On the basis of the previous experimental and analytical study, it is possible to determine some desired characteristics of pallatives to combat fretting fatigue.

1) Introduction of compressive residual stresses is desirable. There is little doubt about the benefit of compressive residual stresses to slow down fatigue crack growth in an engineering component [66]. However, the residual stresses have almost a negligible effect on initiation.

2) A reduction of the coefficient of friction is beneficial. This effect would drive up the
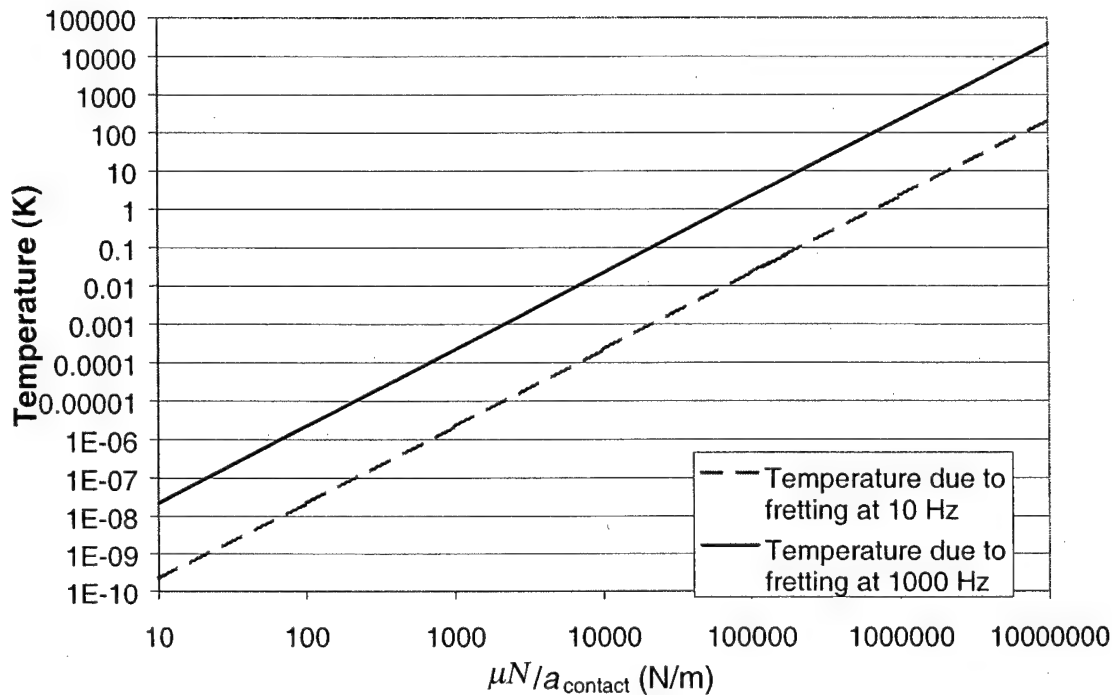
Figure 4-11: A plot of the fretting induced temperature change versus $\mu N/a_{contact}$ in Ti−6Al−4V for fretting frequencies of 10 Hz and 1 kHz.

$Q_{\max}/(\mu_b N)$ ratio for a given $Q_{\max}/N$. As shown above, the contact stresses are directly proportional to the coefficient of friction.

3) Any interference with the contact process would reduce adhesion and be beneficial [27].

4. Design the structure of the component to reduce stresses and optimize the loading. This would include changing the contact angle and the root radius of the dovetail.

5) If the plain fatigue performance allows, choose a fretting resistant microstructure. A hard surface would be desirable to resist contact.

Although must of the following discussion on palliatives will revolve around the gas turbine dovetail joint, the effects of palliatives on fretting fatigue can be of interest in other applications as well. Any palliative which would be applied to a gas turbine engine should also follow these additional guidelines:

1) The palliative should not increase the vulnerability of the blade dovetail and rotor to the corrosive environment.

2) The treatment applied to the blade dovetail and rotor should be able to survive elevated temperatures.

3) The plain fatigue life of the component should suffer minimally if possible. At best, the pallative should improve resistance to plain fatigue as well as fretting fatigue.

A note of caution must be expressed here with regard to pallatives. Applying a treatment to a component could leave the component with a reduced strength rather than an improved one. Palliatives could introduce flaws into the material or produce material changes that could weaken the component. Careful study must be used to determine the proper pallative and the full effects of that pallative. Also, redesigning components can be easier to discuss than to actually perform. The structural and vibrational conditions of the gas turbine engine has the primary focus and redesign of dovetail joints to combat fretting fatigue must fit inside the structural and vibrational specifications. With that warning, a quick overview of several potential fretting pallatives is in order.

A common fatigue palliative is shot peening. This palliative involves launching steel shot or glass beads at a metal surface at such a speed that it causes local plastic deformation [66]. The material surrounding the impact region will recover elastically as the shot rebounds. This recovery causes the deformed region to become compressive to a depth of about 0.5 mm. The material beneath that depth has tensile stresses with a magnitude dependent on the volume of material away from the surface. Shot peening does offer improved fatigue performance, but the mechanisms which do so are still in question. Much focus has been placed on the compressive residual stresses. However, the surface roughness and microstructural deformation also contribute to the tribological aspects of contact. Surface roughness may offer more crack initiation sites which can be hazardous if the residual stresses are relieved [67]. Microstructural deformation could cause the path of crack growth to be irregular, thus impeding the fatigue crack propagation. When examining the effect of shot peening on fretting fatigue, the issues are more complex. A compressive residual stress field is helpful for almost every application because of the reduction of fatigue crack growth. Roughness may be beneficial to counter fretting fatigue because of its effect on adhesion. Another concern about shot peening is that

elevated temperatures can relieve the residual stresses [67]. This concern must be considered for applying shot peening to blade dovetails near the hot stages of the engine. At that location, the combinations of high temperatures and high loadings could relieve stresses over a period of time.

Laser shock peening (LSP) is another pallative that has the potential to be used to counter fretting fatigue. A high powered laser beam is directed toward an opaque film on the surface of the material. The opaque film usually a black paint or tape absorbs the energy and is finally destroyed by the beam. A transparent medium, usually water, contains the blast and directs the energy into the material [68]. The pressure wave generates plastic deformation at the surface and compressive residual stresses [34]. Laser shock peening leaves a smoother surface compared to shot peening. The compressive residual stresses generated by laser shock peening have greater depth than that of shot peening, although at the surface, the magnitude of the residual stress is similar.

Laser shock peening is presently being applied to the leading edges of fan blades in certain types of turbine engines to protect against foreign object damage (FOD). Two beams are directed onto opposite sides of the airfoil so the system will be mechanically stable. Otherwise the blade could bend or spallate due to the force of the laser [69]. The leading edge of the airfoil is so thin that compressive residual stresses could be generated throughout the entire thickness. Although laser shock peening or any other peening can generate compressive residual stresses at the surface, tensile residual stresses must develop elsewhere in the material to preserve equilibrium. In an airfoil, there is a significant amount of material beyond the trailing edge to contain minute tensile residual stresses. However, the width and thickness of fretting test specimens are often so small that tensile residual stresses are large enough to change the length of the specimen. Thus, it is difficult to conduct fretting tests to examine the effects of laser shock peening unless the specimen size is increased or the laser power reduced (thereby reducing the residual stresses). Laser shock peening is favored in plain fatigue applications because of the smoothness of the surface after processing. The adhesion model would seem to indicate that the surface smoothness may actually be detrimental to the fretting fatigue life. Further discussion on roughness will follow.

Application of laser shock peening to the blade dovetail and to the rotor disk would be
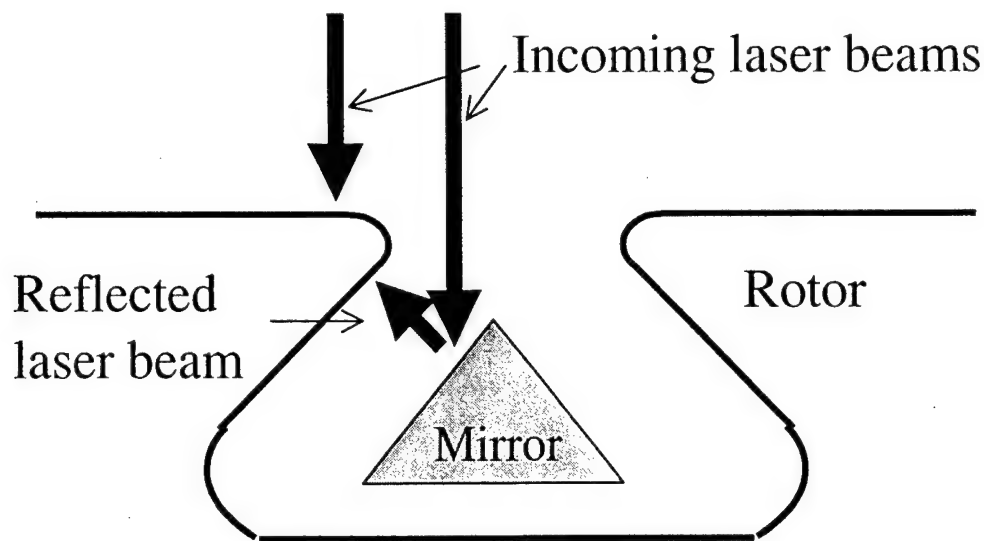
Figure 4-12: A diagram showing a possible way to conduct LSP inside a disk lug using a mirror (gray triangle) placed inside the lug. The black arrows indicate the beam directions.

difficult for two reasons. First, it is very difficult to direct a beam onto the dovetail and rotor surfaces due to their complex geometries (particularly that of the rotor). It is also more difficult to apply the opaque overlay on the surface inside the rotor joint. Second, multiple beams (in excess of two) would be required to maintain overall mechanical stability. Figure 4-12 shows a diagram of how LSP might be applied to a rotor.

Coatings are commonly applied as a surface treatment on the blade and disc contact region [34]. Often CuNiIn is applied as a soft coating with an overlay of MoS_2. The MoS_2 serves as a solid lubricant to reduce the coefficient of friction. The application of coatings makes analysis of the contact mechanics more complicated because of the changes in the coefficient of friction and the elastic contact properties.

Coatings may have only a limited effectiveness against fretting fatigue. First, the coatings may be removed by galling or delamination. Galling may occur when the engine starts up and shuts down. One investigation of a fractured disk lug from an F-100 engine indicated that a layer of $50\mu m$ of the rotor material was removed by galling [36], and it would not be surprising for the coating to be damaged in a similar way. Second, the application of coatings by a plasma spray process may relieve residual stresses from shot peening or LSP. The plasma

spray process can heat up the substrate and cause uneven surface hardness on surfaces already hardened by shot peening [34].

The discussions of contact mechanics thus far have been limited to idealized smooth contacting surfaces. In the real world, asperities exist on surfaces. Unless there is an intentional engineering of asperities, asperity contact can be modeled as a fractal [70]. Ciavarella et al. [71] analyzed the shearing contact of rough surfaces. It was demonstrated that asperities in the slip zone will slide and asperities in the stick zone will experience partial slip. Ciavarella et al. also demonstrated that the maximum damage moved from the edge of the stick-zone to the edge of contact. However, their analytical model becomes less valid as the distance between asperities is reduced (i.e. the number of asperities per unit contact area increases).

Ultimately, roughness can counter the effect of fretting fatigue because of interfacial adhesion. As adhesion increases, so do the square root stress singularities at the edge of the adhesive boundary. However, as the surface roughens, the surface roughness makes adhesion ineffective when [27]:

$$\left[\frac{3(1 - \nu^2)}{2E}\right] \geq 100 \frac{G_d^2 \rho_o}{\Sigma^3} \tag{4.39}$$

where Σ is the standard deviation of the microasperity heights and ρ_o is the average radius of curvature of the asperity tips. Sharp asperity tips ($\rho_o \longrightarrow 0$) reduce the contact surface. However, if one assumes that *valleys* between asperities also have a radius of curvature of ρ_o, then as $\rho_o \longrightarrow 0$ the valleys become like sharp notches. These would be regions where cracks could initiate under contact or bulk loads. Thus, an optimal roughness would reduce the roundness of the asperties tips or increase the standard deviation of the microasperity heights *and* not allow the radius of curvature for the asperity valleys to go to zero. Therefore, the difficulty with using roughness to combat fretting fatigue would be the control of roughness. First, special engineering techiques would have to be utilized to produce the appropriate roughness to weaken adhesion. Second, combinations of treatments could weaken the impact of roughness, as can be demonstrated by the following example. Suppose ion implanation is utilized to harden a surface to protect against contact fatigue and that the surface has an asperity height greater than the depth of penetration of the ion implantation. The asperty tips could harden and when sheared off by the fretting they will form wear particles that could initiate cracks

87

[34].

There are design options for the dovetail joints that would reduce fretting fatigue. As discussed above, the ratio of the tangential load to the normal load has a significant impact on the amount of fretting damage. From Figure 1-1, it is readily apparent that the values of the tangential load and the normal load are dependent on the pitch angle, ϕ', formed by the base of the blade and the side of the blade which contacts the rotor. If that angle was reduced, the ratio would also be reduced since $\phi' = \tan Q/N$. Another design option is to change the root radius of the blade. Recall that a flat contact with rounded corners is very analogous to the dovetail joint contact. Changing the radius of the rounded corner (the root radius) could also yield beneficial results.

Combining the blades and the rotor disks together into one unit will completely remove the dovetail joints and the associated fretting fatigue leading to integrated blade rotor (IBR) designs. A materials selection decision must be made because blades are manufactured out of Ti−6Al−4V for its resistance to FOD and the disk is made of Ti−17. Some research has been conducted in to determine which titanium alloy would be better for IBR and initial results indicate a preference for Ti−17 [72]. While the complete removal of all fretting fatigue is attractive, the concern with IBR is FOD. In a conventional blade-rotor system, a blade that has been severely damaged by FOD can be easily replaced. Such damage in an IBR could result in the expensive replacement of the entire component. Thus, the blade structures in an IBR must be treated with LSP, shot peening, or low plasticity burnishing. Improved cutting and welding techniques will be required to remove and replace extremely damaged blades without replacing the entire IBR. In the end, using IBR to remove the fretting fatigue threat could result in an equally severe and expensive HCF/FOD problem.

Chapter 5

Conclusions

5.1 Summary

A novel fretting fatigue apparatus was employed to examine the fundamental characteristics of fretting fatigue in several microstructures Ti−6Al−4V. The following results can be surmised:

1) It is very clear that variations in the contact conditions have the primary impact on the initiation of fretting fatigue cracks. The effect of the bulk stresses on initiation is minimal. The most damaging contact conditions occur when $Q_{\max}/N$ approaches the coefficient of friction. The contact stresses at/near the trailing edge are maximized under those conditions.

2) Also, for a given load, a decrease in the pad radius results in a decrease in total life of the component. The maximum contact pressure (and therefore the contact stresses) increase for a given load as the pad radius increases.

3) The location of cracking was always at or near the edge of contact. Multiple cracks often initiate at or near the edge of contact along the x-axis. These cracks will sometimes join. However, often only one crack will propagate to failure and the others will arrest.

4) The dynamic coefficient of friction for the mill annealed and STOA variants of Ti−6Al−4V was determined to be 0.7 and the breakaway coefficient is 0.95. From comparison with literature values, it appears that the determination of the coefficient of friction is sensitive to the loading history.

5) At room temperature the effects of various microstructures on fretting fatigue resistance was difficult to determine. However, it was clear that the martensitic variant of Ti−6Al−4V

was resistant to the effects of fretting fatigue.

The experimental results can be examined in the light of the analytical models to determine further results.

1) Utilizing common stress-based models for fretting fatigue crack initiation and initial growth are unwieldly and may not offer the correct location of cracking. Fracture mechanics based models are less complex and can be directly employed in life prediction methodologies. It is preferred to use a fracture mechanics model which can directly relate contact parameters into the fracture mechanics. Otherwise, empiricially determined fictitious initial flaw sizes must be employed. The adhesion model of Giannakopoulos et al. agrees well with the experimental results for sphere-on-flat fretting fatigue in Ti−6Al−4V for contacting surfaces of equal hardness. This model accurately predicted the crack entrance angle to be near 70°. The stress-intensity factors for stage I increase as Q_{max}/N approaches the coefficient of friction. In conjunction with the experimental results, this model yields a contact fatigue threshold near 2 MPa$\sqrt{\mathrm{m}}$ for fully reversed contact fatigue.

2) The adhesion model indicates that bulk stress plays a minor role in the initiation of fretting fatigue cracks compared to the role of contact conditions. The bulk stress is the driving force for region III crack propagation. The removal of the number of cycles the crack spent in stage III reveals that bulk stresses play only a minor role in region I and II. Considering that bulk stresses provide some mode I and II stress-intensity factors during region II, the effect of the stress state in the bulk of the material on fretting crack initiation is negligible. Residual stresses would be included in the stress state of the bulk; therefore, palliatives involving residual stresses will only affect fatigue crack growth propagation.

3) From points 1) and 2) it is clear that stress-based models have a distinct disadvantage when describing fretting fatigue. Fracture mechanics based models map the process of fretting fatigue from initiation to failure. They tend to be more robust than the stress-based models.

5.2 Future work

Fretting fatigue is an old problem with new techniques being employed to understand it and combat its effects. However, the problem is now better understood but not yet solved. The

examination of the fundamental mechanical and microstructural characteristics of fretting fatigue in Ti–6Al–4V should form the groundwork for a variety of future work. For example, several new technologies have developed that could prove to be useful as fretting palliatives. Experimental observations must be made for each of these pallatives and compare them to the baseline material.

The effects of shot peening and laser shock peening on fretting fatigue should be examined closely. In particular, shot peening should be examined in such way that the effects of surface roughness and residual stresses can be separated. Also, care must be taken in applying residual stress treatments so that the geometry of the specimens would not be severly altered. Along with the experimental examination of shot peening and laser shock peening, comprehesive analytical and numerical models of the contact, bulk and residual stresses should be developed. Another pallative that could have major potential is low-plasticity burnishing (LPB). Low-plasticity burnishing can generate a deeper zone of compressive residual stresses than shot peening. It also produces less cold work (and surface damage) than shot peening and can be very cost effective [73].

Coatings will continue to be of use as a palliative for contact fatigue in general. Functionally graded coatings could be developed with fretting resistance surface characteristics that has an atomic level gradient into the composition of the base material. Examination of the effect of the coefficient of friction and the hardness of coatings must be continued.

The effects of roughness and adhesion should be examined in detail. Of particular use would be the determination of debonding energies for Ti–6Al–4V. Another interesting exploration would be to show the interaction (or lack thereof) between hardness and adhesion and the effect of that interaction on the adhesion model.

More experimental work on the effect of the Ti–6Al–4V microstructure should be conducted. Eventually, experiments should be performed at high temperatures to examine fretting fatigue resistance of the various microstructures at those temperatures.

Along with experimental work, research must continue on the development of robust analytical and numerical models of fretting fatigue. The understanding of the stress fields underneath the contact should be made complete. The models should also help to increase the knowledge of the evolution of the stress fields at any given point as a function of both the contact and bulk

91

stress frequencies (these may not be in-phase). These models have to incorporate the effects of pallatives as well. The understanding of the stress-fields can help us determine more realistic stress-intensity factors for the life-prediction methodology.

5.3 Acknowledgments

always believed in me. May God bless each of you.

Appendix A

Fractography results for fretting fatigue experiments

Below are the results of fractography conducted post-failure on fretting fatigue specimen fracture surfaces. The dimensions of the thumbnail crack at the beginning of region III are given by a_o and c_o, and Θ is the measured crack entrance angle. The description of the measurement process can be found in section 3.7. See Tables 3.1 to 3.5 for further details of the experimental conditions.

	a_o (μm)	c_o (μm)	Θ (°)	fracture location
B1	280	300	80.7	cannot determine
B2	n/a	n/a	n/a	n/a
B3	180	310	n/a	edge
B4	200	250	n/a	edge
B5	180	310	68.7	edge
B6	120	275	n/a	edge/outside of contact
B7	250	300	n/a	edge
B8	130	255	72.9	outside of contact
B9	n/a	n/a	n/a	n/a
B10	200	300	n/a	edge/outside of contact

Table A.1: Fractography results for experiments where bulk stresses are varied for constant contact conditions.

	a_o (μm)	c_o (μm)	Θ (°)	fracture location
B11	n/a	n/a	n/a	n/a
B12	n/a	n/a	n/a	n/a
B13	150	275	56.3	edge
B14	180	280	n/a	cannot determine
B15	160	210	58	edge
B16	231	256	68.9	edge
B17	180	230	67.4	edge
B18	100	170	n/a	edge/outside of contact
B19	260	350	71.9	edge/outside of contact
B20	150	255	n/a	edge
B21	320	360	73.5	edge

Table A.2: A continuation of the fractography results for experiments where bulk stresses are varied for constant contact conditions.

	a_o (μm)	c_o (μm)	Θ (degrees)	fracture location
T1	180	280	57.3	cannot determine
T2	70	260	75.3	edge
T3	200	250	75.7	edge
T4	137.5	240	82.9	slip zone/edge
T5	360	250	72.8	slip zone/edge

Table A.3: Fractography results for experiments using the mill annealed material where the tangential load is varied for a normal load of 50 N, an applied bulk stress of 300 MPa and a pad radius of 12.7 mm.

	a_o (μm)	c_o (μm)	Θ (°)	fracture location
T6	123	241	59.3	edge (linked w/crack from stick-slip boundary)
T7	148	185	78.4	slip zone
T8	185	198	70.1	slip zone
T9	222	309	77.2	slip zone
T10	185	210	70.9	edge
T11	197	259	72.0	slip zone
T12	222	272	65.3	edge
T13	160	228	79.0	edge

Table A.4: Fractography results for experiments using the STOA material where the tangential load is varied for a normal load of 50 N, an applied bulk stress of 300 MPa and a pad radius of 12.7 mm.

	a_o (μm)	c_o (μm)	Θ (°)	fracture location
T14	150	210	71.6	outside of contact
T15	n/a	n/a	n/a	n/a
T16	n/a	n/a	n/a	n/a

Table A.5: Fractography results for experiments using the mill annealed material where the tangential load is varied for a normal load of 50 N, an applied bulk stress of 300 MPa and a pad radius of 25.4 mm.

	a_o (μm)	c_o (μm)	Θ (°)	fracture location
T17	173	241	68.3	edge
T18	148	253	55.4	edge (linked w/crack from stick-slip boundary)

Table A.6: Fractography results for experiments using the STOA material where the tangential load is varied for a normal load of 50 N, an applied bulk stress of 300 MPa and a pad radius of 25.4 mm.

	a_o (μm)	c_o (μm)	Θ (°)	fracture location
N1	200	250	75.3	edge
N2	90	200	60.9	edge
N3	75	150	61.9	edge
N4	100	200	n/a	edge
N5	140	250	60.2	slip zone/edge
N6	150	250	75.1	slip zone/edge

Table A.7: Fractography results for experiments using the mill annealed material where the normal load is varied for a tangential load of 16 N, an applied bulk stress of 300 MPa and a pad radius of 12.7 mm.

	a_o (μm)	c_o (μm)	Θ (°)	fracture location
N7	100	250	65.8	edge
N8	n/a	n/a	n/a	n/a
N9	180	295	60.9	can't determine

Table A.8: Fractography results for experiments using the mill annealed material where the normal load is varied for a tangential load of 16 N, an applied bulk stress of 300 MPa and a pad radius of 25.4 mm.

	a_o (μm)	c_o (μm)	Θ (°)	fracture location
Martensitic 1	n/a	n/a	n/a	plain fatigue
Martensitic 2	n/a	n/a	n/a	n/a
Coarse STOA 1	102	248	57.9	edge
Coarse STOA 2	114	235	52.1	edge
Fine Lamellar	190	337	n/a	slip zone
Widmanstätten 1	n/a	n/a	n/a	edge
Widmanstätten 2	n/a	n/a	n/a	edge

Table A.9: Fractography results for experiments on several microstructures where the tangential load is varied for a normal load of 50 N, an applied bulk stress of 300 MPa and a pad radius of 12.7 mm.

Appendix B

Region I, II & III for fretting fatigue experiments

The results of the Paris law calculations to determine region III crack propagation life are listed in the tables below. N_f is the number of cycles to failure and was determined experimentally. N_{III} is the number of cycles the crack spent in region III and was calculated. $N_{I\&II}$ is the number of cycles the crack spent during regions I & II and was determined by subtracting N_{III} from N_f.

	N_f	N_III	$N_\text{I\&II}$
B1	107899	53,232	54,667
B2	31,540	n/a	n/a
B3	266,176	65,575	200,601
B4	474,656	177,275	297,381
B5	2,055,856	147,124	1,908,732
B6	192,000	73,473	118,527
B7	872,863	104,417	768,446
B8	8,596,572	84,474	1,524,764
B9	1,609,238	n/a	n/a
B10	3,962,688	137,493	3,825,195

Table B.1: Total life, number of cycles in region III and number of cycles in regions I and II for experiments where bulk stresses are varied for constant contact conditions.

	N_f	N_III	$N_\text{I\&II}$
B11	4,273,718	n/a	n/a
B12	2,288,839	n/a	n/a
B13	117,183	104,030	13,153
B14	142,746	132,074	10,672
B15	278,238	247,080	31,158
B16	691,612	374,035	317,577
B17	85,957	77,427	8,530
B18	212,491	179,662	32,829
B19	245,637	178,088	67,549
B20	253,700		
B21	3,295,860	390,790	2,905,070

Table B.2: A continuation of the total life, number of cycles in region III and number of cycles in regions I and II for experiments where bulk stresses are varied for constant contact conditions.

	N_f	N_III	$N_\text{I,II}$
T1	142,746	132,074	10,672
T2	307,653	153,745	153,908
T3	474,656	177,275	297,381
T4	3,057,892	152,907	2,904,985
T5	2,163,277	399,807	2,013,277

Table B.3: Total life, number of cycles in region III and number of cycles in regions I and II for experiments using the mill annealed material where the tangential load is varied for a normal load of 50 N, an applied bulk stress of 300 MPa and a pad radius of 12.7 mm.

	N_f	N_{III}	$N_{I\&II}$
T6	1,955,612	147,613	1,807,999
T7	745,000	257,406	487,594
T8	433,195	281,618	151,577
T9	227,972	124,413	103,559
T10	317,073	241,400	75,673
T11	605,023	162,264	442,759
T12	182,617	163,544	19,073
T13	260,894	179,285	81,609

Table B.4: Total life, number of cycles in region III and number of cycles in regions I and II for experiments using the STOA material where the tangential load is varied for a normal load of 50 N, an applied bulk stress of 300 MPa and a pad radius of 12.7 mm.

	N_f	N_{III}	$N_{I\&II}$
T14	598,191	140,926	457,265
T15	8,596,572	n/a	n/a
T16	207,258	120,466	86,792

Table B.5: Total life, number of cycles in region III and number of cycles in regions I and II for experiments using the mill annealed material where the tangential load is varied for a normal load of 50 N, an applied bulk stress of 300 MPa and a pad radius of 25.4 mm.

	N_f	N_{III}	$N_{I\&II}$
T17	244,054	162,583	81,471
T18	4,708,273	142,253	4,566,020

Table B.6: Total life, number of cycles in region III and number of cycles in regions I and II for experiments using the STOA material where the tangential load is varied for a normal load of 50 N, an applied bulk stress of 300 MPa and a pad radius of 25.4 mm.

	N_f	N_{III}	$N_{I\&II}$
N1	474,656	177,275	297,381
N2	401,153	183,118	218,035
N3	499,291	258,959	240,332
N4	284,670	184,700	99,970
N5	1,235,575	147,827	1,087,748
N6	2,969,846	144,293	2,825,553

Table B.7: Total life, number of cycles in region III and number of cycles in regions I and II for experiments using the mill annealed material where the normall load is varied for a tangential load of 16 N, an applied bulk stress of 300 MPa and a pad radius of 12.7 mm.

	N_f	N_{III}	$N_{I\&II}$
N7	5,342,499	199,458	5,143,041
N8	12,000,000	n/a	n/a
N9	8,596,572	n/a	n/a

Table B.8: Total life, number of cycles in region III and number of cycles in regions I and II for experiments using the mill annealed material where the normal load is varied for a tangential load of 50 N, an applied bulk stress of 300 MPa and a pad radius of 25.4 mm.

Appendix C

Comparison of multiaxial fatigue criteria

Multiaxial fatigue data from Nishihara and Kawamoto first reported by McDiarmid [74]. The material was a hard steel with the following fatigue limits: f_{-1}=313.9 MPa, t_{-1}=196.2 MPa, and σ_f=680 MPa. Papadopoulos et al. compared several multiaxial fatigue criteria and determined that their criterion most accurately predicted the experimental results. The results shown in the Table C-1 below are the percentage of difference between theory and experiments. C is Crossland, P is Papadopoulos, MC is Modified Crossland, σ is the uniaxial bending, τ is a torsional loading, and δ is the difference in phase of the loadings in degrees. The subscripts a and m denote amplitude and mean value respectively.

	σ_a (MPa)	σ_m (MPa)	τ_a (MPa)	τ_m (MPa)	δ	C	P	MC
1	138.1	0	167.1	0	0	-2.3	-2.3	-2.3
2	140.4	0	169.9	0	30	-4.7	-0.6	-0.6
3	145.7	0	176.3	0	60	-4.9	3.1	3.1
4	150.2	0	181.7	0	90	-3.7	6.3	6.3
5	245.3	0	122.65	0	0	1.5	1.5	1.5
6	249.7	0	124.85	0	30	-3.9	3.3	3.3
7	252.4	0	126.2	0	60	-12.0	4.4	4.4
8	258.0	0	129.0	0	90	-17.8	6.7	6.7
9	299.1	0	62.8	0	0	0.9	0.9	0.9
10	304.5	0	63.9	0	90	-3.0	2.7	2.7

Table C.1: Torsional and uniaxial fatigue data (mean stress and stress amplitudes) in various degrees of phase and the percentage of difference between theory and experiment multiaxial stress fatigue criteria (C=Crossland, P=Papadopoulos and MC=Modified Crossland).

Appendix D

Modified Crossland Criterion for various contact fatigue geometries

Below are several simplified versions of the Modified Crossland Criterion for the sphere-on-flat and cylinder-on-flat geometries.

The first case is for sphere-on-flat sliding and is derived from the method shown in the section 4.3 "Multiaxial stress fatigue crack initiation criterion" using the equations for the contact stresses from Hamilton [38]

$$\sqrt{J_{2,a}} + \bar{\alpha}\sigma_{H,max} \leq \bar{\beta} \tag{D.1}$$

where

$$\sqrt{J_{2,a}} = \frac{1}{\sqrt{3}}\sqrt{\left(\frac{\mu p_{max}\pi}{8}\right)^2 (16 - 4\nu + 7\nu^2) + \frac{\mu p_{max}\pi}{8}\sigma_b(8 - \nu) + \sigma_b^2} \tag{D.2}$$

and

$$\sigma_{H,max} = \mu p_{max}\pi \frac{(1 + \nu)}{6} + \frac{\sigma_b}{3} + \frac{\sigma_x^R + \sigma_y^R}{3} \tag{D.3}$$

The second case is for the plane stress cylindrical contact. The plane stress condition occurs when the half-width of contact, $a_{contact}$, is greater than the width of the contact substrate. Nishioka and Hirakawa's [12] derivation of the quasi-uniaxial stress at the edge of a cylindrical contact is employed here.

$$\left(\frac{1}{\sqrt{3}} + \frac{1}{3}\right)\bar{\alpha}\left[2p_{\text{max}}\left[\frac{\mu Q}{N}\right] + \sigma_{\text{b}}\right] + \frac{\sigma_x^{\text{R}}}{3}\bar{\alpha} \leq \bar{\beta} \tag{D.4}$$

where

$$p_{\text{max}} = \frac{2N}{\pi a_{\text{contact}}}$$

is the maximum contact pressure for both plane stress and plane strain cases.

The third case is for the plane strain cylinder-on-flat contact. In this condition, the width of the specimen is much greater than that of the half-width of contact. Thus, the stresses in the cross-plane of the surface are no longer zero.

$$\sqrt{J_{2,\text{a}}} + \bar{\alpha}\sigma_{\text{H,max}} \leq \bar{\beta} \tag{D.5}$$

where

$$\sqrt{J_{2,\text{a}}} = \frac{1}{\sqrt{3}}\sqrt{\left(2p_{\text{max}}\left[\frac{\mu Q}{N}\right]\right)^2(1 - \nu + \nu^2) + 2p_{\text{max}}\left[\frac{\mu Q}{N}\right]\sigma_{\text{b}}(2 - \nu) + \sigma_{\text{b}}^2} \tag{D.6}$$

and

$$\sigma_{\text{H,max}} = \frac{(1+\nu)}{3}2p_{\text{max}}\left[\frac{\mu Q}{N}\right] + \frac{\sigma_{\text{b}}}{3} + \frac{\sigma_x^{\text{R}} + \sigma_y^{\text{R}}}{3} \tag{D.7}$$

Bibliography

[1] S. Suresh. *Fatigue of Materials*. Cambridge University Press, 1998.

[2] R. B. Waterhouse and T. C. Lindley. *Fretting Fatigue*. ESIS Publication No 18, European Structural Integrity Society. Mechanical Engineering Publications Limited, London, 1994.

[3] M. Niinomi. Recent titanium R and D for biomedical applications in Japan. *JOM*, 51(6):32–34, 1999.

[4] B. J. Briscoe, A. Chateauminois, T. C. Lindley, and D. Parsonage. Fretting wear behavior of polymethylacrylate under linear motions and torsional contact conditions. *Tribology International*, 31(11):701–711, 1998.

[5] E. M. Eden, W. N. Rose, and F. L. Cunningham. The endurance of metals. *Proceedings of the Institution for Mechanical Engineers*, 4:834–974, 1911.

[6] G. A. Tomlinson. The rusting of steel surfaces in contact. *Proceedings of the Royal Society, London, Series A*, 115:472–483, 1927.

[7] E. J. Warlow-Davies. Fretting corrosion and fatigue strength: Brief results of preliminary experiments. *Proceedings of the Institution for Mechanical Engineers*, 146:32, 1941.

[8] W. D. Milestone. Fretting and fretting fatigue in metal to metal contacts. In *Proceedings AIAA Structural Dynamics and Materials Conference*, page 96, Denver, 1970.

[9] K. Nishioka and K. Hirakawa. Fundamental investigation of fretting fatigue–part 2. fretting fatigue testing machine and some test results. *Bulletin of the JSME*, 12:180–187, 1969.

[10] K. Nishioka and K. Hirakawa. Fundamental investigation of fretting fatigue–part 3. some phenomena and mechanisms of surface cracks. *Bulletin of the JSME*, 12:397–407, 1969.

[11] K. Nishioka and K. Hirakawa. Fundamental investigation of fretting fatigue–part 4. the effect of mean stress. *Bulletin of the JSME*, 12:408–414, 1969.

[12] K. Nishioka and K. Hirakawa. Fundamental investigations of fretting fatigue. *Bulletin of JSME*, 12(52):692–697, 1969.

[13] D. Godfrey. Investigation of fretting corrosion by microscopic observation. NACA Technical Note 2039, 1950.

[14] B. Bethune and R. B. Waterhouse. Adhesion of metal surfaces under fretting conditions-i. like metals in contact. *Wear*, pages 289–296, 1968.

[15] R. B. Waterhouse. Influence of local temperature increases on the fretting corrosion of mild steel. *Journal of the iron and steel institute*, 197:301–305, 1961.

[16] M. H. Attia and N. S. D'Silva. Effect of the mode of motion and process parameters on the prediction of temperature rise in fretting wear. *Wear*, 106:206–224, 1985.

[17] M. H. Attia and P. L. Ko. On the thermal aspects of fretting wear-temperature measurements in the subsurface layer. *Wear*, 111:363–376, 1986.

[18] R. Bramhall. *Studies in Fretting Fatigue*. PhD thesis, Oxford University, 1973.

[19] J. A. Araùjo and D. Nowell. Analysis of pad size effects in fretting fatigue using short crack arrest methodologies. *International Journal of Fatigue*, 21:947–956, 1999.

[20] K. Endo and H. Goto. Initiation and propagation of fretting fatigue cracks. *Wear*, 38:311–324, 1976.

[21] P. R. Edwards. The application of fracture mechanics to predicting fretting fatigue. In R. B. Waterhouse, editor, *Fretting Fatigue*, pages 67–99, London, 1981. Elsevier Applied Science Publishers.

[22] D. Nowell. *A Analysis of Fretting Fatigue*. PhD thesis, Oxford University, 1988.

[23] L. J. Fellows, D. Nowell, and D. A. Hills. Analysis of crack initiation and propagation in fretting fatigue: The effective initial flaw size methodology. *Fatigue Fract. Engng Mater. and Struct.*, 20(1):61–70, 1997.

[24] D. A. Hills and D. Nowell. *Mechanics of Fretting Fatigue*. Kluwer Academic Publishers, 1994.

[25] A. E. Giannakopoulos, T. C. Lindley, and S. Suresh. Aspects of equivalence between contact mechanics and fracture mechanics: Theoretical connections and a life-prediction methodology for fretting-fatigue. *Acta mater*, 46(9):2955–2968, 1998.

[26] A. E. Giannakopoulos, T. C. Lindley, S. Suresh, and C. Chenut. Similarities of stress concentrations in contact at round punches and fatigue at notches: Implications to fretting fatigue crack initation. *Fracture and Fatigue of Engineering Materials and Structures*, 2000. accepted for publication.

[27] A. E. Giannakopoulos, T. A. Venkatesh, T. C. Lindley, and S. Suresh. The role of adhesion in contact fatigue. *Acta Materialia.*, 47(18):4653–4664, 1999.

[28] A. E. Giannakopoulos and S. Suresh. A three-dimensional analysis of fretting fatigue. *Acta materialia*, 46(1):177–192, 1998.

[29] G. W. Kirkpatrick. Fretting fatigue analysis and palliatives. Master's thesis, MIT, 1999.

[30] P. R. Birch. A study of fretting fatigue in aircraft components. Master's thesis, MIT, 1998.

[31] T. Nicholas. Critical issues in high cycle fatigue. *International Journal of Fatigue*, 21(1001):221–231, 1999.

[32] ACC News Service. ACC releases Cannon F-16 crash investigation report, October 1999.

[33] Pilot OK after F-16 crash at Cannon. *The Air Force Times*, 1999.

[34] A. K. Koul, L. Xue, W. Wallace, M. Bibby, S. Chakravarty, R. G. Andrews, and P. C. Patnaik. An investigation on surface treatments for improving the fretting fatigue resistance of titanium alloys. In *Tribology for Aerospace Systems*. Institute for Aerospace Research, 1996.

[35] M. P. Szolwinski, J. F. Matlik, and T. N. Farris. Effects of HCF loading on fretting fatigue crack nucleation. *International Journal of Fatigue*, 21:671–677, 1999.

[36] D. L. Davidson. Fatigue crack growth in an aeroengine disk lug due to blade attachment. In *Damage Mechanisms in High Cycle Fatigue*. Southwest Research Institute, January 1999.

[37] R. I. Jaffee and G. Lütjering. Effect of microstructure and loading conditions on fatigue of Ti–6Al–4V alloy. In *Microstructure Fracture Toughness and Fatigue Crack Growth Rate in Titanium Alloys*, pages 193–208. TMS-AIME, Metallurgical Society, Inc., 1987.

[38] G. M. Hamilton. Explicit equations for the stresses beneath a sliding spherical contact. *Proc Instn Mech Engs*, 197C:53–59, 1983.

[39] T. C. Chivers and S. C. Gordelier. Fretting fatigue and contact conditions: A rational explanation of pallative behaviour. *Proc Instn Mech Eng*, 199C:325–337, 1985.

[40] H. Hertz. On the contact of elastic solids. *J. Reine and Angewandte Mathematik*, 92:156–171, 1882.

[41] R. D. Mindlin and H. Deresiewicz. Elastic spheres in contact under varying oblique forces. *Journal of Applied Mechanics*, pages 327–344, 1953.

[42] R. D. Mindlin. Compliance of elastic bodies in contact. *Journal of Applied Mechanics*, 16:259–268, 1949.

[43] D. A. Hills and D. Nowell. *Standardization of Fretting Fatigue Test Methods and Equipment, ASTM STP 1159*, chapter The development of a fretting fatigue experiment with well-defined characteristics, pages 69–84. American Society for Testing and Materials, 1992.

[44] B. U. Wittkowsky, P. R. Birch, J. Dominguez, and S. Suresh. An apparatus for quantitative fretting fatigue testing. *Fatigue and Fracture of Engineering Materials and Structures (UK)*, 22(4):307–320, 1999.

[45] R. A. Antoniou and T. C. Radtke. Mechanisms of fretting-fatigue of titanium alloys. *Materials Science and Engineering A*, pages 229–240, 1997.

[46] G. Lütjering and A. Gysler. Titanium science and technology. *Deutsche Gesellschaft fur Metallkunde e.V.*, 4:2077, 1985.

[47] G. Welsch, R. Boyer, and E. W. Collings. *Materials Properties Handbook: Titanium Alloys.* ASM International, Materials Park, OH, 1995.

[48] C. J. Beevers and J. L. Robinson. Some observations on the influence of oxygen content on the fatigue behaviour of alpha -titanium. *Journal of the Less Common Metals*, 17(4):345–352, 1969.

[49] G. R. Yoder, L. A. Cooley, and T. W. Crooker. Observations on a fracture mechanics approach to fatigue crack initiation in Ti–6Al–4V. In M. F. Kanninen and A. T. Hopper, editors, *Fracture Mechanics: Sixteenth Symposium, ASTM STP 868*, pages 392–405, Philadelphia, 1985. American Society for Testing and Materials, American Society for Testing and Materials.

[50] J. P. Campbell and R. O. Ritchie. Summary of work in the micromechanics laboratory at southwest research institute. In *Damage Mechanisms of High Cycle Fatigue*. Southwest Research Institute, January 1999.

[51] B. L. Boyce, J. P. Campbell, O. Roder, A. W. Thompson, W. W. Milligan, and R. O. Ritchie. Thresholds for high-cycle fatigue in a turbine engine Ti–6Al–4V alloy. *submitted to International Journal of Fatigue*, 1999.

[52] L. J. Fellows, D. Nowell, and D. A. Hills. Contact stresses in a moderately thin strip (with particular reference to fretting experiments). *Wear*, 185:235–238, 1995.

[53] M. P. Szolwinski and T. N. Farris. Observation, analysis and prediction of fretting fatigue in 2024-t351 aluminum alloy. *Wear*, 221:24–36, 1998.

[54] T. N. Farris, G. Harish, P. A. McVeigh, and H. Murthy. Prediction and observation of fretting fatigue of Ti–6Al–4V subjected to Blade/Disk type contacts. In *Proceedings of the 5th National High Cycle Fatigue Conference*, 2000.

[55] D. Tabor. *Hardness of Metals.* Clarendon Press, Oxford, 1951.

[56] V. Lamacq, M. C. Dubourg, and L. Vincent. Crack path prediction under fretting fatigue a theoretical and experimental approach. *Journal of Tribology*, 118:711–720, 1996.

[57] J. C. Newman, Jr and I. S. Raju. An empirical stress-intensity factor equation for the surface crack. *Engineering Fracture Mechanics*, 15:185–192, 1981.

[58] P. K. Liaw, T. R. Leax, and W. A. Logsdon. Near-threshold fatigue crack growth behavior in metals. *Acta Metallurgica*, 31:1581–7, 1983.

[59] P. C. Paris, M. P. Gomez, and W. P. Anderson. A rational analytic theory of fatigue. *The Trend in Engineering*, 13:9–14, 1961.

[60] B. Crossland. In *Proc. Int. Conf. On Fatigue of Metals*, pages 138–149, London, 1956. Institution of Mechanical Engineers.

[61] I. V. Papadopoulos, P. Davoli, C. Gorla, M. Filippini, and A. Bernasconi. A comparative study of multiaxial high-cycle fatigue criteria for metals. *Int. J. Fatigue*, 19(3):219–235, 1997.

[62] R. S. Bellows, K. R. Bain, and J. W. Sheldon. Effect of step testing and notches on the endurance limit of Ti–6Al–4V. *ASME Mechanical Behavior of Advanced Materials*, 84:27–32, 1998.

[63] J. S. McFarlane and D. Tabor. *Proc. R. Soc. Lond*, A202:244, 1950.

[64] J. P. Campbell and R. O. Ritchie. Mixed-mode fatigue-crack growth thresholds in Ti–6Al–4V at high frequency. *Scripta Materialia*, 41(10):1067–1071, October 1999.

[65] B. Cottrell and J. R. Rice. Slightly curved or kinked cracks. *Int. J. Fract*, 16:155–169, 1980.

[66] T. C. Lindley and R. B. Waterhouse. Prevention of fatigue by surface engineering. In J. H. Beynon, M. W. Brown, R. A. Smith, T. C. Lindley, and B. Tomkins, editors, *Engineering Against Fatigue*, pages 487–499. A. A. Balkema, 1999.

[67] H. Gray, L. Wagner, and G. Lütjering. Influence of shot peening induced surface roughness, residual stresses and dislocation density on the elevated temperature HCF-properties of

Ti alloys. In *Science-Technology Application.* International Conference on Shot Peening, 1987.

[68] P. Peyre and R. Fabbro. Laser shock processing: A review of the physics and applications. *Optical and Quantum Electronics*, 27(12):1213–1229, 1995.

[69] T. de Resseguier, S. Couturier, J. David, and G. Nierat. Spallation of metal targets subjected to intense laser shocks. *Journal of Applied Physics*, 82(5):2617–2623, 1997.

[70] J. R. Barber and M. Ciavarella. Contact mechanics. *International Journal of Solids and Structures*, 37:29–43, 2000.

[71] M. Ciavarella, D. A. Hills, and R. Moobola. Analysis of plane and rough contacts subject to a shearing force. *International Journal of Mechanical Sciences*, 41:107–120, 1999.

[72] S. M. Russ. The effect of microstructure on the HCF properties of Ti–17. In *Proceedings of the 5th National High Cycle Fatigue Conference*, 2000.

[73] J. Telesman, P. Kantzos, T. Gabb, and P. Prevey. Effect of residual stress surface enhancement treatments on fatigue crack growth in turbine alloys. In *3rd Joint FAA/Dod/NASA Conference on Aging Aircraft*, 1999.

[74] D. L. McDiarmid. Fatigue under out-of-phase bending and torsion. *Fatigue Fract. Engng Mater. Struct.*, 9:457–475, 1987.